Semi-Analytical Closed-Wing Weight Estimation during Conceptual Design

R.N.J. Rousseau

Delft University of Technology

TU Delft Delft University of Technology

Challenge the future

Front page image: Artist impression of the PrandtlPlane configuration, adapted by Hameeteman.[1]

SEMI-ANALYTICAL CLOSED-WING WEIGHT ESTIMATION DURING CONCEPTUAL DESIGN

by

R.N.J. Rousseau

in partial fulfillment of the requirements for the degree of

Master of Science
in Aerospace Engineering

at the Delft University of Technology,
to be defended publicly on Monday September 18, 2017 at 09:30 AM.

Student number:	4147928	
Thesis registration nr:	161#17#MT#FPP	
Supervisor:	Dr. F. Oliviero	
Thesis committee:	Dr. A. Gangoli Rao,	TU Delft
	Dr. G. La Rocca,	TU Delft
	Ir. V. P. Brugemann,	TU Delft

An electronic version of this thesis is available at http://repository.tudelft.nl/.

TU Delft Delft University of Technology

ABSTRACT

One of the novel configurations that could revolutionize the aviation industry is the PrandtlPlane. The closed-wing design features a low front wing and a high rear wing, connected by a lateral surface. In this research, the rear wings of the configuration are attached to a set of fins. The main advantages of the configuration include reductions in induced drag and the ability to transport more payload for a given wingspan. The effect of the different structural arrangement compared to a conventional wing on the wing weight is not fully understood yet.

Previous conceptual design studies have failed to accurately predict the wing weight of the configuration, by using empirical relations or semi-analytical methods designed for conventional wings. These methods fail to capture the three major structural characteristics of a closed-wing design. First, due to the over-constrained nature of the problem, the internal loads depend on the stiffness and an iteration loop is necessary. Second, the optimal closed-wing design features reinforcements in the corners of the wingbox due to the fact that secondary bending moments and shear forces are non-negligible. Finally, the lay-out of the structural constraints is inherently different from a conventional configuration.

To improve the conceptual design of PrandtlPlanes a new closed-wing weight estimation methodology was developed. The primary weight is estimated analytically, while the secondary weights are defined by empirical relations. The primary structure is sized using an equivalent beam method, which is designed to withstand the aerodynamic, inertial and fuel loads applied to the structure. The aerodynamic loads are estimated with with a vortex lattice method, at a 2.5g pull-up manoeuvre. For the PrandtlPlane configuration, the fin is modelled as a support to the rear wing. Due to the over-constrained nature of the structure, a stiffness iteration loop is implemented in which the internal loads are determined using the displacement method and all cross-sections are sized. The cross-sectional design features four booms, which are cross-coupled and four skins, which are sized independently. A total weight estimation of a closed-wing design takes 20-30 seconds. The tool is then implemented as a Class II-1/2 in the Initiator conceptual design workflow.

The finite element tool Nastran was then used to verify that the internal loads in the closed-wing weight estimator were determined correctly. Furthermore, validations for an ATR-72 and A320-200 were performed. The results of the conventional Class II-1/2 tool EMWET were compared to the results of the new wing weight estimation methodology. They indicate an offset in wing weight of less than 1% between the two tools, for conventional designs.

Sensitivity analyses are performed to establish the main drivers of the total wing weight and its distribution. Wingspan, wing sweep angle, fin sweep angle and longitudinal center of gravity position were determined to have the most influence on the total wing weight and its distribution. High positive or negative sweep angles increase the wing weight considerably. However, the minimum wing weight is not necessarily achieved in the completely unswept design, due to the internal loads induced by the fin support. The total wing weight is most sensitive to the fin sweep angle for low main wing sweep angles. A moderately positive fin sweep angle generally leads to the lowest possible wing weight. The longitudinal center of gravity position of configuration has a large influence on the wing due to the result of trim on the applied aerodynamic loads. The lowest possible wing weight is not necessarily achieved at the condition of minimum trim control deflection. The fin sweep angles, wing sweep angles and trim condition not only influence the total wing weight, but its distribution as well. As for conventional wings, an increase in wingspan leads to a higher wing weight. The effect of this parameter on the wing weight distribution is minor however. The effect of the wing taper ratio and fin dihedral angle were found to be minor compared to the previously discussed parameters.

A comparison between a design study in the Initiator with the closed-wing weight estimator and the previous methodology showed large discrepancies. Three design studies were performed with missions varying in payload weight, number of passengers and range. The total offset in the wing weight between the two methods ranged from 4.5% to 30.4%, leading to discrepancies in the required fuel mass of 1.6% and 5.7% respectively. Apart from the large offsets in total wing weight, the previous methodology also failed to accurately predict the distribution of the weight between the front, rear and lateral wing. Furthermore, the offsets between the methodologies are case-dependent and no clear relationship between them can be distinguished. Future conceptual design studies should thus include a closed-wing weight estimator.

Finally, a parametric study was performed to identify the effect of altering the wing area ratio between the front and rear wing on the required fuel mass. Previously, such a study was impossible, because the effect on the wing weight and its distribution were not captured correctly. The results indicate that significant improvements might be achieved by keeping the variable free in a design optimization. For a single aisle, medium range mission, a design with and area ratio of 1.25 is 2% more fuel efficient compared to a design with an even area distribution between the front and rear wing. Even though these results are case-specific, they prove the necessity of including the area ratio as a design parameter in future design optimization studies.

To conclude, an accurate closed-wing weight estimation is implemented into the Initiator framework and the area ratio can now be varied. These improvements open the door for optimization studies on PrandtlPlanes and their conventional counterparts. Comparisons between these configuration should give an insight in the capabilities of the PrandtlPlane and determine whether it can indeed be the future of aviation.

Contents

List of Figures

List of Tables

NOMENCLATURE

ACRONYMS

APU	Auxiliary Power Unit
AVL	Athena Vortex Lattice
BWS	Best Wing System
CWWE	Closed-wing Weight Estimator
DLR	Deutsches Zentrum fur Luft- und Raumfahrt
EMWET	Elham Modified Weight Estimation Technique
IATA	International Air Transport Association
MTOM	Maximum Take-Off Weight
OEW	Operational Empty Weight
PrP	PrandtlPlane
TU	Technical University

SYMBOLS

LATIN

A	Cross-sectional area	$[m^2]$
b	Wingspan	$[m]$
b_{fin}	Fin span measured from centerline	$[m]$
c	Chord length	$[m]$
C_1	Howe's wing weight coefficient	$[-]$
C_L	Lift coefficient	$[-]$
C_l	Local lift coefficient	$[-]$
C_M	Aerodynamic moment coefficient	$[-]$
D_{bws}	Induced drag of the best wing system	$[N]$
D_M	Induced drag of a monoplane	$[N]$
E	Young's Modulus	$[Pa]$
F	External force at structural node (Section 4.1.5)	$[N]$
F	Internal force	$[N]$
fos	Factor of safety	$[-]$
G	Shear Modulus	$[Pa]$
g	Gravitational accelaration	$[m/s^2]$
h	Vertical spacing between wings (Chapter 2)	$[m]$
h	Cross-sectional height (Chapter 4)	$[m]$
I	Area moment of inertia	$[m^4]$
J	Polar moment of inertia	$[m^4]$
k	Local stiffness matrix	[N/m or Nm/rad]
K	Global stiffness matrix	[N/m or Nm/rad]
K_r	Reduced global stiffness matrix	[N/m or Nm/rad]
l	Beam element length	$[m]$
L	Flange support length	$[m]$
l_{rib}	Rib spacing	$[m]$
M	External moment around structural node (Section 4.1.5)	$[Nm]$
M	Internal moment	$[Nm]$
$M_{c/4}$	Moment around quarter chord	$[Nm]$
M_W	Wing mass	$[kg]$

N	Limit load factor	[−]
P	Global external loads	[N or Nm]
P_r	Reduced global external loads	[N or Nm]
q	Dynamic pressure	$[Pa]$
q_0	Closed section shear flow	$[N/m]$
q_i	Open section shear flow	$[N/m]$
S	Wing reference area	$[m^2]$
s	Local internal loads	[N or N/m]
S_a	Aileron area	$[m^2]$
S_{fle}	Fixed leading edge area	$[m^2]$
S_{fte}	Fixed trailing edge area	$[m^2]$
SM	Stability margin	[−]
S_{slat}	Slat area	$[m^2]$
S_{sp}	Spoiler area	$[m^2]$
S_{tef}	Trailing edge high lift device area	$[m^2]$
t	Skin thickness	$[m]$
T	Flange support thickness	$[m]$
t_{foil}	Airfoil skin thickness	$[m]$
t_r	Maximum airfoil thickness at root	$[m]$
t_t	Maximum airfoil thickness at tip	$[m]$
U	Global displacements	[m or rad]
u	Local displacements	[m or rad]
U	Global displacements	[m or rad]
U_r	Reduced global displacements	[m or rad]
V	Aircraft Velocity	$[m/s]$
V'	Rear wing volume coefficient	$[m^2]$
V_D	Dive speed	$[m/s]$
W	Weight	$[kg]$
w	Cross-sectional width	$[m]$
W_a	Aileron weight	$[N]$
W_{fle}	Fixed leading edge weight	$[N]$
W_{front}	Front wing weight	$[kg]$
W_{fte}	Fixed trailing edge weight	$[N]$
W_{lat}	Lateral wing weight	$[kg]$
W_m	Manoeuvre weight	$[N]$
W_{prim}	Primary wing weight	$[kg]$
W_{rear}	Rear wing weight	$[kg]$
W_{rib}	Rib weight	$[kg]$
W_{sec}	Secondary wing weight	$[kg]$
W_{slat}	Slat weight	$[N]$
W_{sp}	Spoiler weight	$[N]$
W_{tef}	Trailing edge high lift device weight	$[N]$
W_{to}	Maximum take-off weight	$[N]$
W_{wing}	Total wing weight	$[kg]$
X_{CG}	Longitudinal center of gravity position	$[m]$
X_{np}	Longitudinal neutral point position	$[m]$
$\tilde{x}\tilde{y}\tilde{z}$	Global coordinates	$[m]$
xyz	Local coordinates	$[m]$
$\bar{x}\bar{y}\bar{z}$	Local center of gravity position	$[m]$

GREEK

β	Relative sweep angle between rear wing and fin	$[deg]$
Δ	Spanwise element length	$[m]$
δ_{NO}	Non-optimum extra thickness	$[m]$
$\Delta_{W_{NO}}$	Non-optimum weight	$[N]$
Γ	Fin dihedral angle	$[deg]$
λ	Taper ratio	$[-]$
Λ	Sweep angle	$[deg]$
λ_{area}	Area ratio closed-wing	$[-]$
$\lambda^{(i)}$	Local direction cosine matrix	$[-]$
ϕ	Radius of gyration	$[-]$
ρ	Air density	$[kg/m^2]$
ρ_{mat}	Material density	$[kg/m^2]$
σ_{alw}	Maximum allowable normal stress	$[Pa]$
σ_{yield}	Normal yield stress	$[Pa]$
σ_i	Normal stress in boom i	$[Pa]$
σ_j	Normal stress in skin element j	$[Pa]$
τ	Average thickness to chord ratio	$[-]$
τ_{alw}	Maximum allowable shear stress	$[Pa]$
τ_{yield}	Shear yield stress	$[Pa]$

1

INTRODUCTION

The air traffic industry has historically shown significant annual growth rates of around 5% in North America and Europe. Propelled by impressive growth rates in Asia and the Middle East, the steady growth of the industry is expected to continue in the future. Currently, the air transportation sector contributes 3% to the global carbon emission, which could increase to 15% in 2050 with the described trends.[5]

IATA has recognised this problem and developed a vision for 2050. To reduce the strain of the industry on the environment they have set ambitious goals for the future. Aircraft in 2050 should be 70% more fuel efficient than their 2010 counterparts. Furthermore, the emission of nitrogen oxides should be reduced by 75% and take-off and landing noise should be drastically reduced. The vision indicates that major improvements in aircraft efficiency will have to come from radical new airframe designs.[6] The European commission also issued a report on the future of aviation, which is titled Flightpath 2050. Their goal is to reduce the CO2 emission per passenger kilometre by 75% in 2050 compared to 2000. The NOx emissions should be reduced by 90% and the perceived noise by 65%.[7]

Besides the long-term goals for 2050 IATA set targets for 2020 back in 2009, which were endorsed by the aviation industry. They include a required cap on aviation CO2 emissions from 2020 and an improvement in fuel efficiency of 1.5% per year from 2009 until 2020. A four-pillar strategy was adopted to reach those targets: improved technology, effective operations, efficient infrastructure and positive economic measures. They expect the first pillar, technology, to contribute the most towards the ambitious goals. However, after 2020 they expect radical new aircraft designs, different from the classical tube-and-wing architecture to reduce CO2 emissions by 25-50%.[8]

Research now focusses on finding new aircraft configurations, which could shape the future of aviation to reach the ambitous goals. One of the concepts being investigated is the PrandtlPlane configuration. The configuration, devised by Frediani et al., aims to reduce the induced drag with a closed-wing system, which is supported by two vertical tails.[9] An artist impression is shown in Figure 1.1. Previous investigations by Zohlandt into the configuration were aimed at comparing the performance of the PrandtlPlane to a conventional configuration for different mission requirements. The results indicated a lower fuel mass was required for the the PrandtlPlane compared to a conventional configuration. Furthermore, due to the closed-wing configuration higher payloads can be transported without increasing the total wingspan.[9] Constraints on maximum aircraft dimensions at airports currently limit the maximum transportable payload, which can thus be overcome by using closed-wing configurations.

The conceptual design of unconventional configurations brings challenges. Empirical relations used in conventional design processes are no longer viable and physics-based methodologies are therefore required. Furthermore, design workflows capable of handling both conventional and unconventional configurations should be developed to provide accurate comparisons. The Initiator design tool, developed at TU Delft aims to solve these problems, such that unconventional designs can be compared to their conventional counterparts.[10] The tool is currently capable of designing PrandtlPlanes, as shown by Zohlandt, but partly relies on conventional methodologies for the wing weight estimation, which reduce the reliability of the results.[11]

Additional background on the PrandtlPlane and its wing weight estimation is compiled in Chapter 2. The improvement points for the closed-wing weight estimation and PrandtlPlane design in the Initiator are determined, such that research goals can be defined in Chapter 3. The applied methodology is presented in

Figure 1.1: Artist impression of the PrandtlPlane configuration, adapted after [1].

Chapter 4, followed by its verification and validation in Chapter 5. The results are compiled in Chapter 6, from which the major conclusions are drawn in Chapter 7. The significance of the improvements made to the conceptual PrandtlPlane design in the Initiator is determined there. Finally, recommendations for the further improvement of the closed-wing weight estimation and the conceptual PrandtlPlane design in general are presented in Chapter 8.

2

BACKGROUND

The focus of this thesis will be on the wing weight estimation during the conceptual design of closed-wing configurations. In particular, the PrandtlPlane configuration will be analysed. The general lay-out and characteristics of the configuration are described in Section 2.1. The state-of-the-art in conceptual closed-wing design methodologies will be elaborated upon in Section 2.2. The characteristics of closed-wing weight estimations and the available methodologies and their drawbacks are investigated in Section 2.3.

2.1. CONCEPTUAL DESIGN OF PRANDTLPLANE CONFIGURATIONS

The PrandtlPlane configuration was devised by Frediani et al.[9] This closed-wing configuration is characterized by a lower front wing, a lateral wing and a high rear wing. The rear wing attaches to two vertical tail surfaces. The design features a twin engine configuration at the rear of the fuselage. The main advantage of this positioning is a small moment arm with the fuselage, which leads to good one engine inoperative performance. Another advantage is the that the wings are free of disturbances caused by the engines, which increases the aerodynamic efficiency of the configuration.[12] An additional difference with conventional configurations is the positioning of the landing gear. The front wing is positioned too far forward to house the main landing gear, while the rear wing is positioned too high. The main landing is thus positioned on the fuselage of the PrandtlPlane.[13]

2.1.1. AERODYNAMIC CHARACTERISTICS

The main advantage of closed-wing configurations is the induced drag savings they can provide. The best wing system described by Prandtl has the lowest induced drag for a given lift and span. The best wing system consists of a lower, upper and lateral wing. The induced drag savings for this configuration increase with the horizontal gap between the two wings. This relationship is shown in Equation (2.1).[14]

$$\frac{D_{i,bws}}{D_{i,m}} = \frac{1+0.45\frac{h}{b}}{1.04+2.81\frac{h}{b}} \tag{2.1}$$

To maximize the induced drag saving of the closed-wing configuration the vertical spacing between the wings should thus be maximized. This is one of the reasons why the rear wing in the PrandtlPlane configuration is attached at the tip of the vertical fins, instead of at the fuselage. Of course, the spacing is limited by practical considerations, but a spacing ratio of 0.2 can already reduce the induced drag by 30% compared to the equivalent monoplane.

Originally, Prandtl determined that the total lift should be distributed equally over the upper and lower wing to obtain the optimal design with the lowest induced drag.[14] More recent studies by Demasi et al. concluded through their analytical solution of the induced drag of the best wing system that the load repartition between the wings can be shifted without increasing the induced drag. An infinite number of solutions for the optimal circulation of the system exist, which consist of a fundamental reference solution and an arbitrary constant circulation.[15] Therefore, the lift partition between the two wings can be altered, without sacrificing the savings in induced drag. These findings increase the flexibility of the designer. Lift repartition

between the wings can be used to decrease the total wing weight or to obtain a more stable or controllable aircraft. Furthermore, Munk's theorem indicates that the horizontal wings can be swept or shifted longitudinally without penalties to the induced drag.[16]

2.1.2. STRUCTURAL CHARACTERISTICS

Three main differences between open and closed-wing structural characteristics can be distinguished. These characteristics will be used as a guideline in Section 2.3 to determine the strengths and drawbacks of current closed-wing weight estimation methodologies.

OVER-CONSTRAINED STRUCTURE

The closed-wing PrandtlPlane configuration is over-constrained from a structural point of view. A conventional wing can be modelled as a beam that is clamped at the fuselage and free at the tip. The structure is therefore statically determinate. Closed-wings however, have more constraints applied to the structure. The number of unknown reaction forces in these structures is larger than the number of equilibrium equations. The internal loads in these statically indeterminate structures depend on the stiffness of the elements, which in turn depend on the internal loads. Therefore, a stiffness iteration loop is necessary to size the primary wing structure of closed-wings. The additional loop to let the design of the structure converge increases the computational time required by closed-wing weight estimators compared to their conventional counterparts. While the required number of iterations is dependent on the specific case and stopping criteria, most tools tend to converge in ± 30 iterations.[2][17]

TILTED BENDING AXIS

In conventional wing weight estimations, the chord-wise bending moments and shear forces are generally neglected. In closed-wing configurations however, these moments and forces can be significant. Depending on the geometry of the configuration, they can be higher than the out-of-plane bending moments and shear forces at some locations along the wingspan.[2] These loads are mainly induced by the over-constrained nature of the structure and its geometric lay-out, instead of by external drag forces. Due to the inclusion of these secondary moments the bending axis of the closed-wing cross-sections are not parallel to the airfoil chord line, but are a tilted. If the lightest design, with the highest moment of inertia is to be obtained, the material should be placed as far away from the bending axis as possible. Therefore, closed-wing cross-sectional designs often feature additional material in the wingbox corners. The area of the flange supports if often cross-coupled in closed-wing designs.[18][2] Dal Canto et al. determined that adding cross-coupled flange supports to the cross-sectional design reduced the wing weight by 13.75% compared to a symmetric, conventional wingbox design.

CONSTRAINT DEFINITIONS

The over-determined structure and tilted bending axis are seen in all closed-wing configurations. However, the constraint definition of the PrandtlPlane is unique for this design. The structural design consist of half a wing, cut through the symmetry plane. Two approaches exist for modelling the PrandtlPlane constraints definition.

In both cases the root of the lower wing is clamped to the fuselage, while a symmetry constraint is applied to the root of the rear wing. Rigid connections between the main and lateral wings were found to lead to the lowest total structural weight by Jemitola.[19] This analysis focussed on a static structural analysis. If instabilities are taken into account, other lateral wing connection might prove to be optimal. However, these configurations are not taken into account in this research. The first option in modelling the fin is to clamp it to the fuselage at its root and connect it to the rear wing with a rigid connection. The approach is shown in Figure 2.1a. The disadvantage of this method is that the stiffness of the fin should be known, since the internal loads in the entire structure depend on the stiffness of the elements. Another possible solution is shown in Figure 2.1b, in which the fin is modelled as a support constraint to the rear wing. This support would be set under the angle at which the fin attaches to the rear wing. The fin is then regarded as a beam with infinite stiffness in tension and compression. The benefit of this solution is that the exact stiffness of the fins, which are sized for lateral manoeuvres, is not required as input for the wing weight estimation. Both approaches will be implemented in the methodology, but the second one will be used for the analyses in Chapter 6.

2.1.3. ADDITIONAL CONSIDERATIONS

The closed-wing design not only has an influence on the weight of the wings, but also on the fuselage. The fuselage can be seen a beam supported by both the front and rear wing. The maximum bending moment in

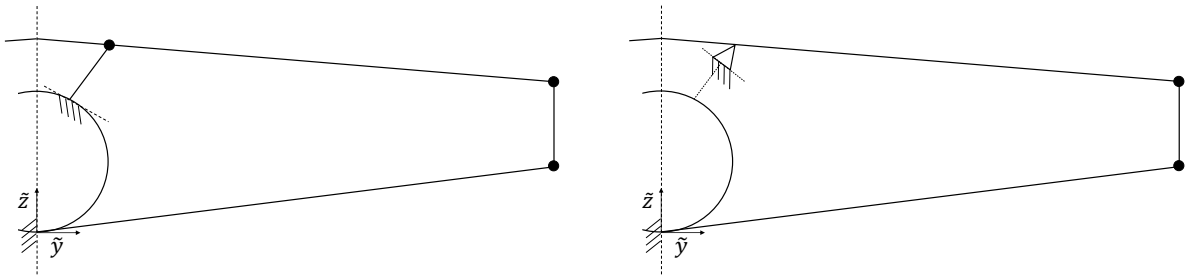

(a) Constraint definition including the fin as beam element.

(b) Constraint definition with the fin as support.

Figure 2.1: Constraint definition of the PrandtlPlane structural wing model.

the fuselage can thus be reduced by altering the longitudinal position of the wings.[9]. Preliminary results in a case study by Oliviero and Frediani seem to verify this theory. Fuselage weight savings of about 7.5-10% are found compared to the equivalent monoplane configuration.[20]

The maximum allowable wingspan at most airports is 80m, which limits the maximum capacity of transport aircraft. Closed-wing configurations can attain a higher wing reference area for a given wingspan, since two wings are used.[9] High payload, low range missions could thus prove to be a promising opportunity for PrandtlPlanes.

A disadvantage of the closed-wing is the limited fuel volume that can be stored in the wings. Compared to the equivalent monoplane, with equal span and area, the chord lengths of the PrandtlPlane wing are halved. If the thickness over chord ratio does not change between the configurations, a conventional wing can hold four times as much fuel as one PrandtlPlane wing.[13] Since the configuration uses a front and a rear wing the total fuel volume in the PrandtlPlane wings is approximately half of that in a conventional wing. This effect was verified by Voskuijl and De Klerk, who found that additional fuel tanks in the fuselage were necessary in their design study.[12]

Van Ginneken performed an investigation into the optimal control surface lay-out for PrandtlPlanes configurations. His findings indicate that separate pitch and roll control is preferred over combined control. The best configuration includes inboard elevators and outboard ailerons on both the front and rear wing. Both the ailerons and elevators can be used for longitudinal control, while rudders in both the fins ensure yaw control.[21]

2.2. EXISTING CONCEPTUAL DESIGN METHODOLOGIES

Three different conceptual closed-wing design methodologies are discussed in this section. The main goal is to determine the strengths and drawbacks of these design flows during the conceptual design. The first workflow, developed by Jemitola, is a conceptual design methodology for medium range closed-wing aircraft.[19] Secondly, the Initiator framework developed at TU Delft, which was extended by Zohlandt to allow for the design of PrandtlPlanes, will be discussed.[11] Finally, a design tool by Salam & Bil will be included in the comparison. The tool uses a physics-based analysis for both the aerodynamic and structural wing design.[22]

To accurately asses the viability of the PrandtlPlane configuration a conceptual design workflow should meet several requirements. The general workflow should be able to handle both closed-wing and conventional configurations for a range of mission requirements, such that an accurate comparison can be made. Furthermore, accurate and design sensitive weight estimations for the wings and fuselage should be included, which take into account the constraint definition of the PrandtlPlane. Furthermore, an aerodynamic analysis should be included, which is linked to a stability and control module. Finally, the ability to repartition the lift between the front and the rear wing could improve the performance of the designed aircraft considerably. The three different closed-wing conceptual design methodologies have been compared to determine if they meet these requirements. The results are compiled in Table 2.1.

None of the design tools meets all criteria, necessary for an accurate closed-wing conceptual design methodology. Apart from the wing weight estimation method, the Initiator was determined to be the most complete and flexible tool to assess the viability of the PrandtlPlane concept with respect to conventional aircraft.

The Initiator is developed at the TU Delft to quickly come up with an initial design from a set of global mission requirements and constraints. A detailed description of the methodology is included in Section 4.2.

Table 2.1: Summary of the methodologies which were investigated

	Jemitola[19]	**Initiator[11]**	**Salam & Bil[22]**
Handles changing mission requirements	✓	✓	✓
Handles closed-wing and conventional configurations	X	✓	✓
Handles PrandtlPlane configurations	✓	✓	X
Includes accurate aerodynamic analysis	✓	✓	X
Includes accurate wing weight estimation	X	X	✓
Includes accurate fuselage weight estimation	X	✓	X
Includes stability and control analyses	✓	✓	X
Deals with unequal lift distribution between the wings	X	X	X

Currently, the tool is capable of designing PrandtlPlanes, but relies on conventional methodologies for the weight estimation of the wings. The next big step in testing the viability of PrandtlPlanes thus seems to develop a physics-based wing weight estimation method that can be used in the Initiator. This method should take into account all structural characteristics mentioned in Section 2.1.2. Finally, the possibility of using an unequal lift distribution between the front and rear wing should be incorporated in the design flow to determine its effect on the PrandtlPlane performance.

2.3. EXISTING CLOSED-WING WEIGHT ESTIMATIONS

It was determined that the most critical point of attention in the conceptual design of closed-wing configurations is the unreliability of current wing weight estimation methodologies. The main goal of this thesis is thus to improve the wing weight estimation of closed-wing configurations during the conceptual design stage. Therefore, background on existing closed-wing weight estimations is included in this section. The methodologies of the three design flows discussed in Section 2.2 will be elaborated upon, together with a methodology by Andrews et al.[2]

2.3.1. JEMITOLA

Jemitola proposes an adapted solution of Howe's conventional wing weight estimation equation. The modified Equation (2.2) reads as follows.[19]

$$M_W = C_1 \left[\frac{bS}{\cos \Lambda_{1/4}} \left(\frac{1+2\lambda}{3+3\lambda} \right) \left(\frac{M_{TOM} N}{S} \right)^{0.3} \left(\frac{V_D}{\tau} \right)^{0.5} \right]^{0.9} \tag{2.2}$$

The coefficient C_1 is based on the type of aircraft that is being considered. Jemitola's goal is to find two values for this factor; one for the front and one for the aft wing. Ten slightly different box wing aircraft designs were selected for the procedure. The fore and aft wing were unjoined and their wing weight was calculated using Howe's empirical formula. For the same wings, a finite element analysis was performed to find the weight of the torsion box. The empirical and finite element results were compared and a regression equation was deduced. Furthermore, the same finite element analysis was applied to the joined wing to form a regression equation as well. The results correlated well ($R^2 > 0.99$) and the resulting coefficients were found to be equal for both the fore and aft wing. C_1 is 0.028 for both wings.

Two main drawbacks can be identified in Jemitola's approach. First, the model has been specifically designed to evaluate medium range PrandtlPlane aircraft. It is unrealistic to assume that a single coefficient would hold for all PrandtlPlane configurations. The method is therefore not applicable to a larger range of designs, which limits its use in a conceptual design tool. Furthermore, the original equation uses a certain set of input parameters to which the wing weight of a conventional aircraft is sensitive. Jemitola assumes that the same set of parameters, in the same equation, can capture this sensitivity for a PrandtlPlane as well. However, this is not necessarily true. The methodology is therefore not expected to produce accurate, design sensitive results in a conceptual design workflow.

2.3.2. ZOHLANDT

Zohlandt uses the class II.1/2 EMWET tool designed for conventional aircraft to estimate the wing weight of PrandtlPlanes.[23][11] This wing weight estimation was developed for conventional configurations and can estimate their wing weight with an average error of less than 2%.[23] Zohlandt splits the PrandtlPlane

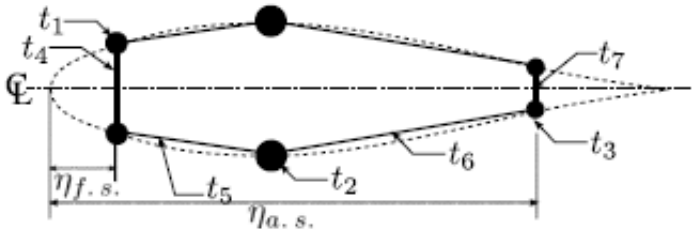

Figure 2.2: A cross-sectional view of the boom and skin model used by Andrews et al.[2]

configuration in three separate surfaces. The weight of the front and rear wing are determined, as if they are conventional wings, with EMWET and a factor is added for the connection element. This is shown in Equation (2.3).

$$W_{lat} = 0.11\left(W_{front} + W_{aft}\right) \tag{2.3}$$

A few notable drawbacks can be identified. First, the empirical factor for the lateral wing weight is unlikely to hold for all aircraft sizes and mission requirements. Secondly, by splitting the wing in two separate wings, none of the closed-wing structural characteristics mentioned in Section 2.1.2 are taken into consideration. Finally, closed-wings are not necessary sensitive to the same design parameters as conventional wings. The methodology is therefore not design sensitive or accurate enough to be applied in conceptual closed-wing design stages.

2.3.3. SALAM & BIL

Salam & Bil use the weight estimation tool wingMASS developed by Dorbath at DLR for the wing weight estimation in their conceptual design flow.[22][24] The tool is capable of handling both conventional as well as closed-wing configurations and takes the structural characteristics defined in Section 2.1.2 into account. Dorbath opts to use a combination of beam and shell elements in a finite element analysis. The structural analysis and sizing routines are performed in ANSYS to find the optimal material distribution. A non-optimum mass factor, which is based on a regression analysis with existing aircraft, is included at the end of the optimization, while the secondary structural weights are estimated using a physics-based approach.

An analysis of a conventional primary structure takes 45 seconds. This indicates that a complete finite element analysis for the primary weight, in which a stiffness iteration loop should be included, is too extensive for a closed-wing configuration. Including the physics based secondary weight estimation, ramps up the computational time to 24 minutes, which is unacceptably long in a conceptual design study.

2.3.4. ANDREWS ET AL.

The wing weight estimation method by Andrews et al. can be applied to both planar and non-planar configurations. The notable difference with the previously discussed models is the use of a different cross-sectional design in the equivalent beam finite element model to determine the internal forces and moments. It sizes the primary structure using a fully stressed design, stiffness iteration loop. The secondary wing weights are determined with empirical relationships.[2]

The equivalent beam model consists of two-node beam elements with six degrees of freedom per node. The loading cases include the aerodynamic manoeuvre loads, an inertial load factor and a fuel load. A boom and skin model is applied as cross-sectional definition. The booms are positioned at the front spar, aft spar and the location with the maximum displacement on the suction surface. Symmetry is applied about the chord-line of the airfoil. The cross-sectional design is shown in Figure 2.2.

The booms are sized to withstand the axial forces and bending moments, while the skins withstand the shear forces and torsional moments. Note that an iterative procedure takes place in sizing the booms, since the centre of gravity shifts when the boom areas are altered. No unique solution exists for the areas of the six booms, therefore their areas were assumed to be proportional to their distance to the centre of gravity. The methodology by Andrews et al. can take both conventional and unconventional aircraft as input. While conventional designs can be analysed within 3 seconds, closed-wing configurations take up to 30 seconds.

An assumption that could be challenged is the hexagonal boom and skin model for the cross-sectional design. The drawback of the skin and web model with reinforced flanges is the fact that the height of the webs

has to be chosen rather arbitrarily according to Andrews et al. and that the final shape does not necessarily fit in the airfoil.[2] The argument, that the wing box does not necessarily fit in the wing, is not important during conceptual design however. The main goal of the tool is to find an accurate wing weight estimation, which does not require the wing box to fit in the wing. Furthermore, the cross-section by Andrews et al. is symmetric around the airfoil chord, while the optimal distribution to cope with the tilted bending axis was determined to be asymmetric.[25][26] Their model also requires Andrews et al. to make the assumption that the area of a boom is proportional to its distance from the center of gravity, since multiple solutions for the boom areas exist in the hexagonal model. In conclusion, the benefits of the more complex model are questionable and should be validated before accepting it as superior.

Finally, the method has some other limitations that might hamper its performance in a conceptual design phase. Only one type of wing loading is considered in the research: a case where both the front and the rear wing are loaded equally. Changing the wing loading between the two wings induces completely different internal loads into the structure, especially in the lateral element. The tool has not shown the capability of coping with these kinds of configurations. Furthermore, Andrew's research is focussed on a case where both the front and rear wing are rigidly attached to the fuselage and can thus not handle PrandtlPlane configurations. The flexibility to deal with different configurations is crucial in the early stages of a design process. The possibility to deal with changing boundary conditions and thus PrandtlPlanes could be a great addition to the tool.

OVERVIEW

In conclusion, none of the four methodologies discussed in this section incorporate all structural characteristics of closed-wing weight estimations, which were outlined in Section 2.1.2. It can be concluded that physics-based secondary weight estimations are out of the conceptual design scope. Furthermore, the methodology should be able to handle the specific constraint lay-out of a PrandtlPlane configuration and take into account the secondary bending moments and shear forces. Finally, the primary wing weight should be determined in an iterative procedure, since the internal loads in the design depend on the sizing of its elements. The main goal of this thesis is thus to improve the closed-wing weight estimation, such that the conceptual design of PrandtlPlanes in the Initiator can be performed more accurately.

3

Research Goals and Objectives

In Chapter 2 limitations in existing conceptual design methodologies and corresponding closed-wing weight estimations were determined. In order to address these issues, research questions are set up in Section 3.1. In Section 3.2 the necessary steps and objectives to answer these questions are elaborated upon.

3.1. Research Goals

The goal of this project is to improve the conceptual design of closed-wing configuration by providing a new wing weight estimation, conceived to overcome the limitations of the conventional Class II-1/2 methodology that is currently used in the Initiator. Existing tools are either too computationally intensive, or unable to handle over-constrained structures with a tilted bending axis. Furthermore, no tool exists that can estimate the wing weight of PrandtlPlane configurations, which are characterized by two vertical tails connecting to the rear wing. Research in recent years has also pointed to the fact that it is not necessary to keep the lift partition between the front and rear wing equal to achieve optimal aerodynamic performance.[15] The lift distribution might thus be altered to achieve a lighter wing structure or a more stable design, without sacrificing aerodynamic performance.[15][27] However, none of the design methodologies investigated in Section 2.2 incorporate the lift repartition between the front and rear wing as a design variable. A second goal is thus to investigate the influence of altering the area distribution between the front and rear wing on the performance of the PrandtlPlane design. The following two main research questions should thus be answered.

1. *What is the influence of implementing a Class II-1/2 wing weight estimation method for closed-wing configurations on the wing weight and required fuel mass in the conceptual aircraft design?*
   (a) *What is the influence of the wing sweep angles, span and taper ratio on the total PrandtlPlane wing weight and its distribution?*
   (b) *What is the influence of the fin position and orientation on the total PrandtlPlane wing weight and its distribution?*
   (c) *What is the influence of the longitudinal center of gravity position and trim conditions on the total PrandtlPlane wing weight and its distribution?*
   (d) *What is the influence of the PrandtlPlane configuration versus a clamped rear wing on the total wing weight and its distribution?*
2. *What is the influence of varying the area distribution between the front and the rear wing on the required fuel mass in the conceptual design of PrandtlPlane configurations?*

3.2. Research Plan

Several distinct steps should be taken to answer the two main research questions formulated in Section 3.1. The overview of all activities is shown in Figure 3.1. First, a closed-wing weight estimator suitable for the conceptual design stages should be created. The estimation of the wing weight and its distribution should be as accurate as possible, with a reasonable computational time for the conceptual design stages. In practice,

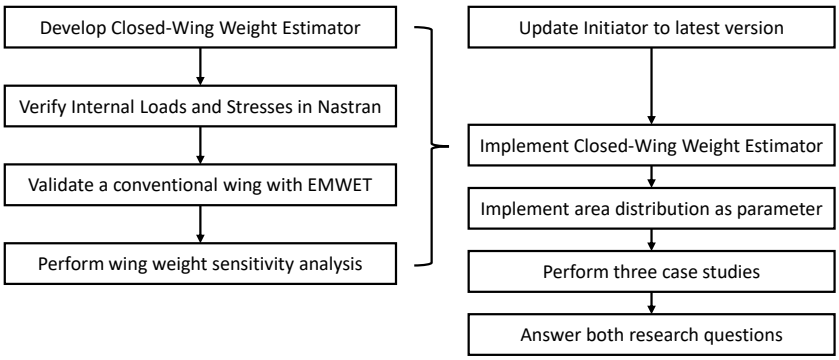

Figure 3.1: Overview of the main project objectives.

a Class II-1/2 module in the Initiator framework should have a required computational time under thirty seconds. The methodology shall include a physics-based estimation of the primary weight, which takes the closed-wing structural characteristics defined in Section 2.3 into account. A physics-based analysis of the secondary weights was determined to be too computationally intensive for the conceptual design stages. Therefore, secondary weights will be determined empirically.

The new closed-wing weight estimation methodology will be verified by comparing the internal loads and stresses with a finite element solution in Nastran. A validation is performed by comparing the results for two conventional configurations with the state-of-the-art Class II-1/2 conventional wing weight estimations of EMWET.[23] After the tool has been verified and validated some sensitivity analyses are performed. The goal of these analyses is to determine the influence of wing and fin design parameters on the total wing weight and its distribution. The sub-questions to the main research question can then be answered.

The development of the closed-wing weight estimation methodology is the main focus of this thesis. However, to determine the influence on the the overall conceptual design, the methodology is incorporated in the Initiator for PrandtlPlanes. The Initiator will be updated to the latest version and the area ratio between the front and rear wing is added as design parameter to be able to investigate its influence on the required fuel mass of the PrandtlPlane designs. Apart from these updates, the Initiator will be used as is and no further improvements to its methodology are implemented. Then, three case studies, with different mission requirements, will be performed to determine the influence of the new closed-wing weight estimator compared to the original method implemented in the Initiator. These results will be used to answer the main research questions.

4

METHODOLOGY

The detailed implementation of the research objectives defined in Chapter 3 is elaborated upon in this Chapter. The new semi-analytical closed-wing weight estimation methodology is discussed in Section 4.1. The overall methodology used for the conceptual design of the closed-wing configuration in the Initiator is shown in Section 4.2.

4.1. CLOSED-WING WEIGHT ESTIMATION METHODOLOGY

The goal of the closed-wing weight estimation methodology is to determine the total wing weight and its distribution as accurately as possible, while keeping the computational time under thirty seconds. Furthermore, the methodology should be sensitive to the design parameters of a PrandtlPlane wing. A general overview of the methodology is described in Section 4.1.1, followed by detailed elaborations in Sections 4.1.2 until 4.1.10.

4.1.1. CLOSED-WING WEIGHT ESTIMATION OVERVIEW

The general flow of the closed-wing weight estimation methodology is summarised in Figure 4.1, while a more in-depth flow of parameters and data within the program is shown in the N2-chart in Appendix A. Two input files are supplied to the pre-processing module at the start of the weight estimation. An initial wing model is then generated from these inputs. Aerodynamic, fuel and inertial relief loads are generated and applied to the structural model, after which the internal loads are determined. The cross-sections of all beams are sized to withstand these loads and the primary weight of the structure is updated. Since the closed-wing structure is over-constrained, a convergence loop is implemented. The stopping criteria for this loop is shown in Equation (4.1).

$$\frac{W_{i+1} - W_i}{W_i} < 10^{-6} \tag{4.1}$$

If the stopping criteria is not met, the self-relief weight of the wing is updated in the load generation module and the updated stiffness distribution is used to determine a new set of internal loads. This procedure is repeated until the primary weight of the wing has converged. The secondary weights are then estimated empirically and added to the primary weight to determine the total weight of the wing. Finally, a post-processing module compiles all results and generates visual outputs. In Sections 4.1.2 until 4.1.10 all relevant modules shown in Figure 4.1 will be discussed in more detail. A reference PrandtlPlane design will be used throughout this section to visualize the process.

4.1.2. PRE-PROCESSING MODULE

Two different input files are required for the tool: one file specifying the geometry and lay-out of the wing and one file specifying the variables to be used during the methodology. The detailed lay-out of these input files is shown in Figures 4.2a and 4.2b respectively.

In the geometry input file the wing is defined as a series of surfaces, defined by at least two sections. For these sections, the leading edge locations, chord length, twist angle, front and rear spar locations and airfoil name should be supplied. Furthermore, airfoil coordinate files should be supplied. In these files the x and y coordinates, normalized with the chord length, should be provided. The coordinates run from the trailing

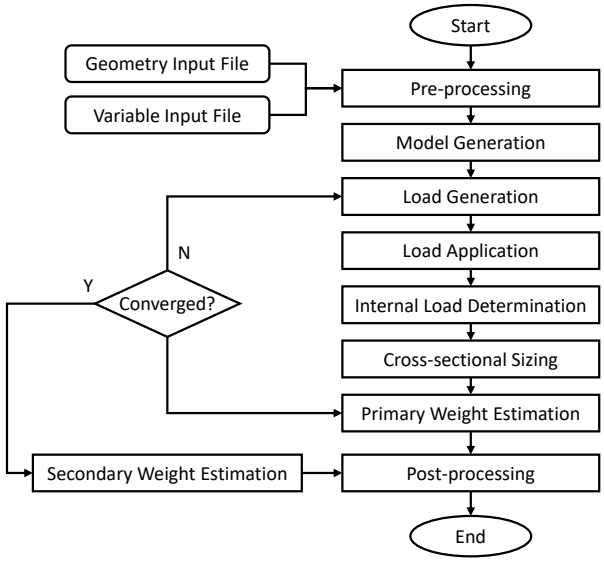

Figure 4.1: Overview of the closed-wing weight estimation methodology.

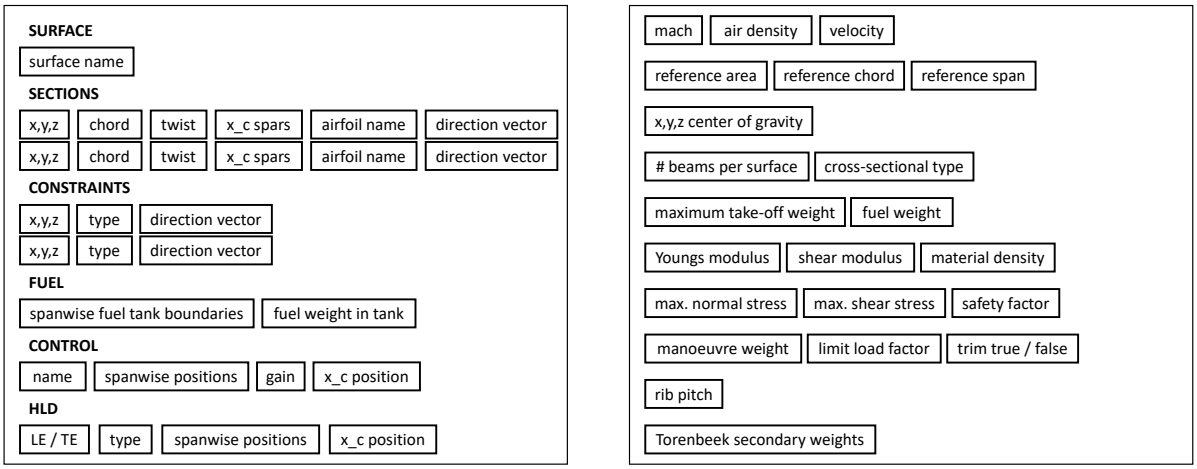

(a) Definitions for the geometry input file.

(b) Definitions for the variable input file.

Figure 4.2: Definitions for the input files of the closed-wing weight estimator.

edge (1,0) towards the leading edge along the upper surface (0,0) and back to the trailing edge along the lower surface(1,0). In the geometry input file, the direction of the upwards y-direction of the airfoil should be given, to define the orientation of the airfoil.

Constraints can be specified on each surface. For each constraint three inputs are required: the location in the global coordinate system, the constraint type and its direction vector in global coordinates. Possible constraints include: clamped, symmetry, support and rigid connections. These constraints will be applied to the structural model, when the internal loads are determined.

Information on fuel tanks, control surfaces and hight lift devices is optional input. If the spanwise position of a fuel tank and its weight are supplied, the corresponding fuel relief loads will be taken into account. The spanwise and chordwise position of control surfaces can be given, along with its name and gain. If multiple control surfaces with the same input name are supplied, the load generation module will treat them as a single, coupled control system with the appropriate gains. Information on high lift devices is only used for the empirical secondary weight estimation.

The second input file required by the program contains all relevant variables. The flight conditions and reference dimensions are required inputs. The center of gravity location input is optional and only necessary if the aircraft is to be trimmed in the aerodynamic analysis. The trim condition can also be entered in this

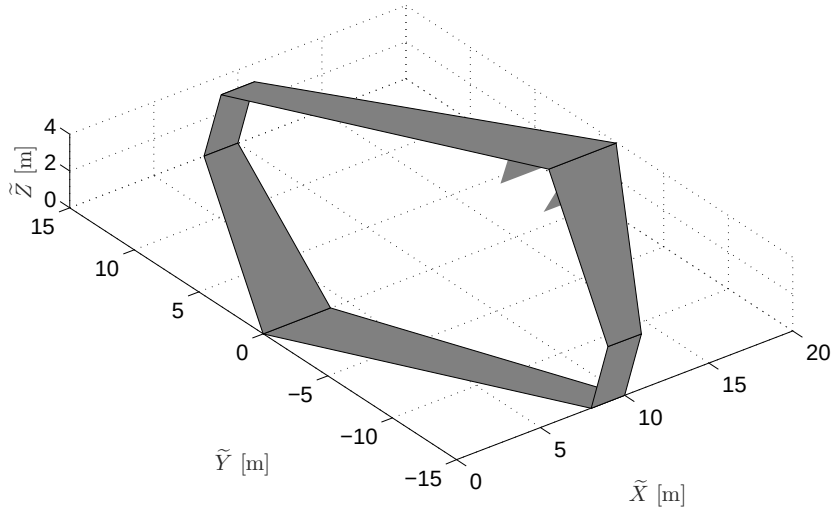

Figure 4.3: Lay-out of the reference PrandtlPlane wing design considered in this chapter.

file. Note, that trimming is only possible when the elevators have been defined in the geometry file described before. The number of beams for the structural discretization of each surface is an input as well. Fuel weight, manoeuvre weight and a limit load factor should be supplied such that the loading condition can be determined. The material properties for the wing box are specified along with a factor of safety. Finally, rib pitch is necessary if Torenbeek's secondary weight estimation methodology is to be used. This choice can be made by varying the last input parameter.

The input files for the reference case, which will be used to visualize a complete weight estimation in this section, are compiled in Appendix B. The corresponding shape of the wing is shown in Figure 4.3.

4.1.3. MODEL GENERATION

In the model generation module an initial model of the wing is created. First, nodes are created at every section and constraint definition specified in the geometry input file. Linearly spaced nodes and beams are placed in between these locations to reach the specified number of beams per wing surface. The nodes, which have six degrees of freedom, are connected by beam elements. The definition of the beam elements is shown in Figure 4.4b. The nodes are positioned along the midpoint of the front and rear spar as shown by the dotted line in Figure 4.4a. The local x-axis runs along the elastic axis, while the local y-axis points in the global x-direction but is rotated to account for sweep and dihedral. The local z-axis is oriented such that the right-handed coordinate system is completed.

At each node, a position, chord length, twist, spar location and a set of airfoil coordinates are defined using a linear interpolation between the input sections. The cross-sectional design of the beams is shown in Figure 4.8. The geometric height and width of the rectangular cross-section are defined at each node. The height of the cross-section will be updated during the cross-sectional sizing, as will be explained in Section 4.1.7. The width of the element is defined as the distance between the front and rear spar, while accounting for the local sweep angle as shown in Figure 4.4a. Finally, initial sizing parameters are applied to all beam elements for the first iteration of the convergence loop.

After this procedure has been carried out for all separate wing surfaces, global nodes are defined. In this set of nodes all duplicate local nodes are removed. The model keeps track of which nodes align with a global node, such that they can be connected in the structural analysis. All constraints from the input file are linked to their respective global node in this procedure. The final result is a system of global nodes and constraints, which are connected by beams. For both the nodes at the start and end of each beam the following parameters are defined: a global position, chord length, twist, spar location, height, width, enclosed cross-sectional area and a set of airfoil coordinates.

The model containing all global global nodes for the reference case is shown in Figure 4.5. The attachment location of the fin is shown by the red dot on the rear wing. The front wing is clamped to the fuselage and a symmetry constraints is applied to the root of the rear wing.

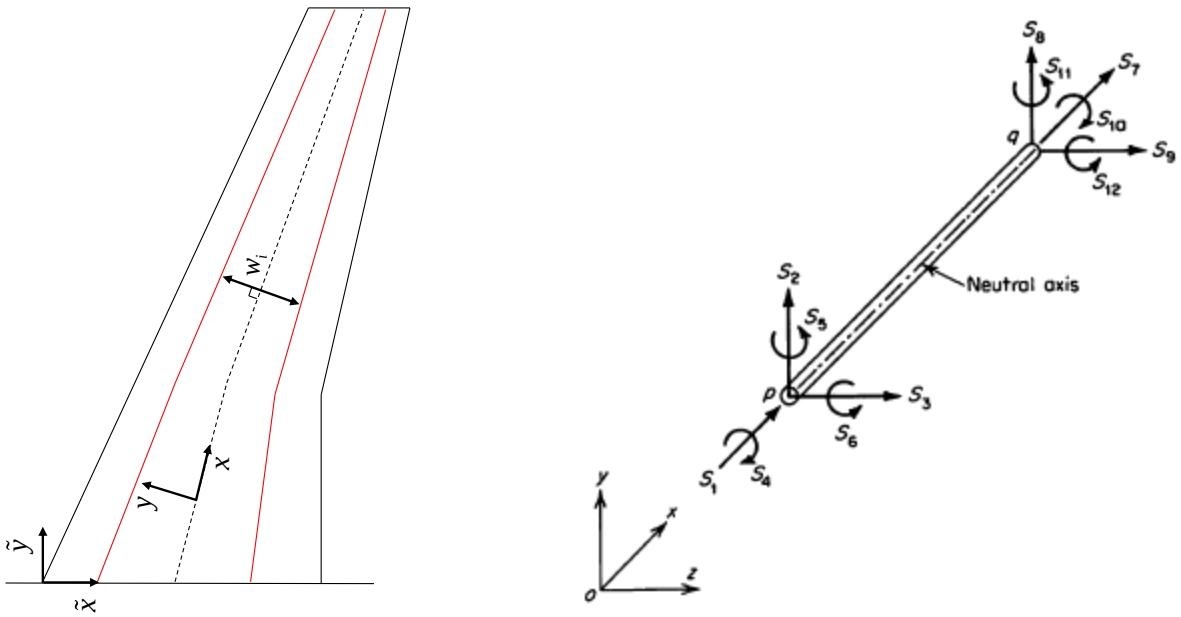

(a) Beam positioning along the wing.

(b) Beam element loads definition.[3]

Figure 4.4: Definition of the equivalent-beam model.

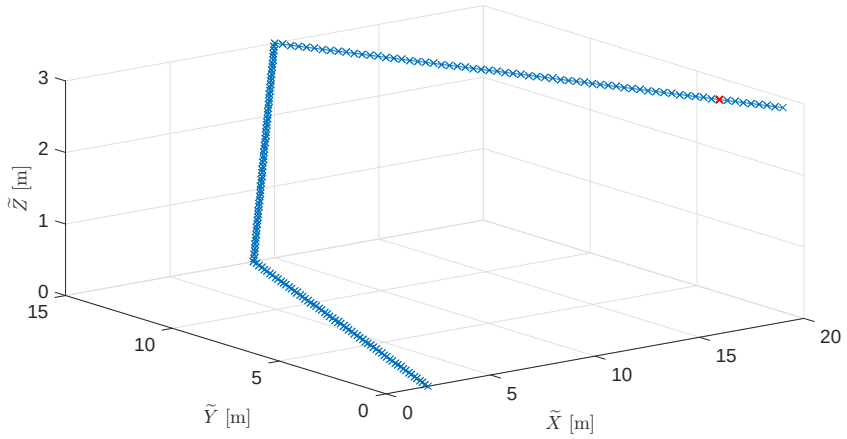

Figure 4.5: Global nodes model for the reference case.

4.1.4. LOAD GENERATION

Three types of loads are considered in the weight estimation analysis: aerodynamic loads, fuel relief loads and inertial relief loads. The aerodynamic loads acting on the structure are determined using the vortex lattice solver AVL. The geometry of the system is written to an input file. Each surface is given the same component segment definition, such that AVL treats them as a single component. Twenty spanwise and chordwise elements are defined for each surface. The geometry, chord lengths and twist angles can be easily derived from the model, which was generated in the previous module. If it is indicated in the input file that the configuration should be trimmed, the position of the control surfaces is included in the AVL input file as well. If no wing section exists at the spanwise start or end location of the control surface, a linear interpolation is performed to define a new wing section in the AVL input file. The chordwise hinge position and gain of the control surface are copied directly from the tool input file. The required lift coefficient at the given loading condition is computed using Equation 4.2.

$$c_L = \frac{2NW_m}{\rho V^2 S} \tag{4.2}$$

AVL is ran at the required lift coefficient, and if trimming is necessary a condition of zero pitching moment

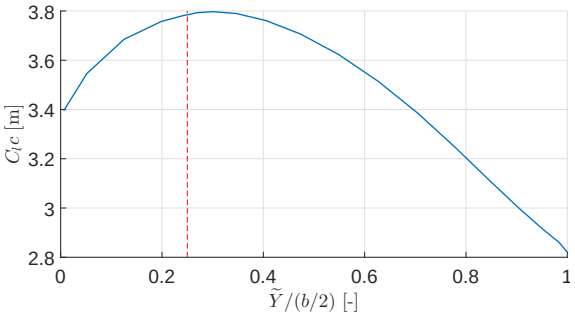

(a) Local lift coefficients on the front wing.

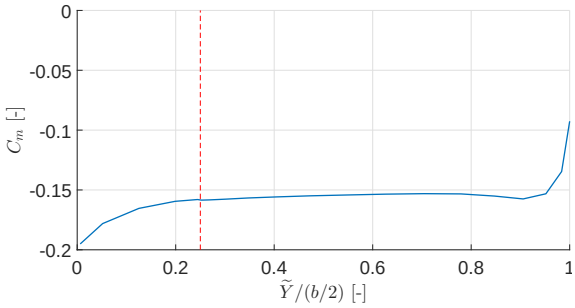

(b) Local moment coefficients on the front wing.

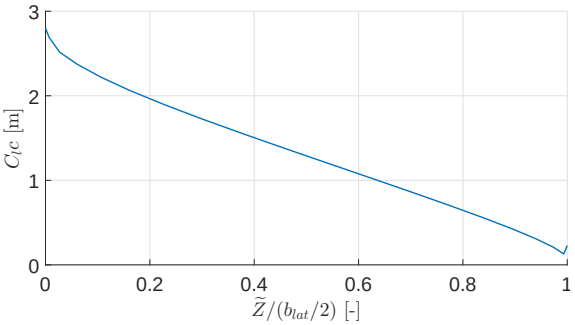

(c) Local lift coefficients on the lateral wing.

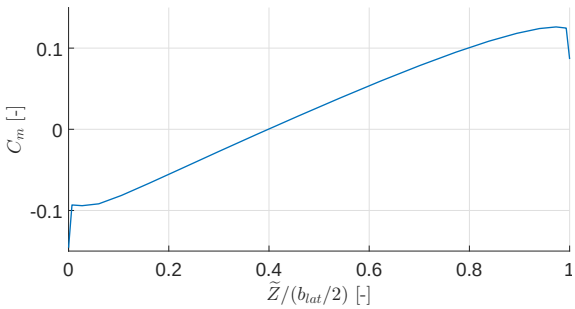

(d) Local moment coefficients on the lateral wing.

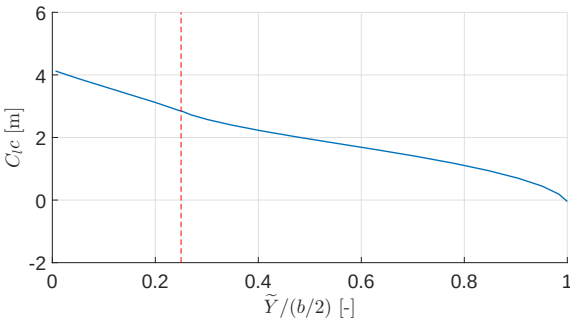

(e) Local lift coefficients on the rear wing.

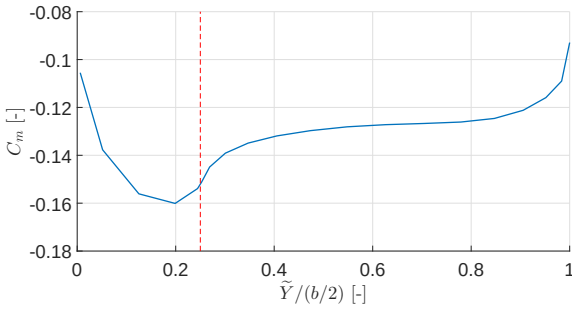

(f) Local moment coefficients on the rear wing.

Figure 4.6: Local lift and moment coefficients for the reference case.

is included. After the solution has converged, the distribution of local lift and moment coefficients on each wing surface is extracted from the AVL output files.

The local lift and moment coefficients for the three wing surfaces of the reference case are shown in Figure 4.6. The red dotted lines indicate the end position of the elevator on the wing. The elevator on the rear wing has deflected downwards, leading to the increase in local lift coefficient seen at the root in Figure 4.6e. The opposite effect is visible at the root of the front wing, due to a small upwards elevator deflection. The effect of the elevator deflection is also visible in the distribution of the moment coefficients on the front and rear wing. The airfoil and chord length of the lateral wing were selected equal to those at the tips of the front and rear wing. Therefore, a smooth transition is visible in local lift and moment coefficients from the main wings to the lateral connection. The distribution thus looks as expected for a best wing system.

Fuel loads provide a relief to the structure and are thus taken into account. The total fuel weight is specified as input in the variable input file. By using the spanwise fuel tank locations in the geometry input file and the cross-sectional area distribution defined in the model generator, the amount of fuel at each beam can be defined. It is assumed that the distribution of the fuel in the tanks varies linearly with the cross-sectional area of the elements. The fuel weight is multiplied with the limit load factor, since the fuel experiences the same acceleration as the wings of the aircraft.

The inertia relief of the wing weight is also accounted for. After each iteration of the stiffness loop the weight of the beams is updated. The weight of a beam is multiplied by the limit load factor to determine the

inertial relief loads at that element.

4.1.5. LOAD APPLICATION

All loads which are generated by the load generation module should be applied to the global structure. The aerodynamic properties from AVL are defined at different spanwise locations than the structural grid is defined at. Therefore, a spline interpolation is performed to define the lift and moments coefficients at the center of each beam element. By applying Equation (4.3) a force and moment can be defined at the quarter chord, spanwise midpoint of each beam element. In which Δ is the spanwise length of the local beam element.

$$F = q c_l c \Delta \tag{4.3}$$

$$M_{c/4} = q c_{mac} c_m c \Delta \tag{4.4}$$

Each aerodynamic force and moment is rotated with the dihedral angle of the specific wing surface to define the forces and moments in the global reference system, shown in Figure 4.4a. The structural nodes are positioned midway between the front and rear spar. Therefore, the aerodynamic forces should be moved from the quarter chord position onto the structural grid. The total moment at each beam center is then composed of two contributions: the moment around the quarter chord point and the moment due to the offset between the quarter chord point and the elastic axis of the beam.

$$M = M_{c/4} + F \times \left(\begin{bmatrix} \tilde{x} & \tilde{y} & \tilde{z} \end{bmatrix}_{node} - \begin{bmatrix} \tilde{x} & \tilde{y} & \tilde{z} \end{bmatrix}_{c/4} \right) \tag{4.5}$$

At this point, the aerodynamic loads, fuel loads and relief loads are defined at the center of each beam element. To define them at the structural nodes they should be distributed to the start and end node of the beam. Half of the force, and half of the moment applied to each beam is positioned at the start node and the other half at the end node. If multiple forces are applied to the same global node their contributions are summed.

The total external loads applied at the global nodes of the reference PrandtlPlane are shown in Figure 4.7. The global nodes run from the lower wing root to the tip, up along the lateral wing and then inwards from the upper wing tip to the root. The black dotted lines in Figure 4.7 indicate a start of a new surface, while the red line shows the location of the fin support constraint.

As expected, no external loads are present in the global x-direction, since drag forces are neglected. The loads on the front and rear only act in the global-z direction, because no dihedral angle is present in the reference case. Due to the opposite sweep angles of the wings, with a backwards swept rear wing and a forward swept front wing, a lift discrepancy between the surfaces exists. The total load on the front wing is higher than on the rear wing. The loads on the lateral connection element act inboard, as expected in a best wing system.

4.1.6. INTERNAL LOAD DETERMINATION

The beams in the structural definition consists of two nodes, which each have six degrees of freedom. The lay-out of such a beam and the definition of the internal loads is shown in Figure 4.4b. The cross-sectional definition of the beams is shown in Figure 4.8. The cross-section consists of four booms and four skins. Opposing booms are coupled to have the same areas, while all skins are sized separately. Six unknowns per beam cross-section should thus be determined. The choice for this cross-sectional design is further elaborated upon in Section 4.1.7. The positioning of the elements with respect to the global coordinate system is shown in Figure 4.4a. The local x-coordinate is positioned along the beam element. The local y-coordinate points in the negative global x-direction, but is rotated to account for sweep and dihedral. The local z-coordinate is then positioned to complete the right-handed coordinate system.

To determine the internal loads in each of the beam elements the matrix displacement method is employed. An overview of this methodology is shown in Figure 4.9.

First, the three-dimensional local stiffness matrices, shown in Equation (4.6), are defined for each beam element. The matrix links the forces and moments at both the first and second node of the beam to their respective displacements, such that a twelve by twelve matrix is created. The radii of gyration ϕ_y and ϕ_z are assumed to be zero, since the beams are slender. Shear deformations are thus neglected.[3]

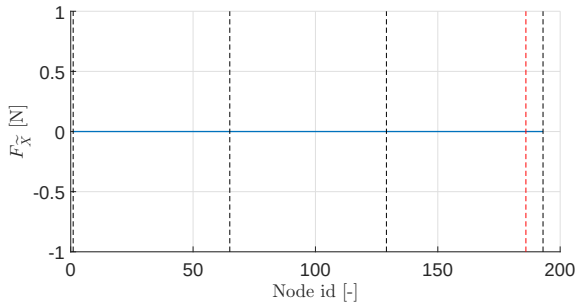

(a) External forces in $\widetilde{X}$.

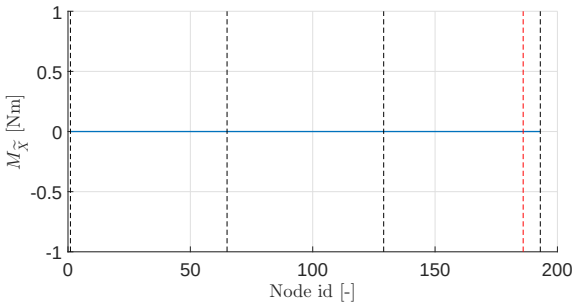

(b) External moments around $\widetilde{X}$.

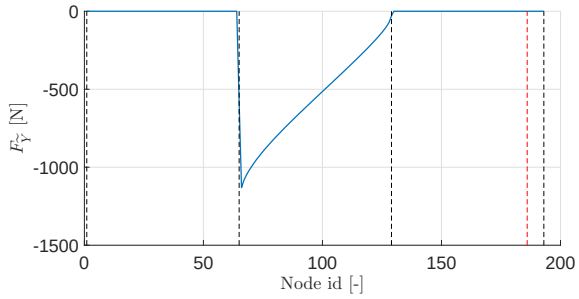

(c) External forces in $\widetilde{Y}$.

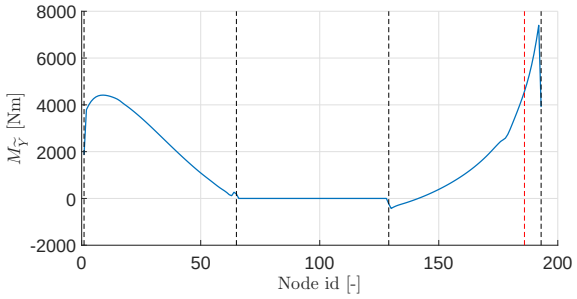

(d) External moments around $\widetilde{Y}$.

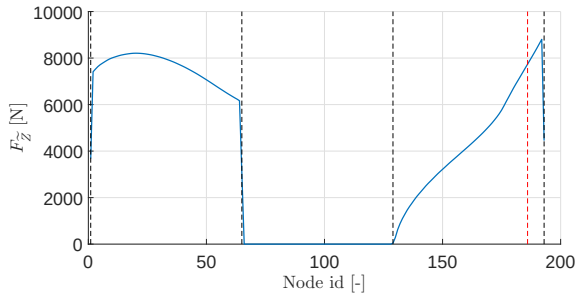

(e) External forces in $\widetilde{Z}$.

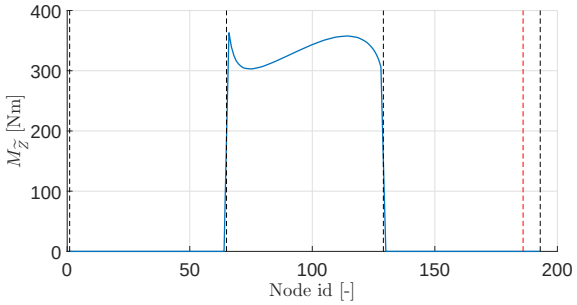

(f) External moments around $\widetilde{Z}$.

Figure 4.7: External loads applied to the global nodes of the reference PrandtlPlane.

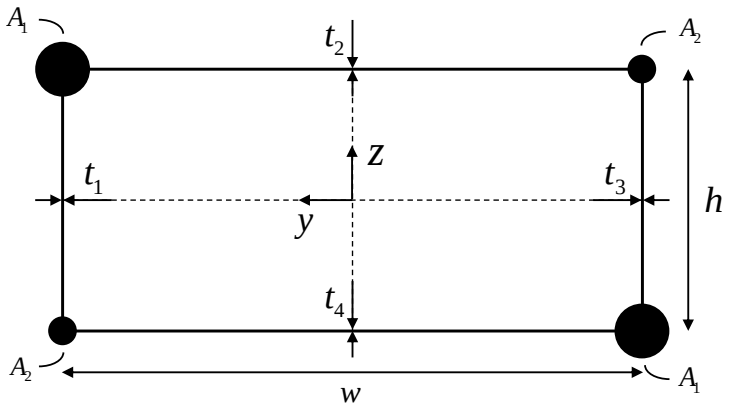

Figure 4.8: Cross-sectional beam definitions.

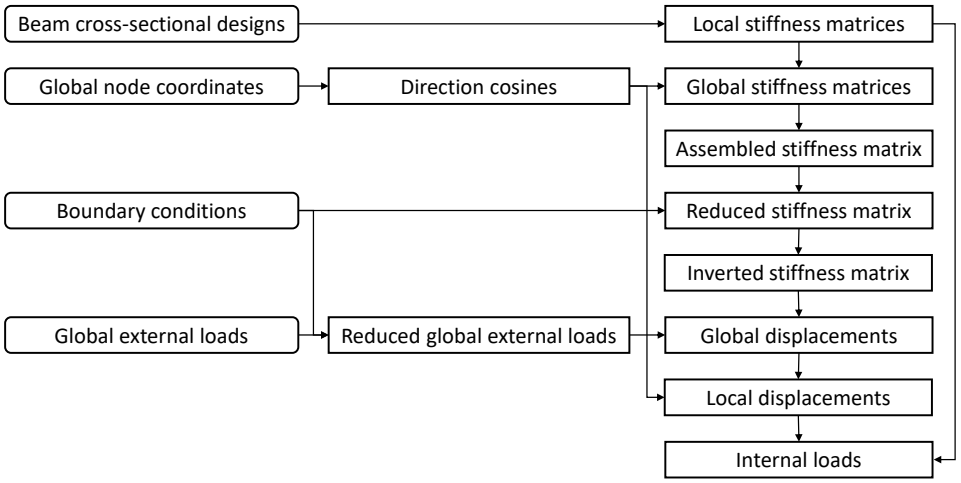

Figure 4.9: Overview of the stiffness method to determine the internal forces and moments, adapted after Przemieniecki.[3]

The Young's and shear modulus of the material are direct inputs into the tool, while the length of the beam is deduced from the structural model. The moments of inertia around both axes, the cross-sectional area and the polar moment of inertia of each beam are computed from the model. Since the cross-section is rectangular and opposing booms are assumed to be of equal area the moment of inertia relations reduce to Equations (4.7) and (4.8).

$$I_y = \sum_{i=1}^{4} A_i (z_i - \bar{z})^2 = 2\left(\frac{h}{2}\right)^2 (A_1 + A_2) \tag{4.7}$$

$$I_z = \sum_{i=1}^{4} A_i \left(y_i - \bar{y}\right)^2 = 2\left(\frac{w}{2}\right)^2 (A_1 + A_2) \tag{4.8}$$

The cross-sectional area is simply an addition of the boom areas, as shown in Equation (4.9). Note that the area of the skins is not taken into account here, since it is assumed that the skins only carry shear and torsional loads. The polar moment of inertia is computed with Equation (4.10), where dA_i is the area enclosed by the triangle formed by connecting the start and end boom of the skin to the center of gravity. The solution for the cross-coupled boom and skin model is also shown.

$$A = 2\,(A_1 + A_2) \tag{4.9}$$

$$J = \frac{4\left(\sum_{i=1}^{4} dA_i\right)^2}{\sum_{i=1}^{4} {}^{l_i}/_{t_i}} = \frac{4w^2h^2}{w\left(\frac{1}{t_2} + \frac{1}{t_4}\right) + h\left(\frac{1}{t_1} + \frac{1}{t_3}\right)} \tag{4.10}$$

After the local stiffness matrices are defined for each beam element they are rotated into the global reference frame. Therefore, the direction cosine matrices λ are constructed. The direction matrices are based on the local coordinate definition in Figure 4.4a and used to map the local coordinates onto the global coordinate system. The global stiffness matrices are thus determined by Equation (4.11). Next, all global stiffness matrices are combined into the complete stiffness matrix of the system. The separate stiffness matrices are placed in the correct place in the global system and overlapping terms are summed. The total system links the external forces P, to the global displacements U, as shown in Equation (4.12).

$$\tilde{k}^{(i)} = (\lambda^{(i)})^T k^{(i)} \lambda^{(i)} \tag{4.11}$$

$$P = KU \tag{4.12}$$

Solving this matrix for the displacements is impossible without applying boundary conditions. Therefore, the boundary conditions specified in the structural model are applied. Rows and corresponding columns of the system are removed in accordance with the directions in which displacement is prohibited. If constraints

$$
\begin{bmatrix} s_1 \\ s_2 \\ s_3 \\ s_4 \\ s_5 \\ s_6 \\ s_7 \\ s_8 \\ s_9 \\ s_{10} \\ s_{11} \\ s_{12} \end{bmatrix}
=
\begin{bmatrix}
\frac{EA}{l} & & & & & & & & & & & \\
0 & \frac{12EI_z}{l^3(1+\phi_y)} & & & & & & & & & & \\
0 & 0 & \frac{12EI_y}{l^3(1+\phi_z)} & & & & & & & & & \\
0 & 0 & 0 & \frac{GJ}{l} & & & & & & & & \\
0 & 0 & \frac{-6EI_y}{l^2(1+\phi_z)} & 0 & \frac{(4+\phi_z)EI_y}{l(1+\phi_z)} & & & & & & & \\
0 & \frac{6EI_z}{l^2(1+\phi_y)} & 0 & 0 & 0 & \frac{(4+\phi_y)EI_z}{l(1+\phi_y)} & & & & & & \\
\frac{-EA}{l} & 0 & 0 & 0 & 0 & 0 & \frac{AE}{l} & & & & & \\
0 & \frac{-12EI_z}{l^3(1+\phi_y)} & 0 & 0 & 0 & \frac{-6EI_z}{l^2(1+\phi_y)} & 0 & \frac{12EI_z}{l^3(1+\phi_y)} & & & & \\
0 & 0 & \frac{-12EI_y}{l^3(1+\phi_z)} & 0 & \frac{6EI_y}{l^2(1+\phi_z)} & 0 & 0 & 0 & \frac{12EI_y}{l^3(1+\phi_z)} & & & \\
0 & 0 & 0 & \frac{-GJ}{l} & 0 & 0 & 0 & 0 & 0 & \frac{GJ}{l} & & \\
0 & 0 & \frac{-6EI_y}{l^2(1+\phi_z)} & 0 & \frac{(2-\phi_z)EI_y}{l(1+\phi_z)} & 0 & 0 & 0 & \frac{6EI_y}{l^2(1+\phi_z)} & 0 & \frac{(4+\phi_z)EI_y}{l(1+\phi_z)} & \\
0 & \frac{6EI_z}{l^2(1+\phi_y)} & 0 & 0 & 0 & \frac{(2-\phi_y)EI_z}{l(1+\phi_y)} & 0 & \frac{-6EI_z}{l^2(1+\phi_y)} & 0 & 0 & 0 & \frac{(4+\phi_y)EI_z}{l(1+\phi_y)}
\end{bmatrix}
\begin{bmatrix} u_1 \\ u_2 \\ u_3 \\ u_4 \\ u_5 \\ u_6 \\ u_7 \\ u_8 \\ u_9 \\ u_{10} \\ u_{11} \\ u_{12} \end{bmatrix}
\tag{4.6}
$$

symmetric

are to be applied under an angle, both the stiffness matrix and external forces are rotated before the constraint is applied. Three different constraints can be supplied as input. For clamped constraints, all displacements and rotations are removed. In the case of symmetry constraints the displacement in the $\widetilde{Y}$-axis is removed, along with the rotations around the $\widetilde{X}$ and $\widetilde{Z}$-axis. The displacement in the direction of support constraints is also fixed. The constraint definition of the PrandtlPlane configuration was shown in Figure 2.1b. It features a clamped front wing root, symmetry at the rear wing root, rigid connections between the surfaces and a support in the direction of the vertical fin. The reduced system can then be solved for the displacements as shown in Equation (4.13), by inverting the reduced stiffness matrix.

Afterwards, the displacements which were constrained are inserted as zeros to determine the total global displacement vector. If rotations were performed to apply the boundary conditions, they are reversed here as well. Finally, the local internal loads s can be calculated using the global displacements, stiffness matrices and direction cosine matrices defined before. This procedure is shown in (4.14).

$$U_r = {K_r}^{-1} P_r \tag{4.13}$$

$$s^{(i)} = k^{(i)} \lambda^{(i)} u^{(i)} \tag{4.14}$$

The local internal loads of the reference configuration are shown in Figure 4.10. The results for the initial and final iteration of the stiffness convergence loop are shown. The discrepencies between the results are significant and show the importance of the iterative procedure in sizing the primary structure.

The internal loads are defined in the local coordinate systems, shown in Figure 4.4a, which are oriented different for each surface. Therefore, distinct jumps are visible in the internal forces and moments. Furthermore, jumps in internal forces are present on the rear wing at the fin attachment. These jumps cause changes in sign for the internal bending moments as well. It is apparent that the secondary bending moments around the local Z axis can not be neglected for the PrandtlPlane configuration. Near the tip of the front wing, the secondary bending moments (Figure 4.10f) even surpass the primary bending moments (Figure 4.10d) in magnitude. Just as Andrews et al. determined, the primary bending moment changes sign along both the front and rear wing.[2] Interestingly, both the primary and secondary bending moments do not reduce to zero at the tip of the front and rear wing. On the rear wing, the primary bending moment at the wing tip is even higher than at the root. The torsional moments, shown in Figure 4.10b, are also most prominent at the tip of the rear wing. Figure 4.10a shows that the beams in the lower wing are in tension, while the beams in the upper wing are compressed. Finally, the secondary shear forces (Figure 4.10c) are non-negligible for this configuration as well. Near the tip of the front wing and root of the rear wing they surpass the primary shear forces (Figure 4.10e) in magnitude. It is interesting to note that the internal load distributions in the front and rear wing do not resemble distributions on conventional wings. Therefore, the current weight estimation methodology in the Initiator, which treats the front and rear wing as conventional wings, is probably not capable of accurately determining the PrandtlPlane wing weight and its distribution. This hypotheses will be tested in Chapter 6.

4.1.7. CROSS-SECTIONAL SIZING

The internal loads in each beam element are used to size the corresponding cross-sections, shown in Figure 4.8. The booms of the cross-section are sized to withstand the axial force F_x and bending moments M_y and M_z. The shear forces F_y and F_z and the torsional moment M_x are carried by the skins.

The booms in the system are cross-coupled to improve the behaviour of the stiffness iteration loop. If all booms are considered separately the problem is indeterminate and an infinite number solutions exist, in which all booms are fully stressed. Therefore, the solution is not guaranteed to reach the same solution in subsequent iterations, which greatly reduces the convergence behaviour of the outer stiffness loop. Furthermore, the equations can be greatly simplified in the cross-coupled case since the center of gravity of the booms is always located in the center of the cross-section, since the skins are assumed to only be effective in withstanding shear flows. Due to the cross-coupling of the booms the design will have an offset from the optimal solution. This effect is investigated in Section 5.3.

Before the booms are sized, the height of the cross-section should be defined. Since this height is a very sensitive parameter to the final wing weight the following procedure is suggested. The height of the section is chosen, such that the first order bending moment M_y carried by the booms is equal to that of the curved upper and lower panel of the airfoil between the two spars. The airfoil and the relevant definitions are shown in Figure 4.11.

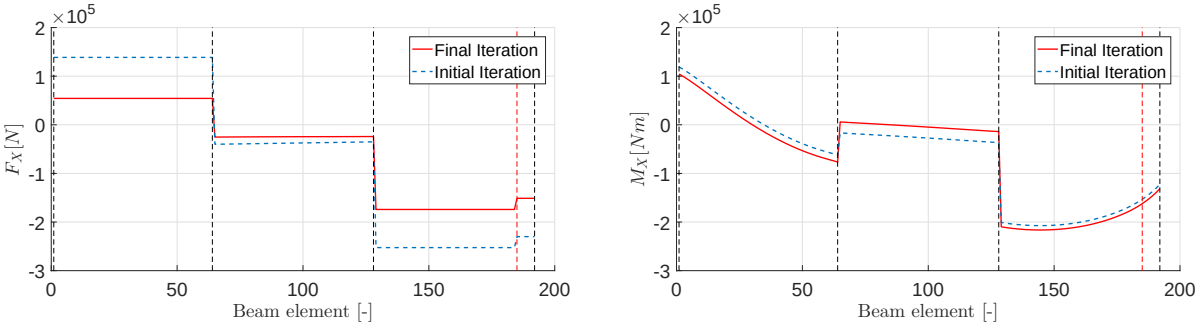

(a) Internal forces in X.

(b) Internal moments around X.

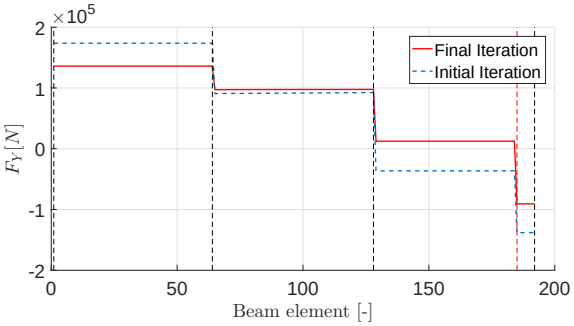

(c) Internal forces in Y.

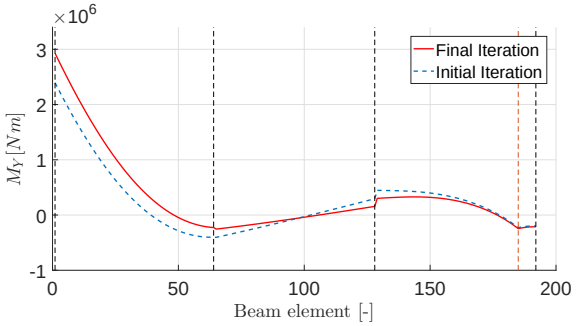

(d) Internal moments around Y.

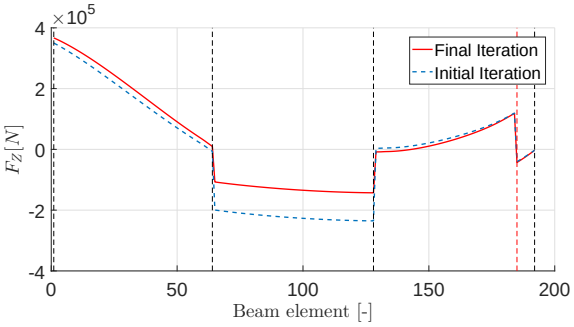

(e) Internal forces in Z.

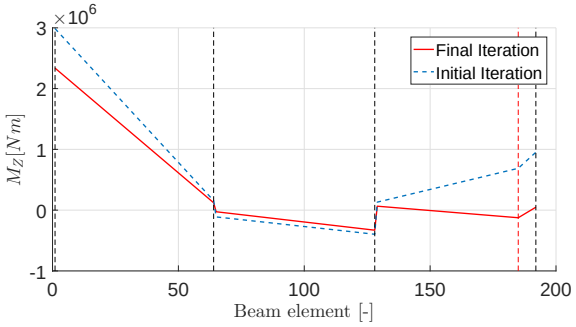

(f) Internal moments around Z.

Figure 4.10: Internal loads in the model of the reference PrandtlPlane.

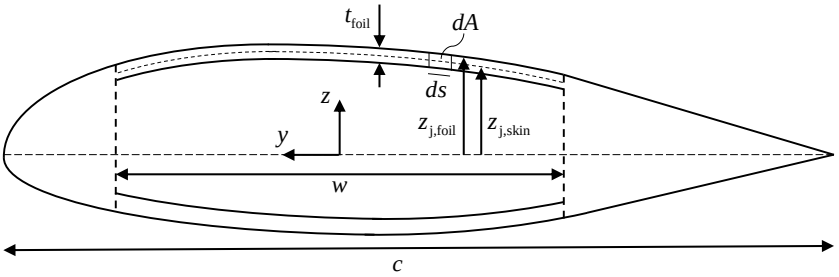

Figure 4.11: Definition of the airfoil and relevant parameters.

The total primary bending moment absorbed by the booms is defined by Equation (4.15), which links the primary bending moment to the height of the cross-section.

$$M_{y,booms} = \sum_{i=1}^{4} |\sigma_i A_i z_i| = \sigma_{alw} h (A_1 + A_2) \tag{4.15}$$

The moment absorbed by the booms is set equal to that in the skin of the airfoil, defined by Equation (4.16), in which both the upper and lower skin are discretized.

$$M_{\text{y,skin}} = \sum_{j=1}^{n} \left| \sigma_j dA_j z_{j,skin} \right| \tag{4.16}$$

The stress in the element furthest away from the neutral line is assumed to be equal to the maximum allowable stress. For the other elements the stress varies linearly with the z-distance from the neutral axis as shown in Equation (4.17). Note that the neutral axis is assumed to be horizontal in this procedure, since the height of the cross-section is mostly determined to withstand primary bending moments. During the actual sizing of the booms, secondary bending moments will be taken into account as well.

$$\sigma_j = \sigma_{alw} \frac{|z_{j,skin}|}{|z_{skin}|_{\max}} \tag{4.17}$$

The thickness of the airfoil skin is assumed to be equal to that of a flat plate positioned between the front and the rear spar with the same cross-sectional area as the booms. The thickness can thus be computed with Equation (4.18).

$$t_{foil} = \frac{A_1 + A_2}{w} \tag{4.18}$$

From the skin thickness, the distance from the elastic axis to the center of the discretized elements can be computed, as well as the area of these elements.

$$|z_{j,skin}| = |z_{j,foil}| - \frac{t_{foil}}{2} \tag{4.19}$$

$$dA_j = t_{foil} ds_j \tag{4.20}$$

Finally, all equations can be simplified and rearranged into Equation (4.21), which links the height of the cross-section to the shape of the airfoil and the boom areas. Due to the inter-dependency between the boom areas and cross-sectional height an iteration loop should be implemented.

$$h = \frac{\sum_{j=1}^{n} ds_j \left(|z_{j,foil}| - \frac{A_1 + A_2}{w} \right)^2}{w \left(|z_{foil}|_{\max} - \frac{A_1 + A_2}{w} \right)} \tag{4.21}$$

However, the additional loop increases the computational time of the overall tool considerably, since it is executed for each beam element and during each overall stiffness iteration. Therefore, the assumption is made that the height of the airfoil shape only depends on the shape of the airfoil itself and that the material offset due to the skin thickness is neglected. The determination of the cross-sectional height then reduces to Equation (4.22). The effect of this assumption will be investigated in Section 5.3.

$$h = \frac{\sum_{j=1}^{n} ds_j z_{j,foil}^2}{w |z_{foil}|_{\max}} \tag{4.22}$$

The width of the cross-section is defined as the distance between the front and rear spar at the particular cross-section. As shown in Figure 4.4a, the orientation of the beam element is taken into account, such that the width in local y-direction is found. With the dimensions of the cross-section and the internal loads known the boom areas can be determined. The normal stresses in a boom can be computed with Equation (4.23).

$$\sigma_x(y,z) = \frac{M_z(I_{yz} z - I_{yy} y)}{I_{zz} I_{yy} - I_{yz}^2} + \frac{M_y(I_{zz} z - I_{yz} y)}{I_{zz} I_{yy} - I_{yz}^2} + \frac{F_x}{2(A_1 + A_2)} \tag{4.23}$$

In which the moments of inertia are defined by Equations (4.24) until (4.26).

$$I_{yy} = \sum_{i=1}^{4} A_i (z_i - \bar{z})^2 = 2\left(\frac{h}{2}\right)^2 (A_1 + A_2) \tag{4.24}$$

$$I_{zz} = \sum_{i=1}^{4} A_i \left(y_i - \bar{y}\right)^2 = 2\left(\frac{w}{2}\right)^2 (A_1 + A_2) \tag{4.25}$$

$$I_{yz} = \sum_{i=1}^{4} A_i \left(y_i - \bar{y}\right)(z_i - \bar{z}) = \frac{hw}{2} (A_1 - A_2) \tag{4.26}$$

The contributions of the two bending moments are equal in magnitude, but opposite in sign for two opposing booms. In one of those booms the normal force F_x will act a relief, while it increases the normal stress in the other boom. Due to the cross-coupled lay-out it will be treated as an increase in normal stress for all booms. Furthermore, the normal stress in all booms should be lower or equal to the allowable normal stress of the material. The allowable normal and shear stress are defined by Equation (4.27).

$$\sigma_{alw} = \text{fos} \cdot \sigma_{\text{yield}} \qquad \tau_{alw} = \text{fos} \cdot \tau_{\text{yield}} \tag{4.27}$$

The system that should thus be solved to determine the boom areas is shown in equation (4.28).

$$\sigma_{alw} = \left| \frac{M_z(I_{yz} z_i - I_{yy} y_i)}{I_{zz} I_{yy} - I_{yz}^2} + \frac{M_y(I_{zz} z_i - I_{yz} y_i)}{I_{zz} I_{yy} - I_{yz}^2} \right| + \left| \frac{F_x}{2(A_1 + A_2)} \right| \qquad \text{for} \quad i = 1:4 \tag{4.28}$$

Due to the cross-coupling, one solution exists which can be reduced to Equation (4.29). In which C_1 and C_2 are defined by Equation (4.30). The booms are thus sized such that they can carry both the primary and secondary bending moments, as well as the normal force.

$$A_1 = \frac{\frac{C_1}{4\frac{w}{2}\frac{h}{2}} + \frac{|F_x|}{2\left(1+\frac{C_2}{C_1}\right)}}{\sigma_{alw}} \qquad A_2 = \frac{\frac{C_2}{4\frac{w}{2}\frac{h}{2}} + \frac{|F_x|}{2\left(1+\frac{C_1}{C_2}\right)}}{\sigma_{alw}} \tag{4.29}$$

$$C_1 = \left| M_y \frac{w}{2} + M_z \frac{h}{2} \right| \qquad C_2 = \left| M_y \frac{w}{2} - M_z \frac{h}{2} \right| \tag{4.30}$$

After the areas of the booms have been determined the skin thicknesses are sized to withstand the shear flows. The shear flow in the skins is composed of three contributions: the open section shear flow, the closed section shear flow and a contribution due to torsion. For the open section shear flow, the skin is assumed to be cut in the front spar, such that the open section shear flow is zero there. The open shear flow in the other three skins is then calculated using Equation (4.31).[28]

$$q_i = q_{i-1} - \left(\frac{F_z I_{zz} - F_y I_{yz}}{I_{zz} I_{yy} - I_{yz}^2} \right) A_i (z_i - \bar{z}) - \left(\frac{F_y I_{yy} - F_z I_{yz}}{I_{zz} I_{yy} - I_{yz}^2} \right) A_i (y_i - \bar{y}) \tag{4.31}$$

The closed-section shear flow can be estimated using Equation (4.32).[2] With dA_i being the area of the triangle connecting booms i and $i+1$ to the center of gravity of the cross-section.

$$q_o = -\frac{\sum_{i=1}^{4} 2 q_i dA_i}{2\sum_{i=1}^{4} dA_i} = -\frac{\sum_{i=1}^{4} q_i}{4} \tag{4.32}$$

Finally, the shear flow caused by torsion is added and the required thickness of each skin can be calculated to withstand the allowable shear stress τ_{alw}, as shown in Equation (4.33).[2] The maximum allowable shear stress is defined by Equation (4.27). In this procedure, the shear center is assumed to coincide with the center of gravity. In reality, the location of the shear center will depend on the thickness of the skins and an additional iteration loop would be necessary. This would increase the required computation time and reduce

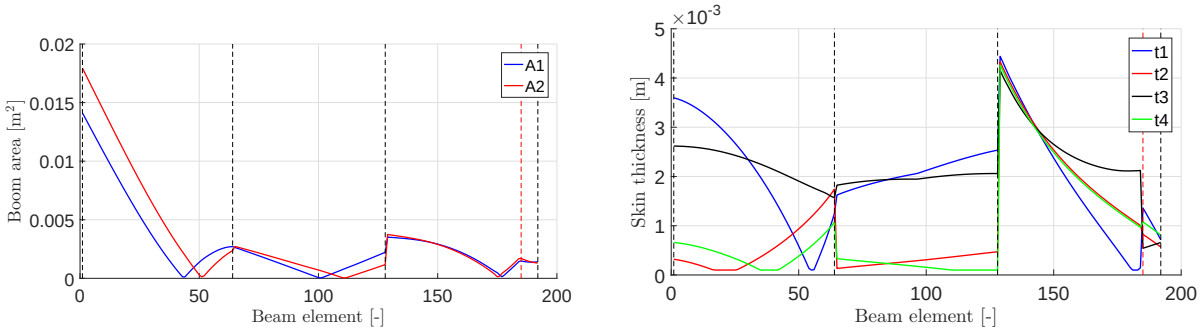

(a) Boom area distribution.

(b) Skin thickness distribution.

Figure 4.12: Local cross-sectional sizing results of the reference case.

the convergence behaviour of the outer stiffness lopp. The effect of this assumption on the total wing weight was found to be minor by Bindolino et al. and will be investigated in Section 5.3.[18]

$$t_i = \frac{1}{\tau_{alw}}\left(q_i + q_0 + \frac{M_x}{2\sum_{i=1}^{4} dA_i}\right) = \frac{1}{\tau_{alw}}\left(q_i + q_0 + \frac{M_x}{2wh}\right) \tag{4.33}$$

To aid in the convergence of the outer loop and for manufacturing purposes, a minimum skin thickness of $1e^{-4}m$ has been defined. If the skin thickness computed by Equation (4.33) is lower than the minimum, the minimum value is used instead.

The skin thicknesses and boom areas computed for the reference section are shown in Figure 4.12. Furthermore, the cross-sectional height throughout the design is shown in Figure 4.13. The largest boom areas are encountered at the root of the front wing and tip of the rear wing, which is in line with the large internal loads at these locations seen in Figure 4.10. Along the rear wing, where the secondary bending moments are smaller, the area of all four booms is approximately equal. For sections with a horizontal neutral axis, the cross-sectional design thus mimics a symmetric, conventional wingbox. The large skin thicknesses at the tip of the rear wing are caused by the high torsional moment, and the smaller sized wingbox at that location. The height distribution throughout the design is dependent on the chord length, airfoil thickness and sweep angle. Due to the taper of both wings, the cross-sectional height decreases from root to tip. The wing geometry features equal, but opposite, leading edge sweep angles on the front and rear wing. However, due to the applied taper ratio, a discrepancy exists between the half chord sweep angles of the wings. Therefore, a slight offset in the cross-sectional height of the front and rear wing is seen.

4.1.8. PRIMARY WEIGHT ESTIMATION LOOP

After all beam element have been sized to withstand the internal loads, the primary weight of the structure can be computed. The weight is determined by multiplying the cross-sectional area of each beam by its length and material density, and summing over all beams as shown in Equation (4.34).

$$W_{prim} = \rho_{mat} \sum_{i=1}^{n} l_i \left(2\left(A_{1_i} + A_{2_i}\right) + h\left(t_{1_i} + t_{3_i}\right) + w\left(t_{2_i} + t_{4_i}\right)\right) \tag{4.34}$$

As shown in Figure 4.1 the results of the primary weight estimation are fed back in a new iteration of the stiffness loop. The weight of each beam elements is used to update the inertial relief loads. Furthermore, the sizing results are fed into the next determination of the internal loads, since the stiffness of all beam elements has changed. This loop is repeated until the convergence specified in Equation (4.1) is reached and the final primary weight is determined. For closed-wing configurations the complete tool converges in 20-30 iterations, which takes approximately 20-30 seconds.

The convergence behaviour of the reference configuration is shown in Figure 4.14. The first iteration is sized based on a default cross-sectional design. The weight then drops sharply before it starts rising slowly again. After 22 iterations the system has converged, according to the criteria in Equation (4.1). The difference in internal loads between the first and and final iteration are compared in Figure 4.10. In Figure 4.15 the distribution of the primary weight throughout the wing is shown. The majority of the weight is located in root of the front wing. Interestingly, the tip of the rear wing is heavier than its root. This effect can be explained

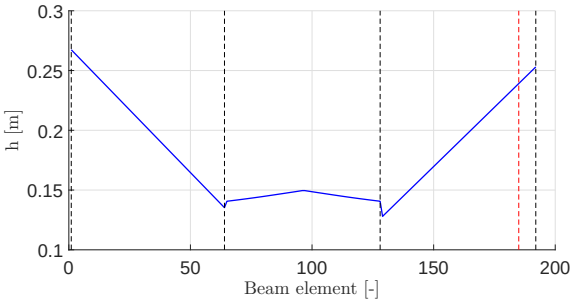

Figure 4.13: Cross-sectional height distribution.

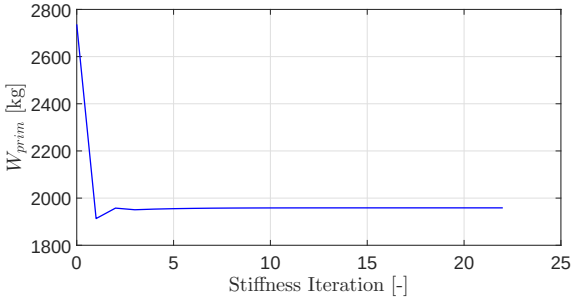

Figure 4.14: Outer loop convergence behaviour.

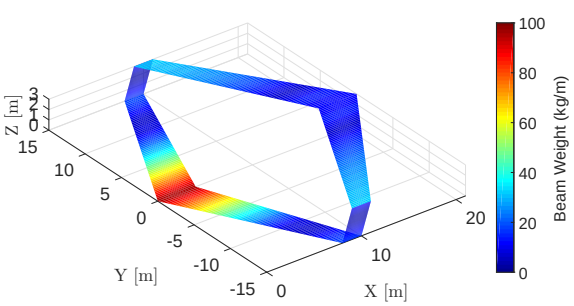

(a) Visual representations of the primary weight distribution .

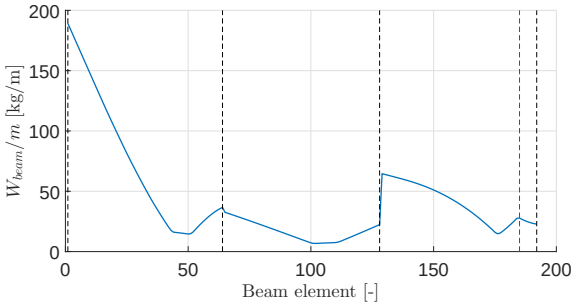

(b) Beam weight per meter throughout the structure.

Figure 4.15: Results of the primary weight estimation loop for the reference case.

by looking at the internal loads in Figure 4.10 and the cross-sectional design in Figure 4.12. The primary bending and torsional moments at the rear wing tip are higher than at its root. Combined with the fact that the cross-sectional area at the tip is smaller, thicker booms and skins are needed to withstand the internal loads.

4.1.9. SECONDARY WEIGHT ESTIMATION

Two different methods are proposed to provide an approximation of the secondary wing weight. First, if little input is available about control surfaces and high lift devices the user can opt to use the same relationship as the EMWET tool. This relationship is based on a regression analysis between the primary weight calculated by EMWET and the total wing weight of several conventional wings. The relationship is shown in Equation (4.35).[23]

$$W_{\text{sec}} = 10.147 W_{prim}^{0.8162} - W_{prim} \tag{4.35}$$

A few notable drawbacks of applying this equation to unconventional configurations exist. First, the regression data only contains conventional aircraft. Secondly, the methodology proposed by Elham et al. to determine the primary wing weight is different from the methodology proposed in this chapter. A detailed comparison will be provided in Section 5.2. Finally, the methodology is not sensitive to design choices on control surfaces and high lift devices. Therefore, a more detailed methodology, which can be selected by the user has been implemented as well.

In this case the secondary wing weight is determined in accordance with Torenbeek.[29] It should be noted that this method is based on empirical relations for conventional aircraft. However, all components weights are determined separately and are based on non-configuration specific inputs and relationships. The weight of the ribs, control surfaces, high lift devices, fixed leading and trailing edges and a penalty due to cut-outs and joints are considered in the methodology. The weight of the wing ribs is calculated with Equation (4.36).

$$W_{rib} = k_r \rho g S \left(t_{ref} + \frac{t_r + t_t}{2} \right) \tag{4.36}$$

With $k_r = 0.5x10^{-3}$ and $t_{ref} = 1.0m$.

Equation (4.37) determines the additional wing weight due to fixed leading edges and Equation (4.38) for fixed trailing edges. The weight of leading-edge devices and trailing edge devices is computed with Equations (4.39) and (4.40) respectively.

$$W_{fle} = 75 S_{fle} k_{fle} \left(1 + \sqrt{W_{to}/10^6}\right) \tag{4.37}$$

In which, k_{fle} is equal to 1.0 if no leading edge devices are present and 1.4 if they are.

$$W_{fte} = 60 S_{fte} \left(1 + 1.6\sqrt{W_{to}/10^6}\right) + \Delta \tag{4.38}$$

With Δ being 0, 45 or 105 for single slotted, double slotted or triple slotted flaps respectively.

$$W_{slat} = 160 S_{slat} \left(1 + 0.7\sqrt{W_{to}/10^6}\right) \tag{4.39}$$

$$W_{tef} = 100 S_{tef} k_{tef} \left(1 + \sqrt{W_{to}/10^6}\right) \tag{4.40}$$

In which k_{tef} is a variable, which ranges from 1.0 to 2.9 based on the type of trailing edge high lift devices employed. The extra rib weight due to inclusion of the flap support systems can be assumed to be 5% of the total flap weight.

The weight estimation of the ailerons is accounted for by Torenbeek with Equation (4.41). For the support system of the ailerons an additional weight increment of 20% should be added. The weight of spoilers and lift-dumping systems can generally be calculated with Equation (4.42).

$$W_a = 125 S_a \left(1 + 0.5\left(W_{to}/10^6\right)^{1/4}\right) \tag{4.41}$$

$$W_{sp} = 110 S_{sp} \tag{4.42}$$

The weight penalty due to cut-outs and joints in the panels is determined with Equation (4.43).

$$\Delta W_{NO} = \rho g S (1 + 2(t/c)_{mean}) \delta_{NO} \tag{4.43}$$

In which the non-optimum extra thickness δ_{NO} is 10^{-3} for typical built-up structures and half that for integrally machined skin-stringer panels.

4.1.10. POST-PROCESSING

The final module in the closed-wing weight estimator deals with the post-processing. First, the total wing weight is determined by summing the primary and secondary weights as shown in Equation (4.44).

$$W_{\text{wing}} = W_{\text{prim}} + W_{\text{sec}} \tag{4.44}$$

Next, all results are visualized. The aerodynamic coefficients, external loads, internal loads, cross-sectional design, convergence behaviour and primary weight distribution results are plotted. The resulting figures were shown throughout this section for the reference case.

4.2. CONCEPTUAL DESIGN METHODOLOGY

Since the main research question aims to determine the influence of the newly proposed wing weight estimation methodology on the overall PrandtlPlane design, the closed-wing weight estimation tool is implemented in the Initiator framework. An overview of the conceptual closed-wing design methodology in the Initiator is given in Section 4.2.1. Before the new wing weight estimation module was implemented, all existing modules were migrated to the newest version. The implications of these changes are discussed in Section 4.2.5. It should be noted that the main focus of this research is on the closed-wing weight estimation. The methodology described in this section, is thus mainly used as-is. The Initiator methodology was migrated and updated, but no new modules were added.

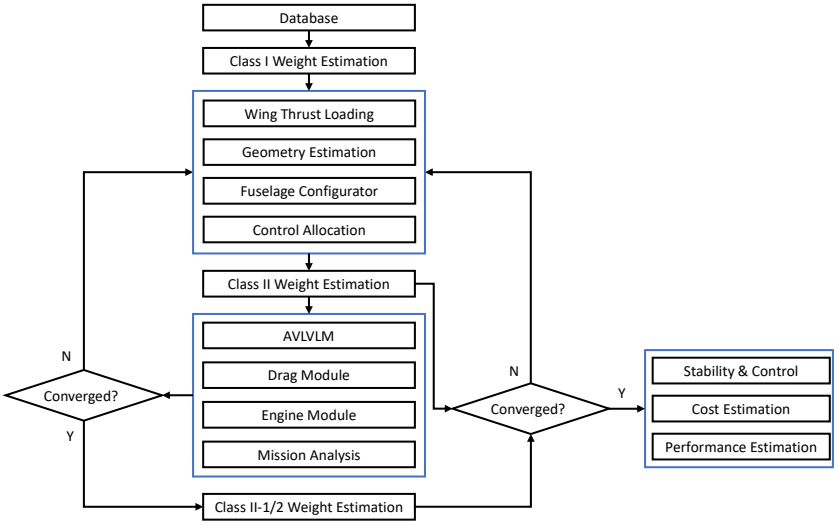

Figure 4.16: Conceptual design workflow in the Initiator.

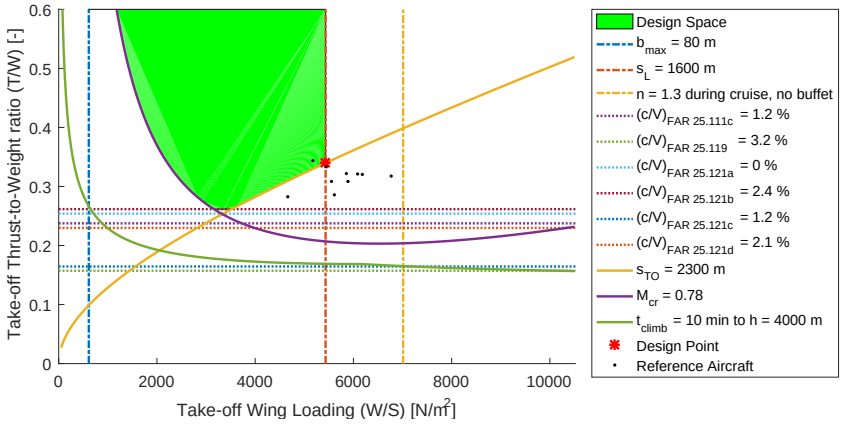

Figure 4.17: Wing loading diagram created in the Initiator.

4.2.1. CONCEPTUAL DESIGN WORKFLOW IN THE INITIATOR

The goal of the Initiator is to provide an initial design from a set of mission requirements. The conceptual design flow of PrandtlPlanes in the Initiator framework is visualized in Figure 4.16. A Class I weight estimation is performed using data from a reference database. With this initial weight estimation, the wing thrust loading diagrams are created to determine the required reference area of the wing. The initial aircraft geometry is then generated, which is used as input for a Class II weight estimation. Several analysis modules are ran after this weight estimation and the wing thrust loading constraints are updated. This procedure is repeated until converge occurs. The Class II-1/2 weight estimations for the wings and fuselage are then performed to improve the accuracy of the results. The results are fed back into the Class II weight estimation until the total design has converged. Finally, a check on stability and controllability is included.

4.2.2. GEOMETRY ESTIMATION MODULES

Before the geometry of the aircraft is defined the wing loading diagram is constructed to determine the required wing reference area of the aircraft. This procedure is shown in Figure 4.17. The design space is limited by a range of requirements. The design point is chosen, such that the highest possible wing loading is achieved, for the lowest possible thrust to weight ratio. The required wing area thus changes when the estimated weight of the aircraft is updated.

The required wing planform area is distributed between the front and the rear wing of the configuration with a distribution ratio defined by Equation (4.45). This ratio is an input to the design workflow. The front and rear wing areas are then deduced with Equation (4.46).

$$\lambda_{area} = S_{front}/S_{rear} \tag{4.45}$$

$$S_{front} = \frac{S_{tot}}{1 - \frac{1}{\lambda_{area}}} \qquad S_{rear} = \frac{S_{tot}}{1 + \lambda_{area}} \tag{4.46}$$

Other inputs that can be supplied to define the geometry of the PrandtlPlane wings and fins include: sweep angles, dihedral angles, aspect ratios, taper ratios, twist angles, longitudinal front wing position and the type of rear wing connection. The front and rear wing geometries are generated and the lateral wing is used to connect them. The size and orientation of the lateral wing can thus be altered by changing the position, size and orientations of the front and rear wing. Furthermore, the cabin and fuselage geometries are defined such that the number of passengers and cargo defined in the mission requirements fit.

4.2.3. WEIGHT ESTIMATION MODULES

Three different weight estimation methodologies have been implemented in the Initiator. The Class I weight estimation is based on reference data from a database. The top level requirements, which are defined as inputs to the workflow are used for this analysis. The results of this preliminary weight estimation are used to create an initial geometry definition, as described in Section 4.2.2.

During the Class II weight estimation empirical relations by Raymer are used to determine the weight of the aircraft components separately.[30] In this stage, the center of gravity location of the aircraft is determined, which will be used in the aerodynamic analysis and the stability and control module. Since some component weights depend on the maximum take-off weight of the configuration, the Class II weight estimation is iterated until convergence occurs.

Finally, a Class II-1/2 weight estimation module is included in the Initiator. This module determines the weight of the fuselage and wings with semi-analytical methods. The new closed-wing weight estimation methodology is incorporated here to replace the methodology by Zohlandt, as described in Section 2.3. The results of the Class II-1/2 weight estimations are used to replace the fuselage and wing weight in subsequent iterations of the Class II-loop as shown in Figure 4.16.

4.2.4. ANALYSIS MODULES

Three analysis modules shown in Figure 4.16 will be described in more depth in this section. The aerodynamic and mission analyses are performed in the design convergence loop, while the stability and controllability is investigated after the design has converged.

AERODYNAMIC ANALYSIS

The aerodynamic analysis of the configuration is performed in AVL. The Athena vortex lattice solver, developed by Drela, uses the geometry of all lifting surfaces and loading conditions for a Trefftz-Plane analysis.[31] The induced drag, aerodynamic coefficients and derivatives are used in subsequent modules. Trimming of the configuration is performed by coupling the control surfaces in the input file with a gain, which is supplied as input. The configuration is then trimmed such that the pitching moment around the center of gravity is zero. AVL is used to determine both the induced and the trim drag of the aircraft. The parasitic and wave drag are accounted for with empirical relations developed by Roskam.[32]

MISSION ANALYSIS

The aerodynamic results are used in the mission analysis module, together with the results of the weight estimation. The mission, described as top-level requirement, is simulated to determine the total required fuel weight. The mission includes a harmonic range and a diversion, in which a loiter phase is included. An example of a mission analysis for a converged design is shown in Figure 4.18. The results show that the aircraft mass decreases to the maximum zero fuel mass at then end of the complete mission. This indicates that the available fuel is exactly enough to perform the mission.

If the analysis indicates that the fuel weight is insufficient, it is increased for the next design iteration. Due to the small chord lengths of PrandtlPlane configurations, the available fuel volume in the wings is often insufficient to fit all required fuel. In those cases, an additional fuel tank in the fuselage is automatically generated.

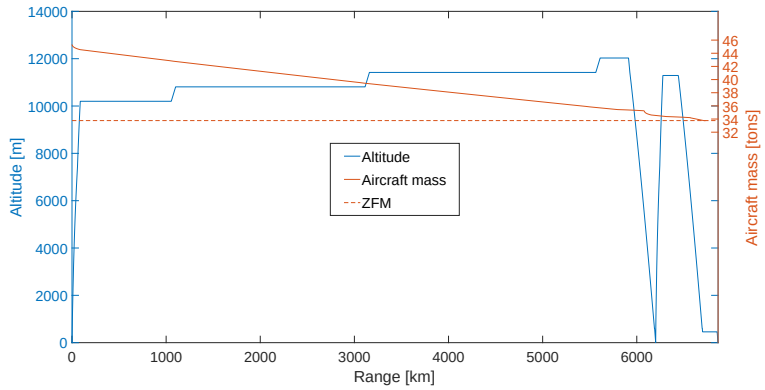

Figure 4.18: Mission profile created by the Initiator.

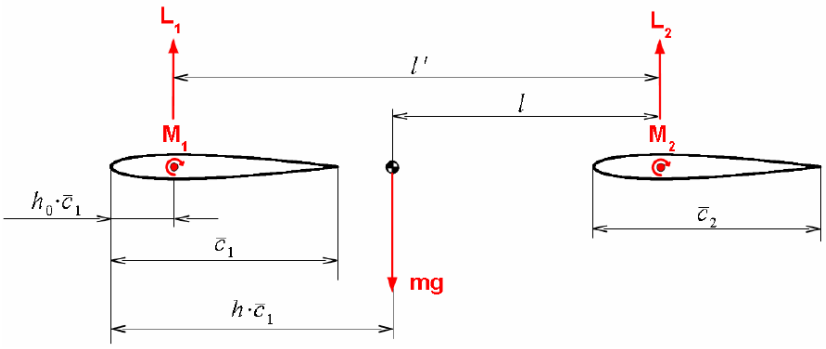

Figure 4.19: Definition of control limit h.[4]

STABILITY & CONTROLLABILITY

The requirements to attain a longitudinally stable and controllable aircraft are similar to those in conventional configurations. The entire range of centers of gravity should be in front of the neutral point and behind the control limit. A minimum stability margin, defined by Equation (4.47), of 0.05 should be achieved.

$$SM = \frac{\left(X_{np} - X_{CG,aft}\right)(S_1 + S_2)}{\bar{c}_1 S_1 + \bar{c}_2 S_2} \tag{4.47}$$

The control limit h is defined in figure 4.19. For controllability the maximum forward center of gravity position should be located behind this control limit, which is calculated with Equation (4.48).[4]

$$h > h_0 + \frac{C_{L,2}}{C_L}\frac{\bar{V}'}{\bar{c}_1'} + \frac{C_{M,1}}{C_L}s_1 + \frac{C_{M,2}}{C_L}s_2\frac{\bar{c}_2}{\bar{c}_1} \tag{4.48}$$

In which the modified volume coefficient of the aft wing is defined by Equations (4.49). The length of the total mean aerodynamic chord and the relative reference areas are defined by Equations (4.50) and (4.51) respectively.

$$\bar{V}' = \frac{l'}{\bar{c}}s_2 \tag{4.49}$$

In which l' is the longitudinal distance between the aerodynamic centers of the front and rear wing.

$$\bar{c} = \bar{c}_1 s_1 + \bar{c}_2 s_2 \tag{4.50}$$

$$s_i = \frac{S_i}{S_1 + S_2}; i = 1:2. \tag{4.51}$$

To increase the controllability of closed-wing configurations the lift coefficient on the rear wing should thus be reduced, while increasing it on the front wing. Another way of improving the controllability of the

configuration is to increase the horizontal distance between the two wings, such that l' increases. The described methodology is implemented as a final check in the Initiator design workflow. A visualization of a stable, controllable PrandtlPlane configuration is shown in Figure 4.20, which indicates that the range of centers of of gravity falls in between the stability and controllability limits.

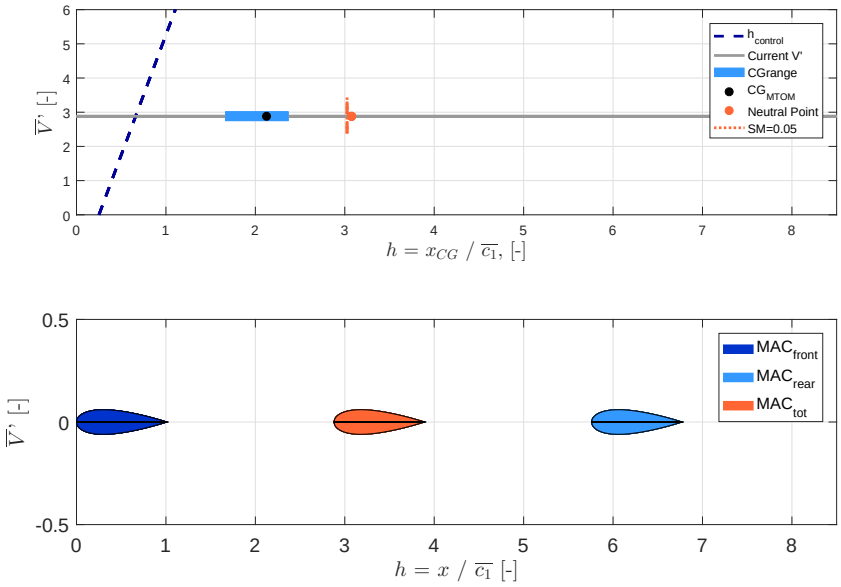

Figure 4.20: Stability and controllability diagram created by the Initiator.

4.2.5. VERSION MIGRATION OF PRANDTLPLANE DESIGN IN THE INITIATOR

All PrandtlPlane design modules in the Initiator were migrated from version 2.6 to 2.9. Several new modules were implemented since then and a range of bugs has been fixed. Therefore, a comparison is provided between a PrandtlPlane design in version 2.6 of the Initiator and version 2.9. Both these modules make use of the conventional EMWET tool for the closed-wing weight estimation.

The results from version 2.6 are taken from Zohlandt's report.[11] The inputs files were adapted to the format for version 2.9 and used to perform a full design convergence. The aircraft is designed to transfer 144 passengers with a total payload mass of 19500 kg over 4000 km. The lay-out of the two designs is compared in Figure 4.21.

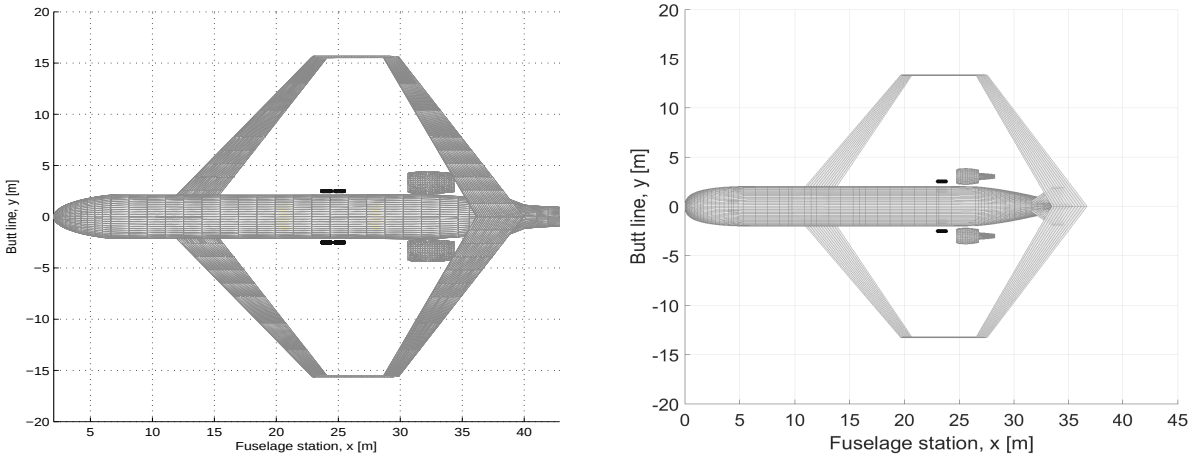

(a) PrP-144 design in Version 2.6.

(b) PrP-144 design in Version 2.9.

Figure 4.21: Comparison of the PrP-144 design between V2.6 and V2.9.

The most obvious discrepancy between the two configurations is the length of the fuselage. The new

fuselage configurator module estimates the fuselage to be 35.5 m long, compared to the 40.7 m in the older Initiator version. Therefore, the sweep angle of the fins was altered, such that the same wing lay-out could be maintained. Furthermore, the wingspan of the new design is smaller, due to a decrease in maximum take-off weight.

The design weights, as well as the breakdown into component weights is compared in Tables 4.1 and 4.2.

Table 4.1: PrandtlPlane weight comparison V2.6 and V2.9.

	Version 2.6	**Version 2.9**	**Difference**
Maximum take-off mass	77510 kg	61785 kg	-20.2%
Operational empty mass	43620 kg	31696 kg	-27.3%
Payload mass	19500 kg	19500 kg	0%
Total fuel mass	14390 kg	10589 kg	-26.4%

Table 4.2: Component weight comparison V2.6 and V2.9.

	Version 2.6	**Version 2.9**	**Difference**
Fuselage	8906 kg	8376 kg	-6.0%
Engines	5932 kg	4002 kg	-32.5%
Front wing	5979 kg	5736 kg	-4.1%
Lateral wing	773 kg	686 kg	-11.3%
Rear wing	3550 kg	2720 kg	-23.4%
Main landing gear	2412 kg	1992 kg	-17.4%
Nose landing gear	356 kg	315 kg	-11.5%
Vertical tails	747 kg	698 kg	-6.6%
Furnising	4573 kg	1120 kg	-75.5%
Systems	6539 kg	3161 kg	-51.7%

The differences between the two version are large. The required fuel weight has decreased by 26.4%, which is mainly caused by a large decrease in the operational empty weight. The reductions there are partly caused by the different geometries and the snowball effect, but updated sizing and weight estimation modules in the Initiator had the largest influence.

Five major differences in the design methodology can be defined. First, the furnishing weight was calculated incorrectly in version 2.6 of the Initiator, explaining the large discrepancy between the two versions. Secondly, the structural wing safety factor of 1.5 was used twice in version 2.6; once to calculate the external loads and once to define the maximum allowable stresses. This led to an overestimation of the wing weight. Thirdly, engine and APU weights were based on regression data, for much larger aircraft than the one considered in the current analysis. Fourthly, the hydraulics weight estimation incorrectly implemented Raymers methodology, leading to an overestimation of more than 1500 kg. Finally, a new landing gear sizing and positioning module was implemented, which reduced the landing gear weight.

It should be noted that the large discrepancies do not necessarily invalidate the results of the design studies by Zohlandt.[11] All problems mentioned above, were present for both conventional and unconventional configurations. Even though the absolute PrandtlPlane design and performance might have been inaccurate, the relative comparison to conventional configurations suffered less.

5

VERIFICATION & VALIDATION

The closed-wing weight estimation methodology described in Chapter 4 is verified and validated in this chapter. In Section 5.1, a verification of the internal loads and stresses with a finite element solution is performed. The methodology is compared to the conventional semi-analytical wing weight estimator EMWET in Section 5.2. Finally, in Section 5.3 the influence of the major assumptions and simplifications is investigated to determine if they seem reasonable.

5.1. INTERNAL LOADS VERIFICATION

A verification procedure has been carried out to determine if the internal loads computed by the weight estimation method are correct. Therefore, a complete PrandtlPlane wing weight estimation has been performed. Three types of input were used to construct a structural model in MSC Patran. First, the geometry of the configuration, shown in Figure C.3 in Appendix C, was recreated. Three external constraints are applied to the model: a clamp at the front wing root, symmetry at the rear wing root and a support along the <0.6, 0.2, 1> vector at a tenth of the rear winspan.

Secondly, the external loads found by the load application module are used to create the same loads on the Patran model. These external loads are shown in Figure C.2 in Appendix C. Finally, the sizing results of each beam element are used to determine the distribution of the cross-sectional areas and moments of inertia in the Patran model. The distribution of the cross-sectional properties is shown in Figure C.1. The corresponding cross-sectional sizing results and distribution of the weight along the wingspan are included and visualized in Figure C.5 and C.4 respectively.

The structural model created by Patran is evaluated in Nastran to determine the internal loads in each beam element. These results are then compared to the internal loads found in the weight estimation tool in Figure 5.1.

The determination of the internal loads in the tool is in line with the results found by Nastran. The distribution of the internal loads is similar to the reference case discussed in Section 4.1.6 and conclusions drawn there, still hold.

Since the width and height of each cross-section are known, the axial stresses in the four booms can be determined with Equation (5.1). The resulting axial stresses are shown in Figure 5.2 to determine the effect small offsets in internal loads between the tool and the Nastran model might have. The same procedure is repeated for the shear stresses in the four skins. These results are compiled in Figure 5.3.

$$|\sigma_i| = \left| (z_i - \bar{z}) \frac{M_y I_{zz} + M_z I_{yz}}{I_{yy} I_{zz} - I_{yz}^2} - (y_i - \bar{y}) \frac{M_z I_{yy} + M_y I_{yz}}{I_{yy} I_{zz} - I_{yz}^2} + \frac{F_x}{2\,(A_1 + A_2)} \right| \tag{5.1}$$

The internal loads determined by Nastran seem to correspond closely with the values found in the tool. Therefore, the axial stresses in all booms are verified as well. Not all of the booms are fully stressed throughout the design. This is the drawback of selecting a symmetric cross-section. This effect will be investigated and described more in-depth in Section 5.3.1.

The shear stress distribution for the Nastran model and wing weight distribution correspond closely. It should be noted however, that the offset of the shear center from the geometric center of gravity has not been included in this analysis. This effect will be evaluated in Section 5.3. The only elements at which the shear

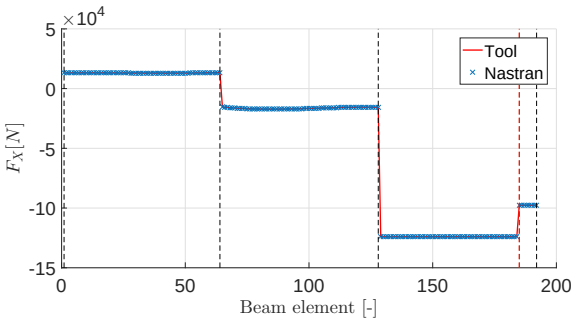

(a) Internal forces in X.

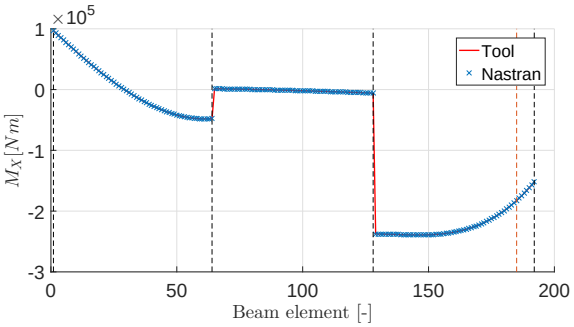

(b) Internal moments around X.

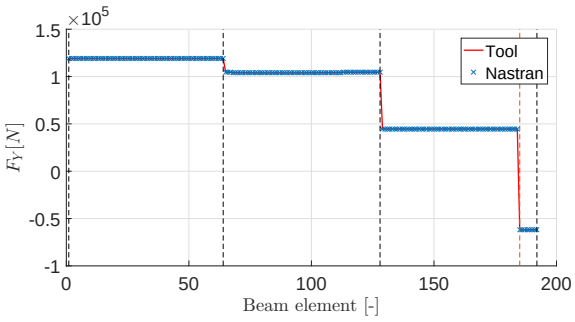

(c) Internal forces in Y.

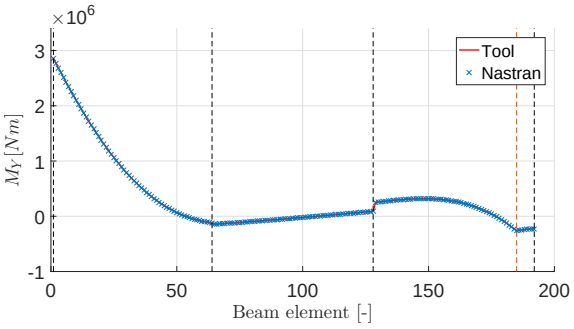

(d) Internal moments around Y.

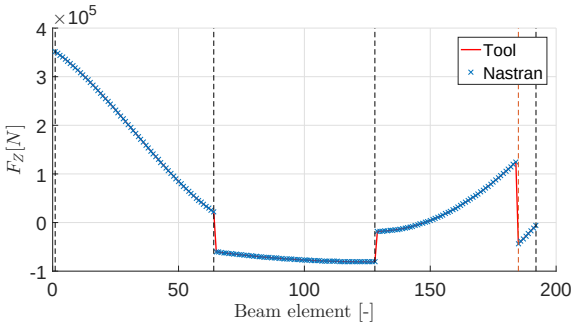

(e) Internal forces in Z.

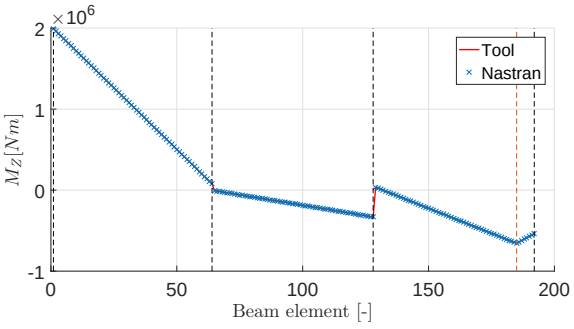

(f) Internal moments around Z.

Figure 5.1: Internal load comparison between tool and Nastran.

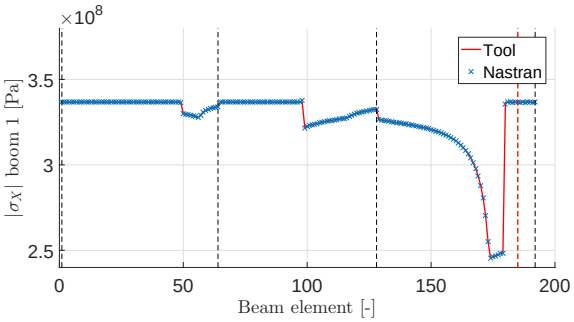

(a) Axial stress in boom 1.

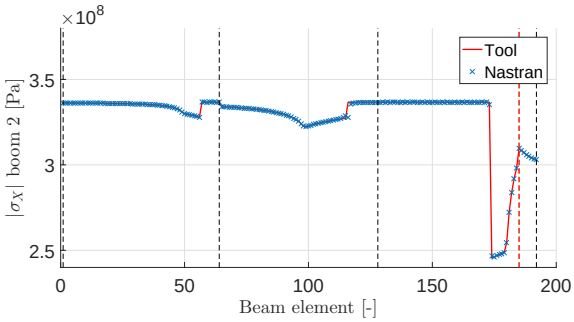

(b) Axial stress in boom 2.

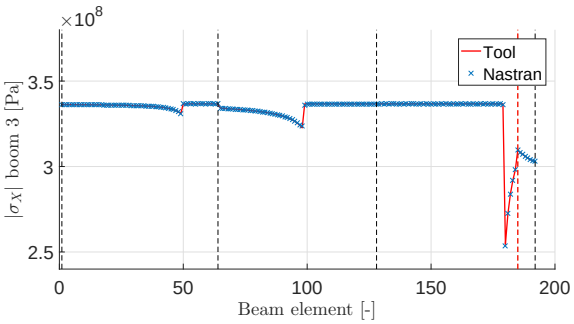

(c) Axial stress in boom 3.

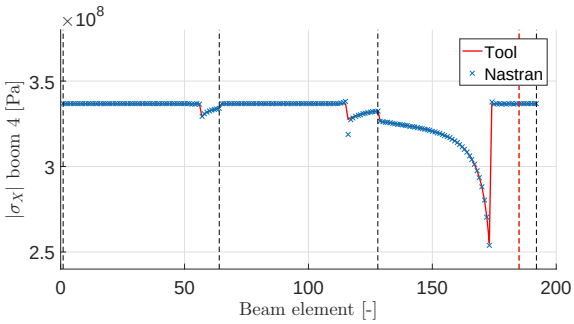

(d) Axial stress in boom 4.

Figure 5.2: Comparison axial stresses tool and Nastran.

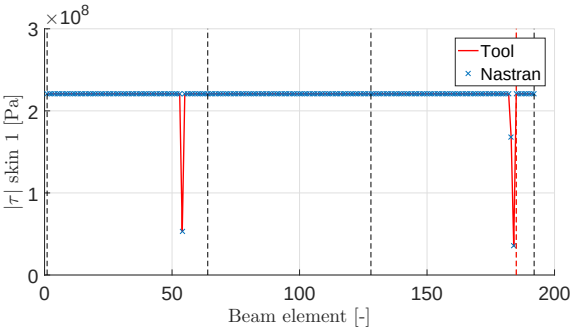

(a) Shear stress in skin 1.

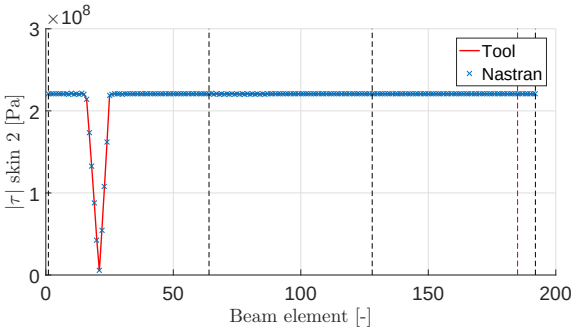

(b) Shear stress in skin 2.

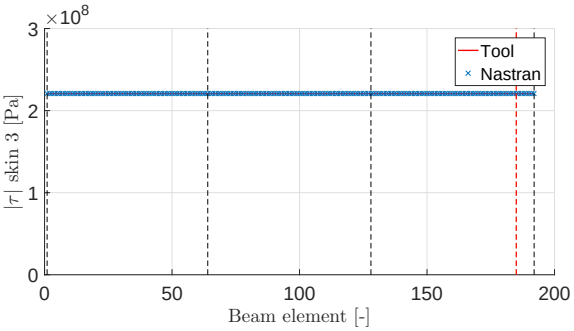

(c) Shear stress in skin 3.

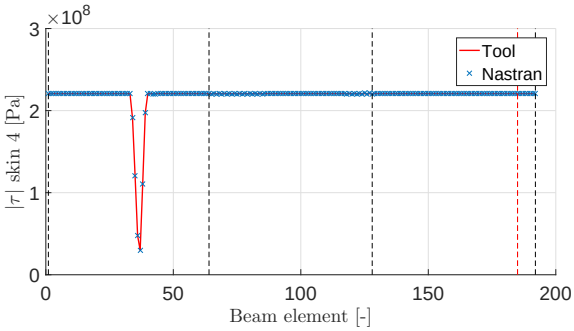

(d) Shear stress in skin 4.

Figure 5.3: Comparison shear stresses tool and Nastran.

stress in the skin drops below the maximum allowable shear stress is when the skin is thickened to the gauge thickness for manufacturing purposes. This minimum gauge thickness has a minor effect on the final wing weight, but improves the convergence behaviour of the stiffness loop greatly, as described in Section 4.1.7.

In general, the internal loads and stresses determined by the closed-wing weight estimator correspond closely to the results found using the finite element software Nastran. Therefore, the methodology described in Chapter 4 is deemed verified.

5.2. EMWET WEIGHT ESTIMATION COMPARISON

The verification in Section 5.1 only shows the ability of the tool to correctly determine the internal loads for a given structural stiffness and loading case. It does not validate that the cross-sectional lay-out and wing weight estimation results are correct. The perfect scenario would be to compare the results of the weight estimation tool to a full-scale, functional PrandtlPlane configuration, but unfortunately these validation cases do not exist. Therefore, the decision is made to perform a preliminary validation with respect to conventional wing designs.

The state-of-the-art in Class II-1/2 wing weight estimation is the EMWET tool developed at the TU Delft.[23] The program functions similarly to the methodology described in Section 4.1. From the basic wing geometry and a set of loads, the primary wing weight is computed, after which the regression in Equation (4.35) is used to estimate the total wing weight. The main discrepancy between the two tools is the different cross-sectional design. Instead of a boom and skin model, EMWET relies on two horizontal plates to withstand the bending moments and a front and aft spar, which are sized to withstand the shear forces and torsional moments. The average error of the EMWET methodology for a range of conventional aircraft was found to be less than 2%.[23] If the results of the new methodology resemble the EMWET results closely, the closed-wing weight estimator can thus be deemed validated for conventional configurations.

Two aircraft are selected to compare EMWET to the closed-wing weight estimator in this section: the ATR-72 and the Airbus A320-200. The geometry and result of the primary weight estimation for the ATR-72 are shown in Figure 5.4a, and for the A320-200 in Figure 5.4b.

To accurately compare the results between EMWET and the closed-wing weight estimator, five adaptations were made to the methodology described in Section 4.1. Firstly, the weight of the top and bottom skin has been excluded from the analysis, since EMWET assumes their shear flows are taken up by the skins, which are sized to handle the primary bending moment. Secondly, minimum values for the boom areas are set, such that the area $A1 + A2$ is not larger than the area of an equivalent horizontal plate with a thickness of 0.8mm, which is the minimum thickness used by EMWET. Thirdly, instead of defining sweep angles for each beam element of the wing separately, a single sweep angle was used in the analysis. The sweep line is defined by connecting the elastic axis point at the root with the elastic axis point at the tip. This procedure is also used by EMWET. Fourthly, the airfoils were selected such that the neutral axis of the cross section lies on the chord line, because the closed-wing weight estimator has cross-coupled opposing booms, while the thickness in EMWET can vary between the upper and lower skin. Finally, the rib spacing in EMWET was set to such a

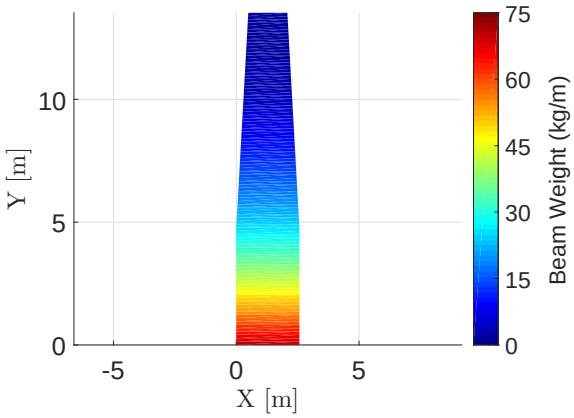

(a) Primary weight estimation results ATR-72.

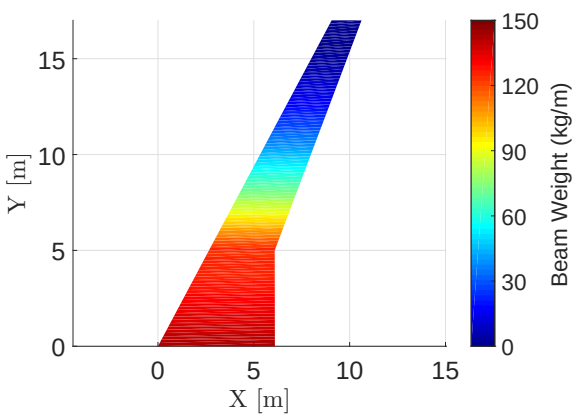

(b) Primary weight estimation results A320-200.

Figure 5.4: Primary weight estimation results closed-wing weight estimator.

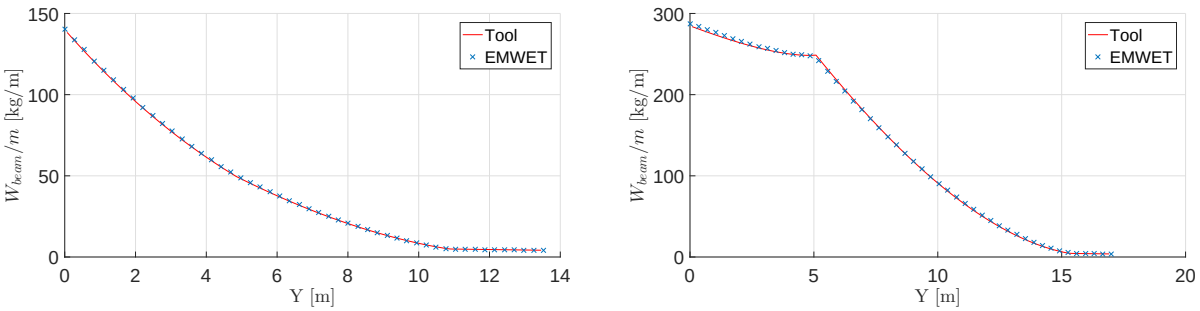

(a) Spanwise weight distribution comparison ATR-72.

(b) Spanwise weight distribution comparison A320-200.

Figure 5.5: Primary weight comparisons between EMWET and adapted closed-wing weight estimator.

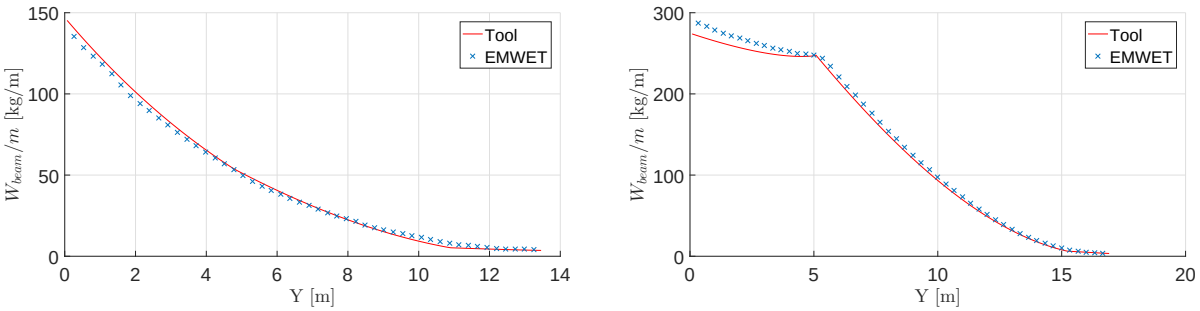

(a) Spanwise weight distribution comparison ATR-72.

(b) Spanwise weight distribution comparison A320-200.

Figure 5.6: Primary weight comparisons between EMWET and standard closed-wing weight estimator.

small value that column buckling was not taken into account during sizing, since the closed-wing weight estimator does not consider this criteria either.

The comparisons of the spanwise primary weight estimations between the tool and EMWET are shown in Figures 5.5a and 5.5b for the ATR-72 and the A320-200 respectively. For both cases the magnitude and trend of the curve is equal for EMWET and the closed-wing tool. Furthermore, the influence of the kink geometry in the A320-200 is modelled smoothly as well. The tool underestimates the primary weight of the ATR-72 by 0.6% compared to the equivalent EMWET case, and by 0.5% for the A320 reference case. By altering the methodology as described above the closed-wing weight estimator can thus accurately predict the primary weight of conventional aircraft.

To determine the influence of the five assumptions mentioned before, the same procedure is repeated without them. This compares the results of EMWET to the closed-wing weight estimator tool as it will be implemented into the Initiator. The results are shown in Figure 5.6.

The primary wing weight for the ATR-72 is now overestimated by 1.6% compared to EMWET, while it is underestimated by 3.6% for the A320-200. The main differences originate from the inclusion of buckling criteria and the sweep angles, which are now defined separately for each beam. Therefore, the wing weight is lower at the root of the wing for the A320-200, compared to the EMWET results. The differences between the two methodologies are still minor and the closed-wing weight estimator is thus validated for conventional configurations.

5.3. INFLUENCE OF ASSUMPTIONS

In this section the influence of the main assumptions made in Section 4.1 is investigated. The cross-coupling of the booms is discussed in Section 5.3.1. In Section 5.3.2 the validity of the assumptions related to the geometric height of the cross-section is determined. Finally, the influence of buckling and the shear center location are described in Sections 5.3.3 and 5.3.4 respectively. The reference geometry for the analyses performed in this section is the one presented in Chapter 4 and shown in Figure 4.3.

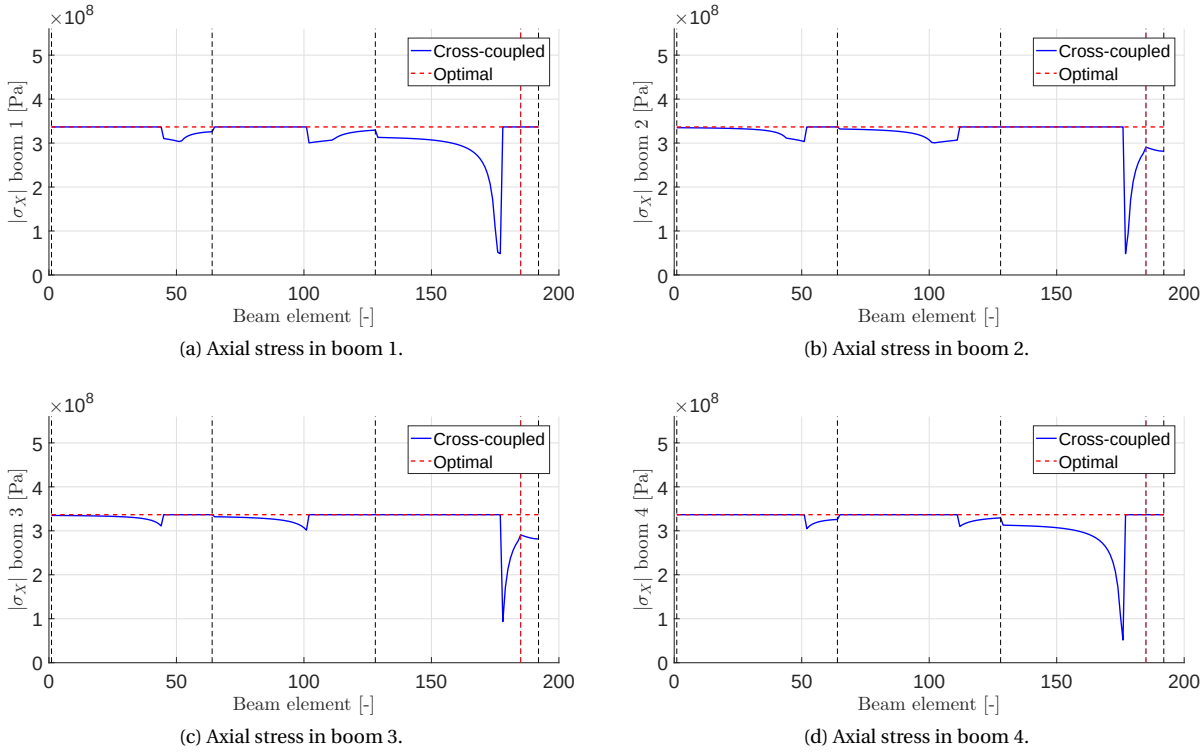

(a) Axial stress in boom 1.

(b) Axial stress in boom 2.

(c) Axial stress in boom 3.

(d) Axial stress in boom 4.

Figure 5.7: Comparison axial stresses cross-coupled and oprimal design.

5.3.1. CROSS-COUPLED BOOM MODEL

Due to the cross-coupling of opposing booms, the cross-sectional sizing results are not optimal. The normal force is assumed to increase the axial stress in both booms, while it actually reduces the stress in one of them. The axial stress in all of the booms should be determined to identify the effect of this assumption. The axial stress in the booms is calculated with Equation 5.1 and the results are compiled in Figure 5.7. The results are shown for the cross-coupled methodology as well as for an optimal design. The optimal solution was obtained by including an iteration loop, which takes the effect of a shifting center of gravity into account while sizing the booms. It should be noted that the optimal solution is not unique and different results will be obtained if a different starting point is chosen.

As expected, the optimal design has all four booms fully stressed throughout the design. However, if booms 1 and 3 are cross-coupled only one of them is guaranteed to be fully stressed at a given beam element. If boom 1 is under stressed, boom 3 is at the maximum value and vice-versa. The same pattern is visible for booms 2 and 4. The under stressing of booms happens predominantly on the rear wing. This effect can be explained by comparing the stresses to the internal loads shown in Figure 4.10. The largest discrepancies occur at a point where the internal bending moments are very small compared to the axial forces. At these locations however, the boom areas are generally small, such that the effect on the final wing weight is minor. The optimized boom areas for booms 1 and 3 are compared to the cross-coupled results in Figure 5.8.

As expected, the main discrepancies between the boom areas appear on the rear wing, where material is removed from boom 1 for the optimal design. In the cross-coupled solution boom 1 was under stressed on the rear wing, so material can be removed there. The differences however are minor: the total boom weight of the cross-coupled solution is less than 2% higher compared to the optimized solution. Using a cross-coupled system reduces the computational effort required, because the booms do not have to be sized in an iterative procedure. Furthermore, one single solution exists for the cross-coupled case, which improves the convergence behaviour of the outer stiffness loop as well. Therefore, the assumption to make use of a cross-coupled boom model is deemed valid.

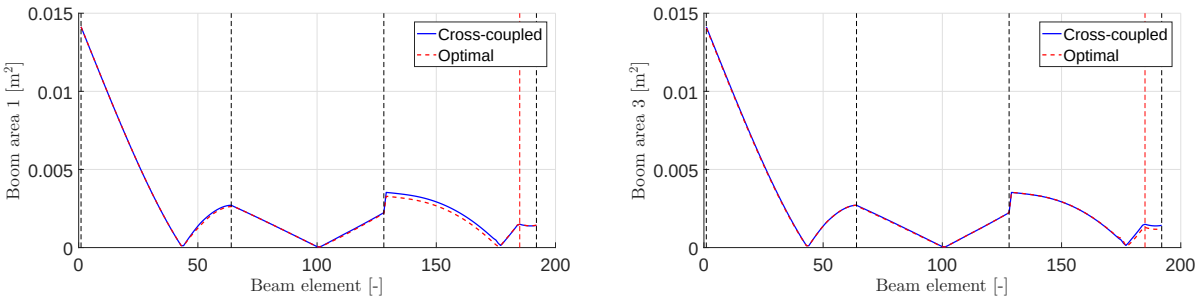

(a) Boom 1 area distribution.

(b) Boom 3 area distribution.

Figure 5.8: Comparison of boom areas for cross-coupled and optimal case.

5.3.2. CROSS-SECTIONAL HEIGHT DETERMINATION

In Section 4.1 the assumption was made, that the height of a cross-section only depends on the shape of the airfoil and not on the thickness of the aircraft skin. This reduces Equation (4.21) to Equation (4.22). The main advantage of this assumption is that the cross-sectional height does not depend on the boom areas. Therefore, no additional loop is required during the cross-sectional sizing. The obvious drawback is that the height of the cross-section will be slightly overestimated, leading to a lower final wing weight. Two wing weight estimations were run to quantify these advantages and drawbacks. The analysis was performed on the reference case introduced in Section 4.1.

The stiffness iteration loop for the analysis, in which the skin thickness is neglected, converges in 13.3 seconds and determines the total wing weight to be 8688 kg. If the effect of the skin thickness on the cross-sectional height is included in the analyses, the stiffness iteration loop takes 39.3 seconds and the final wing weight is found to be 8840 kg. Neglecting the airfoil skin thickness thus leads to an underestimation of the wing weight of 1.7%, while the computational time decreases with 67%, with respect to the case in which the arfoil skin thickness is taken into account. Keeping the constraints on computational time during a conceptual design into account, the assumption is deemed reasonable.

5.3.3. BUCKLING BEHAVIOUR

Buckling was excluded from the closed-wing weight estimation for two main reasons. First, including buckling criteria in the cross-sectional sizing reduces the convergence behaviour of the outer stiffness iteration loop. If beams are sized for buckling criteria in one iteration and for the static yield stress in a subsequent iteration, jumps in the primary weight will be encountered. This state-switching behaviour could lead to the tool getting stuck in the convergence loop. Furthermore, since the shear flow distribution in the skins depends on the boom areas, their thicknesses will fluctuate between two states as well. Secondly, simple column buckling criteria might not be accurate enough to capture the buckling behaviour in closed-wing configurations. Demasi et al. determined that linear buckling analyses can grossly under- and over-predict the capabilities of the design to withstand buckling.[33] Nevertheless, to obtain an approximation if buckling could prove to be a design driver, the column buckling behaviour of the reference case is investigated here.

First, the shape of the flange supports, which carry the axial loads should be decided upon. For this analysis, the cross-sections of the boom reinforcement are assumed to be equal legged angles, as shown in Figure 5.9. The moment of inertia of these shapes depends on the ratio between their thickness and length. The length and thickness of the section are computed with the area of the boom and the T/L ratio as shown in Equation (5.2).

$$L = \sqrt{\frac{A}{2\,{}^{T}\!/_{L} - \left({}^{T}\!/_{L}\right)^{2}}} \qquad T = \left({}^{T}\!/_{L}\right) L \tag{5.2}$$

The moment of inertia then follows from Equation (5.3).

$$I = \frac{T\left(5L^2 - 5LT + T^2\right)\left(L^2 - LT + T^2\right)}{12\,(2L - T)} \tag{5.3}$$

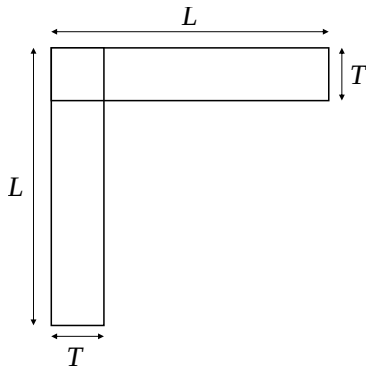

Figure 5.9: Shape definition of the flange supports.

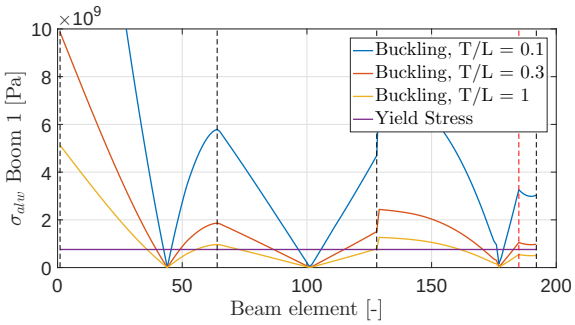

(a) Maximum allowable normal stress in boom 1.

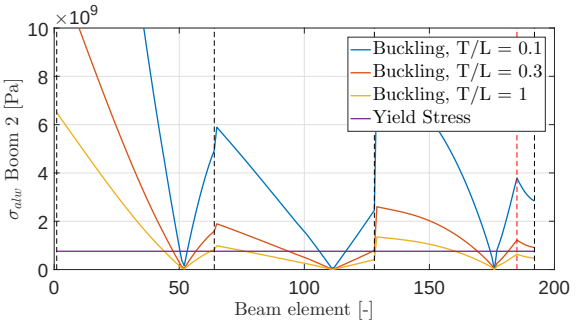

(b) Maximum allowable normal stress in boom 2.

Figure 5.10: Comparison of allowable yield and buckling stresses.

Finally, the critical column buckling stress is computed with Equation (5.4), in which the rib spacing is assumed to be 0.5 meters for the reference case.

$$\sigma_{\text{alw,buckling}} = \text{fos} \cdot \frac{\pi^2 EI}{l_{\text{rib}}^2 A} \tag{5.4}$$

The maximum allowable normal stress in boom 1 and 2 throughout the reference design is shown in Figure 5.10. The analysis has been performed for three different thickness over length ratios of the flange support. If the allowable buckling stress drops below the allowable static yield stress the cross-section should be sized to withstand buckling and the current methodology will underestimate the wing weight. The lateral wing seems to be the most susceptible to buckling, due to the small cross-sectional area of the flange supports as seen in Figure 4.12.

For the lowest thickness over length ratio only a few beams experience buckling at locations where the boom areas are small as seen in Figure 4.12. With a thickness over length ratio of 0.1 for the flanges, approximately 5% of the total winspan experiences buckling behaviour. However, for larger thickness over length ratios more elements in the wing should be sized to resist buckling instead of the static yield stress. For a thickness over length ratio of 1.0, in which the support are square-shaped, 40% of the total winspan should be sized to account for buckling. The validity of the assumption to neglect buckling during the closed-wing weight estimation is thus heavily dependent on the shape of the flange supports as well as the rib spacing. The additional weight added for the reference case design with a rib spacing of 0.5 m and a thickness over length ratio of 1/10 is negligible, but this might not be the case for all closed-wing designs. In the future, additional investigations into the buckling behaviour during the conceptual wing weight estimation should be carried out. These recommendations a elaborated upon further in Chapter 8.

5.3.4. SHEAR CENTER LOCATION

In the procedure of determining the thicknesses of the four skins in each cross-section, the shear center was assumed to coincide with the geometric center of the cross-section. This assumption was made to remove a

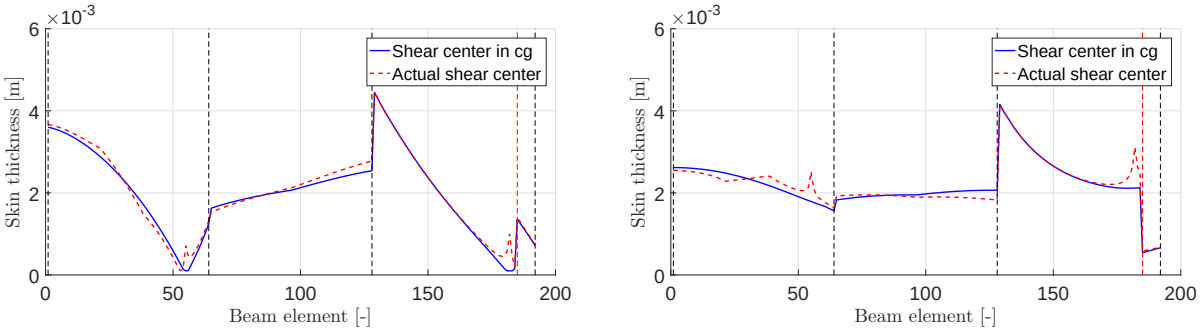

(a) Front spar thickness distribution.

(b) Rear spar thickness distribution.

Figure 5.11: Comparison of spar thicknesses for actual and assumed shear center location.

cross-sectional sizing loop, since the actual shear center location depends on the skin thicknesses, which in turn depend on the shear center location. To determine the influence of the assumption the resulting cross-sectional design for the reference case was adapted to account for the shift in shear center due to the different thicknesses of the four skins. This leads to a new closed shear flow calculation, in which Equation (4.32) is replaced by Equation (5.5). The adjusted cross-sectional sizing results for the front and rear spar are shown in Figure 5.11.

$$q_o = -\frac{\sum_{i=1}^{4} \frac{2q_i}{t_i} dA_i}{2\sum_{i=1}^{4} \frac{1}{t_i} dA_i} = -\frac{\sum_{i=1}^{4} \frac{q_i}{t_i}}{\sum_{i=1}^{4} \frac{1}{t_i}} \tag{5.5}$$

If the contributions of the four skin thicknesses are not neglected in the determination of the shear center location, the final design changes slightly. If the results are compared to the skin thickness distribution in Figure 4.12 it can be noted that the main discrepancies occur at the spanwise locations where the thickness of the front and rear spar differ the most. This could be expected, since the shear center will shift away from the geometric center the most in these cases. The total weight of all skins is 6.7% lower if the shear center is assumed to coincide with the center of gravity, compared to the case in which the shear center is computed accurately. However, the boom weight makes up the majority of the primary wing weight. Therefore, the the total wing weight only is only underestimated by 1.3% if the shear center is assumed to coincide with the center of gravity, compared to the accurate determination. Including the actual center of gravity location into the analysis would at least double the computational time required for the tool, due to the additional loop in the cross-sectional sizing. The lower computational effort required thus outweighs the increase in accuracy and the assumption is deemed valid.

6

RESULTS

The closed-wing weight estimation methodology is assumed to be verified and validated and is used to determine the sensitivity of the closed-wing weight to relevant design parameters in Section 6.1. A comparison between a conventional configuration and a PrandtlPlane is included in Section 6.2. Then, the weight estimation tool is included in the Initiator conceptual design workflow and three case studies are performed in Section 6.3 to determine the improvement over the original wing weight estimation method by Zohlandt.[11] The influence of the discrepancies in the wing weight estimations on the required fuel volume for the designs will be evaluated as well. Finally, an analysis is performed to determine the possible improvements in performance by altering the wing area distribution between the front and rear wing in Section 6.4. All analyses should provide answers to the research questions defined in Chapter 3.

6.1. PRANDTLPLANE WING WEIGHT SENSITIVITY

The goal of this section is to provide insight in the limitations and capabilities of the tool in the conceptual design phase. Therefore, the effect of altering several major design parameters on the closed-wing weight will be determined. For this analysis the closed-wing weight estimator described in Section 4.1 will be used. The following five design parameters are considered as variables: wing sweeps, span, taper ratio, longitudinal center of gravity location, fin position and fin orientation. The reference case for these analyses is the one presented in Section 4.1. The geometry of this reference design is shown in Figure 4.3. It is important to note that the analysis in this section only consider the closed-wing weight estimation results. These results are not iterated to update the center of gravity position or design weight of the aircraft in a conceptual design loop. These iterative design studies will be performed in Section 6.2.

6.1.1. WING SWEEP ANGLE

The definitions of the sweep angles of the PrandtlPlane configuration are shown in Figure 6.3. The sweep angles are all defined at half chord locations. In the following sensitivity analysis the lower wing and lateral wing are swept with the supplied sweep angle, while the upper wing is swept with the negative value. A positive sweep angle thus means that the lower wing is swept backward and the upper wing swept forward. The total wing weight and its distribution over the three surfaces is computed for a range of sweep angles. To purely focus on the effect of the sweep angle, the analysis is ran without trimming the aircraft. The reference area and span of the wings were kept constant throughout the procedure. Due to the exclusion of a trim condition and the equal sweep angles between the three surfaces, the possible conclusions drawn from the analysis are limited. However, the results should be able to indicate whether the wing wing weight and its distribution are sensitive to sweep, which is the main goal of this procedure. The sweep angles were altered in steps of one degree and the influence on the wing weight and the distribution are shown in Figure 6.1.

Both the total wing weight and weight distribution seem to depend heavily on the sweep angle of the wings. Three distinct behaviours cause this relationship. First, the aerodynamic load distribution varies with sweep angle. For highly swept wings, the front wing is loaded more than the rear wing, causing it to be heavier as well. However, it should be noted that including a trim condition would alter this distribution as will be investigated in Section 6.1.6. Secondly, the internal load distribution varies with sweep angle, since the beam orientations change. For highly swept wings, the width of the cross-sections in local y-direction is smaller.

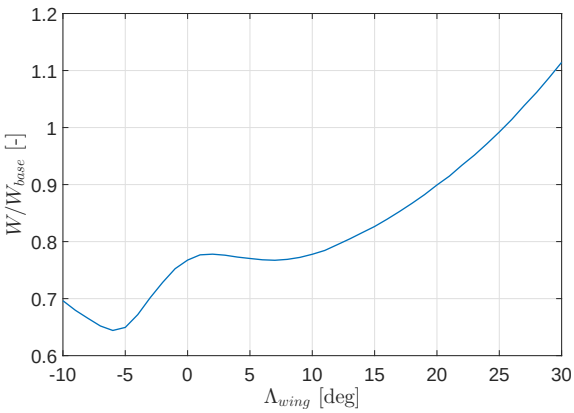

(a) Wing weight versus wing sweep angles.

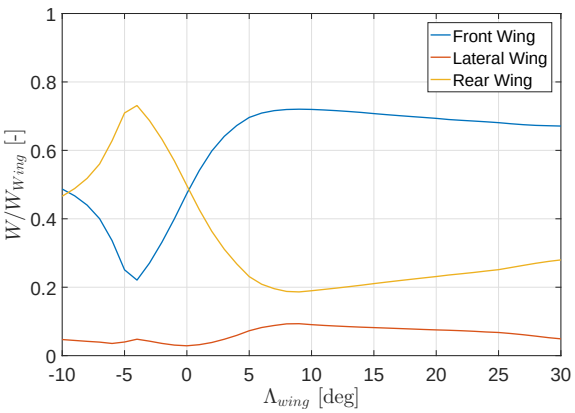

(b) Weight distribution versus wing sweep angles.

Figure 6.1: Sensitivity analysis of the wing sweep angles.

In a smaller wingbox, additional material is needed to reach the same moments of inertia. Finally, the fin orientation was kept constant in this analysis, while the rear wing orientation changes. Therefore, the internal loads due the support constraint are applied in a different beam plane. The effect of this fin orientation angle is investigated further in Sections 6.1.2 and 6.1.3.

Due to these dependencies the behaviour of the wing weight to sweep angle is not easy to predict. The general trend is that the wing weight increases with sweep angle, but the behaviour is irregular for small positive or negative sweep angles. It should be noted that the weight of the front and rear wing is almost equal for a sweep angle of zero degrees, which is in line with the expectations. For positive sweep angles, with a swept back lower wing and forward swept upper wing, the upper wing is heavier than the lower wing. Furthermore, the weight of the lateral connection elements increases when the discrepancies between the front and rear wing are high. This is as expected, since large differences between the internal loads on the front and rear wing, lead to high loads in the lateral connection as well.

6.1.2. FIN SWEEP ANGLE

The sweep angle of the front and rear wing were found to have a large influence on the total wing weight and its distribution. The fin sweep angle and rear wing sweep angle together determine the angle at which the support loads are introduced into the structure. Therefore, the fin sweep angle sensitivity is run at different wing sweep angles to compare the results. The wing reference area and span, as well as the fin dihedral angle are kept constant throughout the analysis. The definitions of the absolute fin sweep angle as well as the relative angle β are visualized in Figure 6.3. The results are shown in Figure 6.2. The continuous and dotted lines in Figure 6.2b refer to the condition of a zero and twenty degrees sweep angle on the wing surfaces respectively.

The first obvious conclusion that can be drawn from the figures is that the sensitivity to the fin sweep angle indeed depends heavily on the sweep angle of the wings. The total wing weight is much less sensitive to the fin sweep angle for a high wing sweep angle than for a low wing sweep angle. The optimal fin sweep angle also shifts with the sweep angle of the wings. The division in weight between the front and rear wing is highly dependent on the fin sweep angle. For the unswept wing, the weight distribution between the front and rear wing shifts from 40/60 to 60/40 by sweeping the fin from 10 to 20 degrees. Therefore, the fin sweep angle should be selected with care in the design of a PrandtlPlane with the closed-wing weight estimation module, especially when the sweep angles of the main wings are small.

The results shown in Figure 6.2a are displayed as a function of the angle β in Figure 6.4 to determine if the optimal fin sweep angle can be expressed as a function of the relative angle between the fin and the rear wing.

The results indicate that aligning the fin with the rear wing ($\beta = 0$ deg) does not lead to the lowest possible wing weight. The optimal relative angle between the rear wing and fin shifts with the wing sweep angle. The more swept the main wings are, the higher the optimal angle β becomes. The optimal fin sweep angle is thus not easy to predict in a PrandtlPlane design.

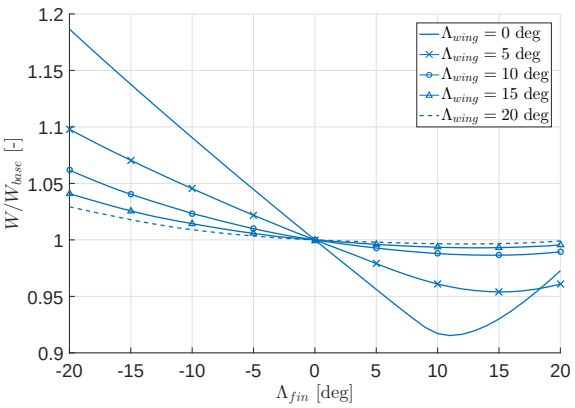

(a) Wing weight versus absolute fin sweep angle.

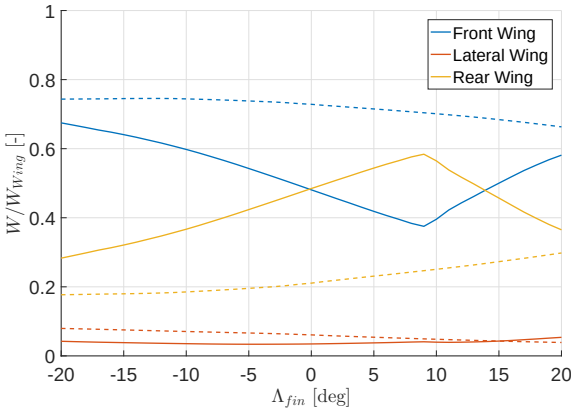

(b) Weight distribution versus fin sweep angle.

Figure 6.2: Sensitivity analysis of the absolute fin sweep angle.

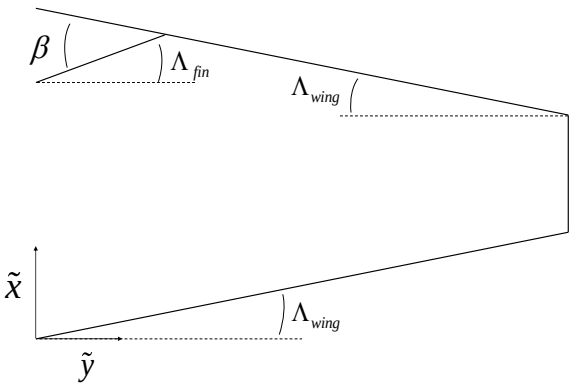

Figure 6.3: Sweep definitions of the PrandtlPlane surfaces.

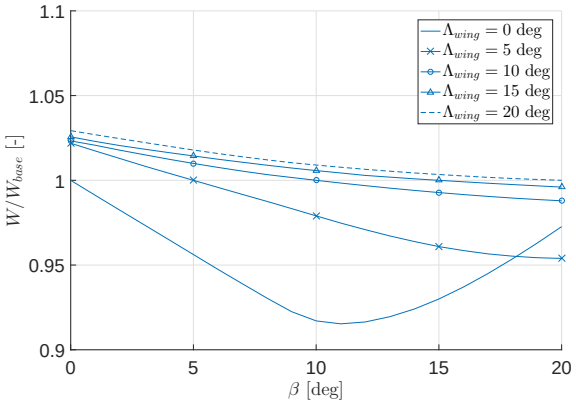

Figure 6.4: Wing weight versus relative sweep angle β.

6.1.3. FIN DIHEDRAL AND SPANWISE POSITION

In the next analysis the fin position and dihedral angle are altered. During this procedure, the root position of the fin is kept constant, while the spanwise location of the tip connection to the rear wing is changed. By altering the spanwise position at which the fin attaches to the rear wing its dihedral angle is changed accordingly, as shown in Figure 6.5. There thus exists an unique dihedral angle for a given spanwise fin position, since the root of the fin is kept fixed to the fuselage. The dihedral angle in the analysis is altered between 45 and 90 degrees with respect to the global y-coordinate. All wings and fins were kept unswept throughout the analysis. The resulting wing weights are plotted against both the spanwise fin attachment position and the dihedral angle in Figures 6.6 and 6.7 respectively.

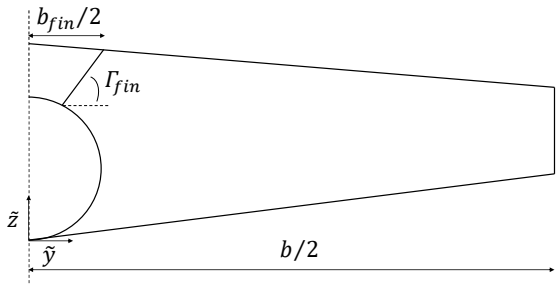

Figure 6.5: Definitions of the fin dihedral angle and spanwise position

The influence of the spanwise fin attachment position and the dihedral angle is marginal. The overall wing weight decreases for a low dihedral angle. In that case, the loads induced by the fin are more in line with

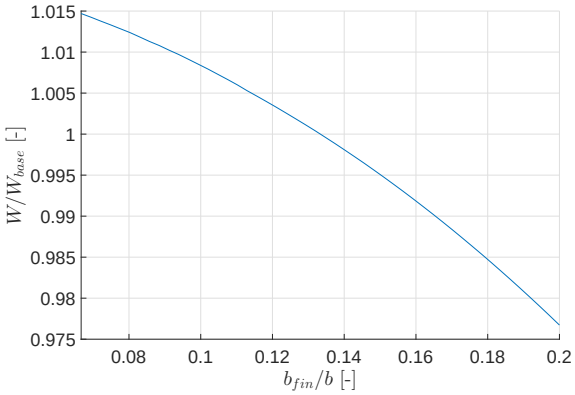

(a) Wing weight versus spanwise fin attachment position.

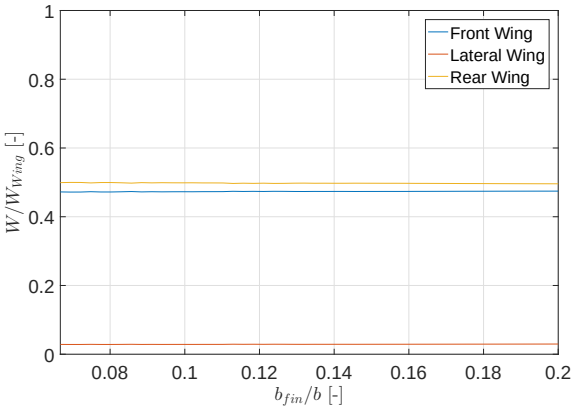

(b) Weight distribution versus spanwise fin attachment position.

Figure 6.6: Sensitivity analysis of the spanwise fin attachment position.

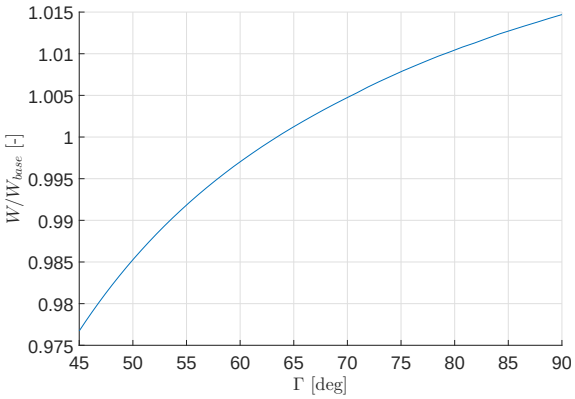

(a) Wing weight versus fin dihedral angle .

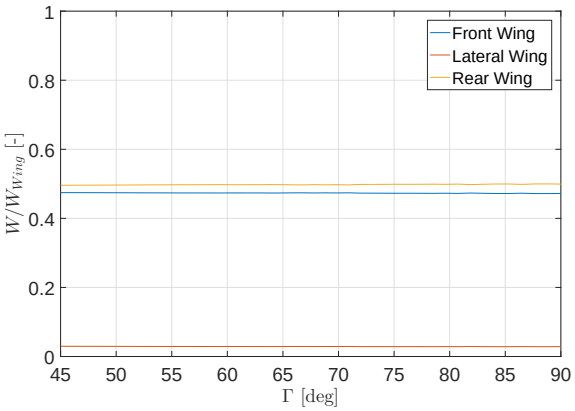

(b) Weight distribution versus fin dihedral angle.

Figure 6.7: Sensitivity analysis of the fin dihedral angle.

the rear wing beam elements and are thus better coped with. Furthermore, applying the fin constraint further away from the root lowers the bending moments in the rear wing. This slight effect is visible in Figure 6.6b, which shows that the rear wing makes up slightly less of the total weight when the fin is positioned further outboard. Overall, the effect of the fin dihedral angle and attachment position is minor compared to the effect of the wing and fin sweep angles.

6.1.4. WINGSPAN

The sensitivity of the PrandtlPlane wing weight with wingspan is determined in the following analysis. The wingspan of both the front and rear wing is varied, while the total wing area is kept constant by altering the chord lengths. Due to the high influence of the sweep angles on the wing weight, both the wing and fin sweep angles were kept at zero degrees throughout the analysis. The results on the wing weight and distribution are shown in Figure 6.8.

As expected, the wing weight of the PrandtlPlane configuration increases significantly with wingspan. An increase of 10% in the wingspan compared to the reference case, leads to an increase of 6% in the total wing weight compared to the reference case. This effect is caused by two contributions. First, due to the higher span, all forces are applied further away from the root, which leads to an increase in the internal bending moments. Secondly, since the total wing area was kept constant the chord lengths decrease for higher wingspans. Therefore, the size of the cross-sectional design decreases as well and more material is necessary to reach the same moments of inertia.

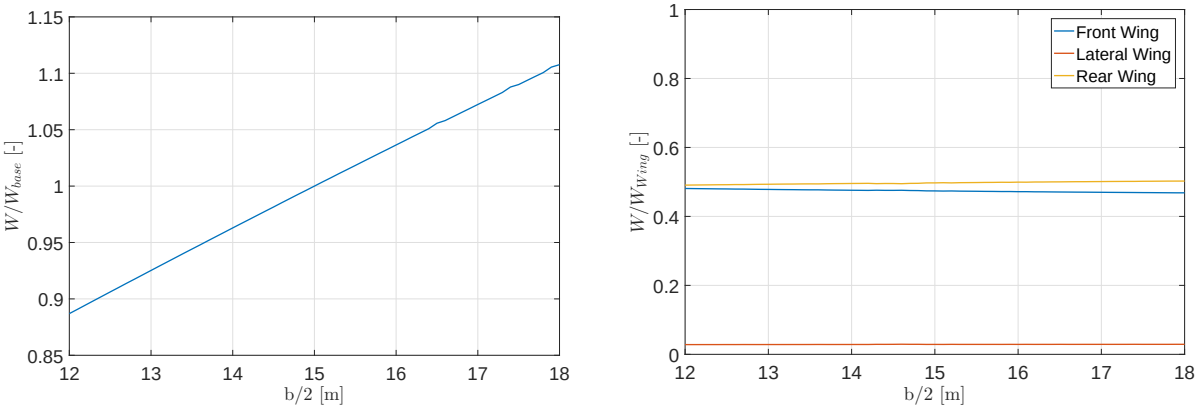

(a) Wing weight versus wingspan.

(b) Weight distribution versus wingspan.

Figure 6.8: Sensitivity analysis of the wingspan.

6.1.5. TAPER RATIO

The sweep angle of the wings was determined to have a large influence on the wing weight. Therefore, the input for the taper ratio sensitivity is altered such that the half chord sweep angle was at zero degrees for all investigated taper ratios. The taper ratio of both the front and rear wing is altered by the same factor, while the chord length of the lateral wing was chosen equal to the tip chords of the front and rear wing respectively. The total area of the front and rear wing and their span were kept constant during the analysis. The taper ratio was varied between 0.2 and 0.8 to determine the effect on the total wing weight and its distribution. The results are shown in Figure 6.9.

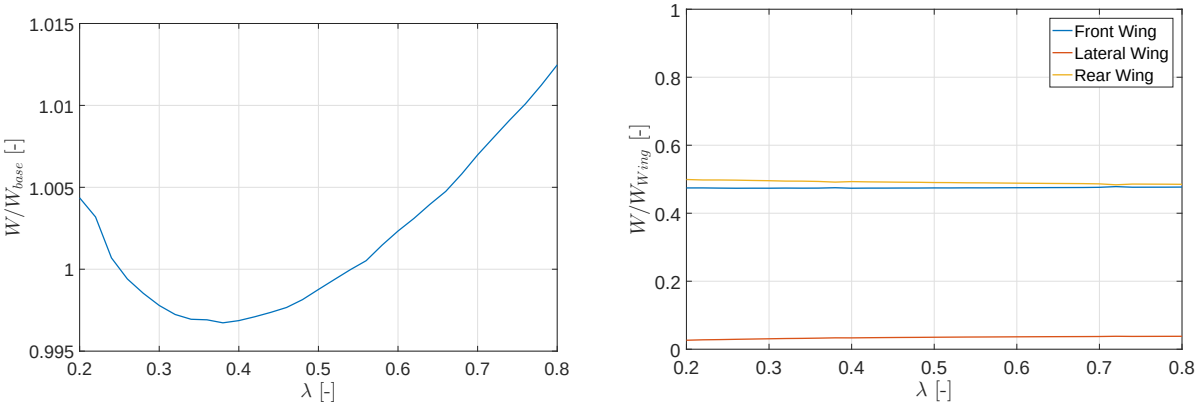

(a) Wing weight versus taper ratio.

(b) Weight distribution versus taper ratio.

Figure 6.9: Sensitivity analysis of the wing taper ratio.

The optimal taper ratio for the reference case is 0.38, but this is probably case-specific. The magnitude of the shift in total wing weight with taper is ratio is small, compared to the influence of the sweep angles and wingspan. The effect of the taper ratio on the wing weight consists of two contributions. First, for a highly tapered wing the fuel is located more inboard, which decreases the bending relief and thus increases the total weight of the wing. A second effect can be distinguished as well. A highly tapered wing has higher chord lengths near the root of the front and rear wing. Due to the high chord length, and thus larger wingbox, less material is required to achieve the same moments of inertia compared to a smaller wingbox. It is thus beneficial to have the highest chord lengths at the spanwise positions with the maximum bending moments. For the reference case, the bending moments were high at the front wing root and rear wing tip. Therefore, a small taper ratio is beneficial to reduce the weight on the front wing, but will lead to an increase in weight on the rear wing. This effect is visible in Figure 6.9b as well.

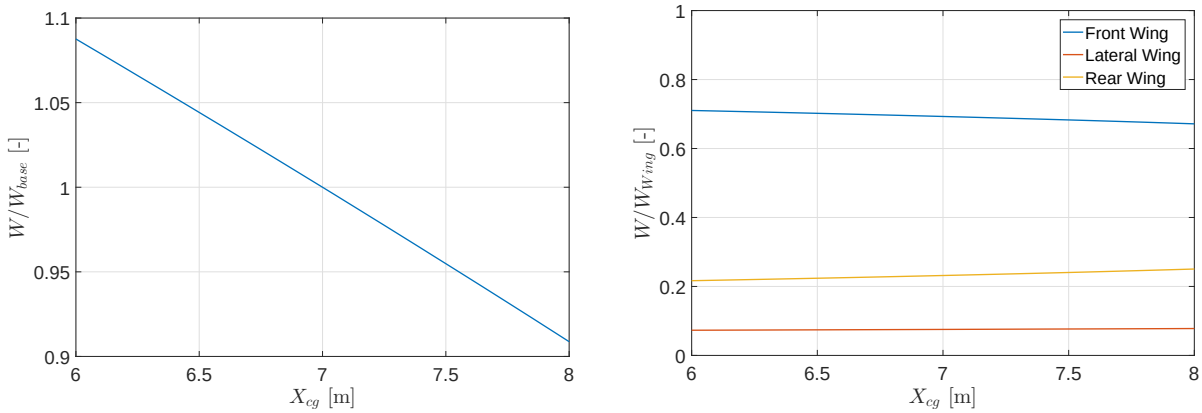

(a) Wing weight versus longitudinal cg position.

(b) Weight distribution versus longitudinal cg position.

Figure 6.10: Sensitivity analysis of the longitudinal centre of gravity position.

6.1.6. LONGITUDINAL CENTER OF GRAVITY POSITION

All previous sensitivity studies were performed without trimming the configuration. In this case, the aircraft will be trimmed and the influence of the longitudinal center of gravity location on the wing weight will be determined. The trim condition can also be altered by changing the wing sweep angles, so those were kept constant at 20 degrees throughout the analysis. It should also be noted that the influence of the the updated wing weight is not fed back to update the center of gravity position. This overall feedback loop is included in the Initiator analysis in Section 6.3. In order to trim the configuration the pitching moment around the center of gravity is set to zero in the AVL run case. The elevators on both the front and rear wings run from the root to 25% of the wingspan. The elevators are coupled through a set of gains. The rear wing elevators have a gain of 1.0, and the ones on the front wing of -0.1. The elevators thus deflect opposite from each other, with the front wing elevators deflecting less than the rear ones. This set-up of the elevators is not necessarily optimal to minimize the trim drag or obtain the minimum wing weight. However, the main goal of this analysis is to determine whether altering a trim condition has a significant influence of the wing weight results. Determining the optimal set-up of the control system should be performed during a conceptual optimization study, but is out of the scope of this research. The results of varying the longitudinal center of gravity position are shown in Figure 6.10.

For the specific configuration a rearward shift in the longitudinal center of gravity position leads to a significant decrease in the total wing weight. When the center of gravity is shifted backwards, the aerodynamic loads increase on the rear wing and decrease on the front wing. The corresponding effect on the wing weight is visible in Figure 6.10b, in which the rear wing weight increases if the center of gravity moves to the rear. It is interesting to note that the total wing weight decreases for configurations with a rear center of gravity in which more elevator deflection is necessary. Shifts of 0.5 meter, 1/6 c_{mac}, can already alter the computed wing weight by 5%. It is thus necessary to include trim in each design study and correctly define the critical center of gravity position in the loading case.

6.2. CLOSED-WING WEIGHT ESTIMATION OF DIFFERENT CONFIGURATIONS

A comparison is now provided between three different wing configurations. One PrandtlPlane configuration, with an unswept fin is analysed. The second configuration has the same geometry, but the fin support is removed and the symmetry constraint at the rear wing root is replaced by a clamp. The two configurations thus feature the same h/b ratio, but their constraint definition is different. Finally, a conventional wing with the same total wing area and aspect ratio was analysed with the closed-wing weight estimation methodology. Due to the different lay-outs of the configurations, none of the designs were trimmed. All designs produce the same amount of total lift. The analyses were performed for a range of sweep angles and the results are compiled in Figure 6.11.

The first notable difference between the three configurations is the shape of the total wing weight plot. Both the clamped and conventional configuration have their minimum weights for small sweep angles and the results look symmetric around the zero degree sweep angle. The PrandtlPlane configuration however,

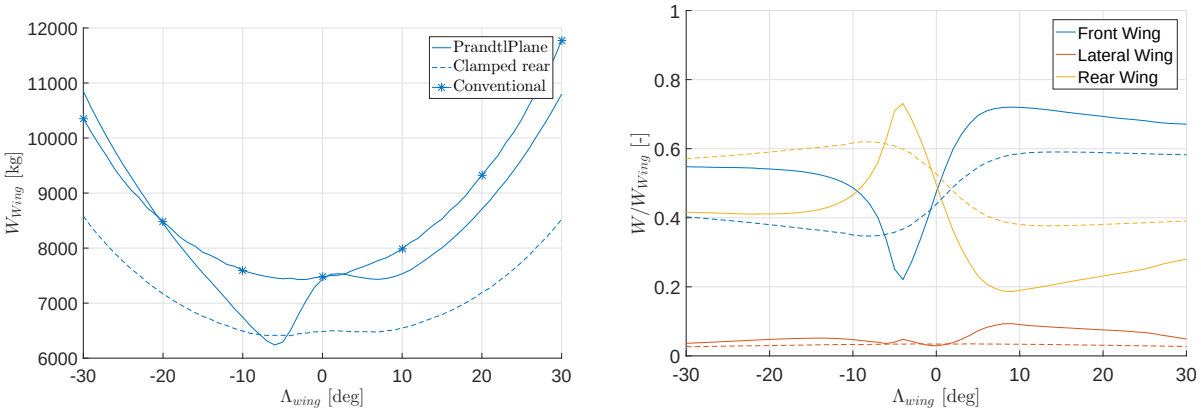

(a) Wing weight versus rear wing lay-out.

(b) Weight distribution versus rear wing lay-out.

Figure 6.11: Wing weight comparison for different configurations.

shows less predictable behaviour, due to the effects discussed in Section 6.1.1. The PrandtlPlane configuration is heavier than the clamped case, but lighter than the conventional configuration. It should be noted however that none of the three design have been optimized and these conclusions might differ for other design parameters.

For the clamped configuration, the weight distribution between the front and rear wing is as expected. For positive sweep angles the front wing is heavier due to the increased loads and this effect is reversed for negative wing sweep angles.

The results for the PrandtlPlane case should be interpreted with care, since it was concluded in Section 6.1.2 that these results depend heavily on the sweep angle of the fin support as well. The weight is distributed equally between the front and rear wing when the wings are unswept. For positive sweep angles the front wing is heavier. Finally, the lateral wing weight for the PrandtlPlane seems to be correlated to the weight discrepancy between the front and rear wing. the larger the difference between the front and rear wing, the heavier the lateral wing becomes. This is due to the fact that discrepancies in the internal loads between the front and rear wing have to be absorbed by the lateral wing.

6.3. CLOSED-WING WEIGHT ESTIMATION IN THE INITATOR

The next analysis aims to answer the primary research question. A comparison is made between the Initiator workflow that uses the EMWET methodology described before and the Initiator design that includes the closed-wing weight estimation. Three different case studies are performed for this analysis: A single aisle, medium range mission (PrP-144), a twin aisle, high range mission (PrP-270) and finally a high payload, low range mission (PrP-514).

Since the differences between the methodologies are expected to be influenced by the trim condition, all analyses are performed for both a trimmed and an untrimmed case. In the untrimmed analyses, the induced drag and lift distribution for the structural analysis are determined without inducing a zero pitching moment requirement on the solution. For the trimmed analyses, elevators are designed on both the front and rear wing, which run from the root to 25% of the wingspan. The elevators are coupled by a gain of 1.0 on the rear wing and -0.1 on the front wing. During the aerodynamic computations, the required pitching moment around the center of gravity is set to zero. The corresponding elevator deflections have an effect on the drag of the configuration and the lift distribution for the structural analysis. It should be noted that this lay-out of control surfaces is not necessarily optimal, but is should allow to define magnitude of the effect of the trim condition on the conceptual aircraft design.

In contrast with the analyses in Sections 6.1 and 6.2, the studies in this section take the results of the closed-wing weight estimation on the conceptual aircraft design into account. The wing weight and its distribution are used in subsequent iterations of the Initiator to define a new geometry, design weight and center of gravity position.

The main design variables were selected equal to those by Zohlandt, who performed optimization studies on these aircraft.[11] While the results of these optimization studies might no longer hold, the designs will

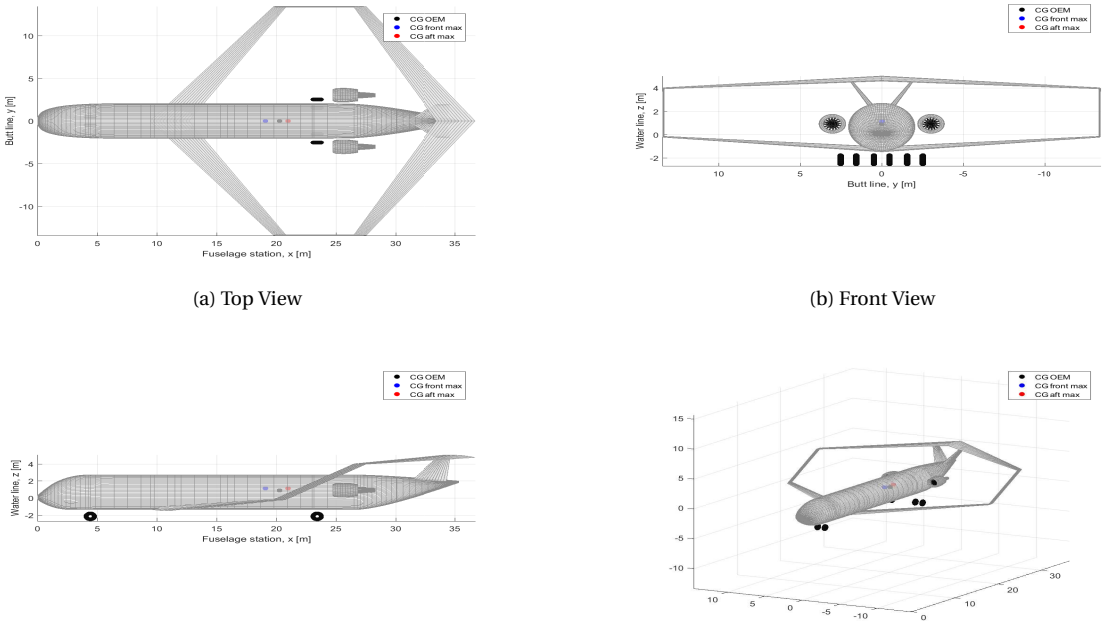

(a) Top View

(b) Front View

(c) Side View

(d) 3D View

Figure 6.12: PrP-144 Aircraft geometry (trimmed,CWWE).

Table 6.1: PrP-144 weight comparison EMWET and CWWE.

	Untrimmed			Trimmed		
	EMWET	**CWWE**	**Difference**	**EMWET**	**CWWE**	**Difference**
Maximum take-off mass	60170 kg	62940 kg	4.6%	61990 kg	64020 kg	3.3%
Operational empty mass	30442 kg	32810 kg	7.8%	31901 kg	33692 kg	5.6%
Payload mass	19500 kg	19500 kg	0%	19500 kg	19500 kg	0%
Total fuel mass	10228 kg	10630 kg	3.9%	10589 kg	10828 kg	2.3%

provide a baseline from which the influence of the new closed-wing weight estimator can be determined.

6.3.1. SINGLE AISLE, MEDIUM RANGE MISSION

The first study focusses on the single aisle, medium range mission defined in Section 4.2.5. This design transports 144 passengers, with a total payload weight of 19500 kg over 4000 km. The design corresponding to the trimmed analysis with the closed-wing weight estimator is shown in Figure 6.12.

The design features two slightly swept back fins that connect to the rear wing. The two engines are attached to the fuselage. The influence of the different methodologies on the design weights is shown in Table 6.1. The discrepancies in the weight of the wings is shown in Table 6.2.

The effect of the new closed-wing weight estimation is visible for both the trimmed and untrimmed cases. If the closed-wing weight estimator is implemented, the total wing weight increases by 17.4% and 24.9% re-

Table 6.2: PrP-144 wing weight comparison EMWET and CWWE.

	Untrimmed			Trimmed		
	EMWET	**CWWE**	**Difference**	**EMWET**	**CWWE**	**Difference**
Front wing	4722 kg	3384 kg	-28.3%	5736 kg	5731 kg	-6.4%
Lateral wing	596 kg	588 kg	-1.3%	686 kg	521 kg	-24.1%
Rear wing	2633 kg	5962 kg	126%	2720 kg	4842 kg	78%
Total	7951 kg	9934 kg	24.9%	9142 kg	10734 kg	17.4%

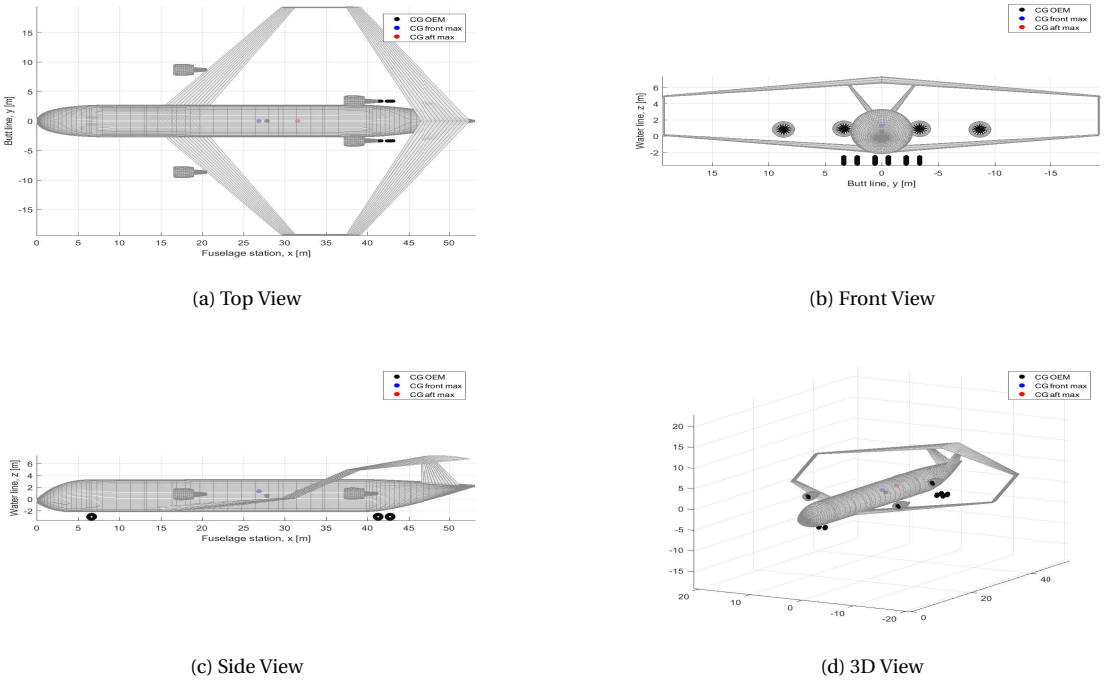

(a) Top View

(b) Front View

(c) Side View

(d) 3D View

Figure 6.13: PrP-270 Aircraft geometry (trimmed,CWWE).

Table 6.3: PrP-270 weight comparison EMWET and CWWE.

	Untrimmed			Trimmed		
	EMWET	**CWWE**	**Difference**	**EMWET**	**CWWE**	**Difference**
Maximum take-off mass	186670 kg	197900 kg	6.0%	195010 kg	203320 kg	4.3%
Operational empty mass	79452 kg	86917 kg	9.4%	84300 kg	89689 kg	6.4%
Payload mass	41000 kg	41000 kg	0%	41000 kg	41000 kg	0%
Total fuel mass	66218 kg	69983 kg	5.7%	69710 kg	72631 kg	4.2%

spectively, compared to the EMWET methodology. The result of the higher wing weight is that the total required fuel mass for the mission increases by 3.9% in the untrimmed case and by 2.3% in the trimmed design, compared to the EMWET designs. Besides a large discrepancy in the total wing weight, a large difference in the weight distribution between the three wings can be distinguished as well. In the untrimmed EMWET design the front wing is around 2000 kg heavier than the rear wing, but this distribution is reversed for the closed-wing weight estimation results. The EMWET methodology is thus not only inaccurate in estimating the total wing weight, it also fails to provide an accurate estimation of the weight distribution between the three surfaces. The design that takes the trim condition into account with the closed-wing weight estimator requires 1.9% more fuel compared to the untrimmed analysis. The additional drag and shift in lift distribution due to trimming should thus be taken into account when determining the influence of the wing area ratio in Section 6.4.

6.3.2. TWIN AISLE, HIGH RANGE MISSION

The twin aisle, high range mission is designed to carry 270 passengers over a range of 10500 km with a total payload mass of 41000 kg. The same comparison studies are performed as before to determine the influence of the new closed-wing weight estimator on this design mission. The lay-out of the design for the trimmed case, designed using the closed-wing weight estimator is shown in Figure 6.13.

In contrast to the previous design, the long-range mission design features forward swept fins. Furthermore, since two engines on the fuselage were not sufficient, an additional pair of engines was attached to the front wing. It should be noted that the effect of these engines on the wing weight estimation is neglected in both methodologies. The results of the analyses are summarised in Tables 6.3 and 6.4.

Table 6.4: PrP-270 wing weight comparison EMWET and CWWE.

	Untrimmed			Trimmed		
	EMWET	**CWWE**	**Difference**	**EMWET**	**CWWE**	**Difference**
Front wing	13410 kg	19223 kg	43.3%	15245 kg	20460 kg	34.2%
Lateral wing	1572 kg	892 kg	-43.3%	1723 kg	1142 kg	-33.7%
Rear wing	5972 kg	7212 kg	20.8%	6000 kg	6817 kg	13.6%
Total	20954 kg	27327 kg	30.4%	22968 kg	28419 kg	23.7%

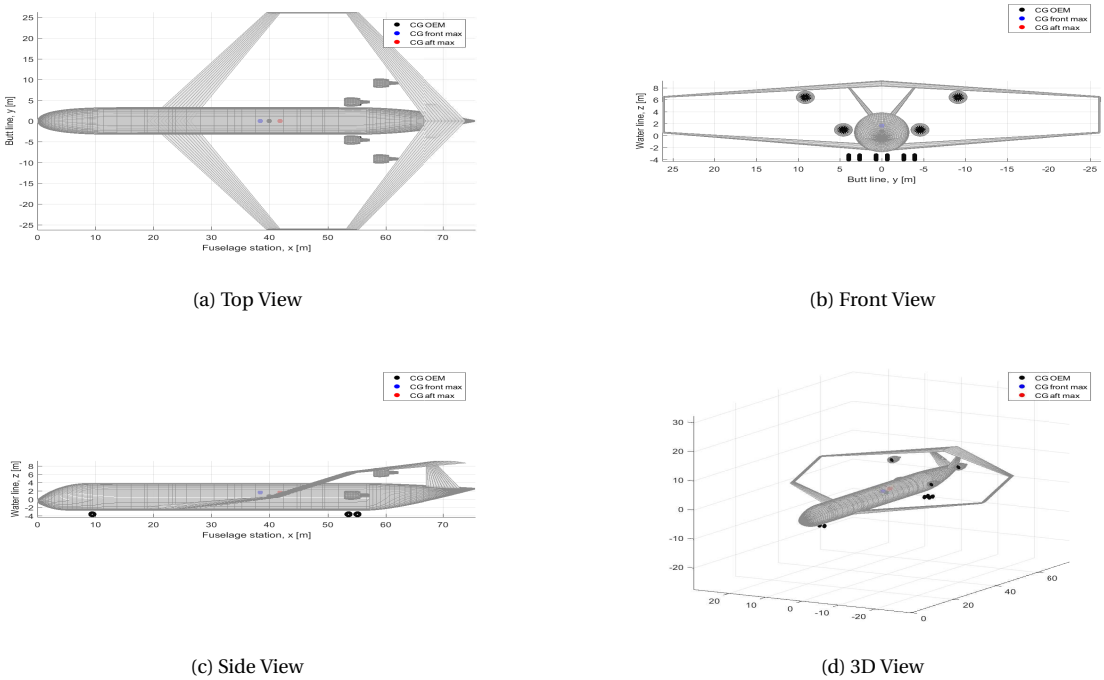

(a) Top View

(b) Front View

(c) Side View

(d) 3D View

Figure 6.14: PrP-514 Aircraft geometry (trimmed,CWWE).

The results are in accordance with those of the single aisle design. The total wing weight increased with 30.4% and 23.7% with the closed-wing weight estimator compared to the EMWET methodology, for the untrimmed and trimmed case respectively. The weight distribution between the wings has also changed, with a larger part of the total wing weight concentrated in the front wing. Furthermore, the weight estimation of the lateral wing is overestimated by the EMWET methodology. The empirical factor used in the EMWET methodology to estimate its weight, might thus not hold for larger aircraft. Due to the increase in estimated wing weight, the fuel required for the mission increases with 5.7% and 4.2% with the closed-wing weight estimator compared to the EMWET methodology, for the untrimmed and trimmed case respectively. The design that takes the trim condition into account with the closed-wing weight estimator requires 3.8% more fuel compared to the untrimmed analysis. An optimization of the design might reduce this effect, but it is clear that the trim condition has a large influence on the overall aircraft performance.

6.3.3. HIGH PAYLOAD, LOW RANGE MISSION

Finally a high payload, low range mission is investigated. The design should carry 514 passengers over 2500km with a total payload weight of 68700 kg. This mission is selected since it plays into one of the main strengths of the PrandtlPlane configuration. It can transport large payloads, while keeping the total wingspan limited, because it features two wings. Four initiator designs were created to compare the influence of trimming and the new closed-wing weight estimation module for this mission. The design that was created with the closed-wing weight estimator and that took the trim condition into account is shown in Figure 6.14.

Just as in the previous design, the two fins are swept forward. Furthermore, additional engines are required, which are positioned under the rear wing. The results of the analyses comparing the different method-

Table 6.5: PrP-514 weight comparison EMWET and CWWE.

	Untrimmed			Trimmed		
	EMWET	**CWWE**	**Difference**	**EMWET**	**CWWE**	**Difference**
Maximum take-off mass	248480 kg	244010 kg	-1.8%	249940 kg	247070 kg	-1.1%
Operational empty mass	146764 kg	142829 kg	-2.7%	147983 kg	145322 kg	-1.8%
Payload mass	68700 kg	68700 kg	0%	68700 kg	68700 kg	0%
Total fuel mass	33016 kg	32481 kg	-1.6%	33257 kg	33048 kg	-0.6%

Table 6.6: PrP-514 wing weight comparison EMWET and CWWE.

	Untrimmed			Trimmed		
	EMWET	**CWWE**	**Difference**	**EMWET**	**CWWE**	**Difference**
Front wing	28068 kg	30231 kg	7.7%	29168 kg	32204 kg	10.4%
Lateral wing	3172 kg	943 kg	-70.3%	3264 kg	1050 kg	-67.8%
Rear wing	11043 kg	9220 kg	-16.5%	11080 kg	9745 kg	-8.1%
Total	42283 kg	40394 kg	-4.5%	43512 kg	42999 kg	-1.2%

ologies are compiled in Tables 6.5 and 6.6.

In comparison to the two previous mission, the differences between the new closed-wing weight estimation methodology and the EMWET module are smaller. For the untrimmed case, EMWET overestimates the wing weight by 4.5% for the untrimmed case and by 1.2% for the trimmed design compared to the closed-wing weight estimator results. For the two other missions, EMWET actually underestimated the wing weight. The offset between the two methodologies is thus case-specific and no clear trend can be distinguished. Just as for the twin-aisle design, the empirical factor used by Zohlandt to determine the lateral wing weight is completely off. The influence of the new closed-wing weight estimation module on the fuel weight of the design is -1.6% or -0.6% compared to Zohlandts methodology, for the untrimmed or trimmed design respectively. Furthermore, the differences between the untrimmed and trimmed cases are smaller for this mission as well. The design that takes the trim condition into account with the closed-wing weight estimator requires 1.7% more fuel compared to the untrimmed analysis.

6.3.4. OVERVIEW OF THE CONCEPTUAL DESIGN STUDIES

The comparisons between the EMWET methodology implemented in the Initiator by Zohlandt and the new closed-wing weight estimator differ significantly for different aircraft sizes and configurations. The offset in total wing weight estimation between the methodologies varies between -1.2% and 23.7% with respect to the original methodology for trimmed analyses. The discrepancies between the two methodologies are thus dependent on the specific design lay-out. Therefore, no clear relationship between the adapted conventional methodology and the more accurate closed-wing weight estimator can be distinguished. Furthermore, the distribution in weight between the different surfaces is not captured accurately in the original methodology. Combined with the fact that a trim condition was determined to have a large influence on the performance of the design, the EMWET methodology is deemed inaccurate in the conceptual design of closed-wing configurations. These offsets in wing weight lead to a maximum under-prediction in required fuel weight by the original methodology of 4.2% for a trimmed analysis, compared to the new workflow with the closed-wing weight estimator. Further investigations into the conceptual design of closed-wing configurations should thus include the newly developed closed-wing weight estimator.

6.4. DESIGN SENSITIVITY TO WING AREA RATIO

In all analyses in this chapter and in previous research, the total wing area was split equally between the front and rear wing. However, the second research question aimed to define the effect of altering the area distribution between the front and rear wing in the PrandtlPlane configuration. Previously, performing such an analysis was impossible, since the effect of the altered area distribution on the wing weight was not captured accurately. The single aisle, medium range design is altered to determine the effect of the area ratio on the final design. The designs were trimmed with the same control definition as described in Section 6.3. The influence on the total wing weight and wing weight distribution is shown in Figure 6.15b. The effect on the design masses is shown in Figure 6.15a. Note that these designs are not necessarily optimized. Only the wing

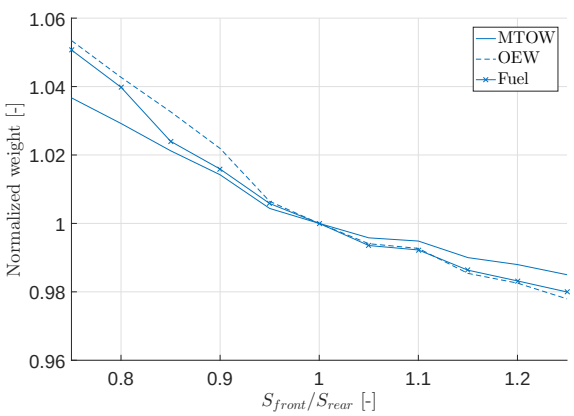

(a) Wing area ratio versus design weights.

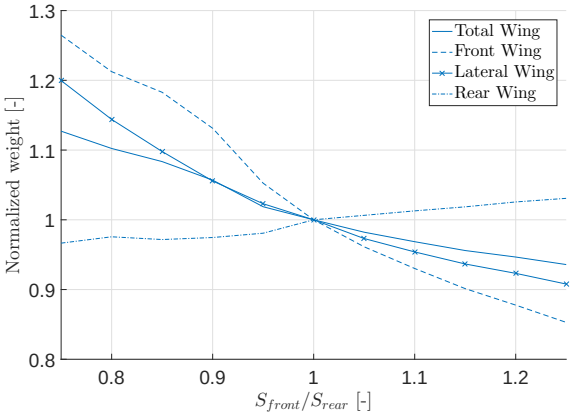

(b) Wing area ratio versus wing weights.

Figure 6.15: Effect of the wing area ratio on the PrP-144 design and performance.

area ratio has been altered between the different designs.

The results show a potential to improve the PrandtlPlane design by varying the area distribution between the front and rear wing. For the current design, an increased area ratio of 1.25 lowered the required fuel mass by 2% compared to a design with an area ratio of 1.0. This effect can mainly be contributed to a lighter wing, as can be seen from Figure 6.15b. For the higher area ratios the weight of the rear wing increases slightly, but this is countered by a larger decrease in front wing weight. These findings are the results of the trimming of the configuration. The center of gravity was located closer to the front wing than the rear wing. Therefore, the front wing had to produce a greater amount of lift compared to the rear wing, which led to high elevator deflections. However, by increasing the area of the front wing and reducing that of the rear wing, less elevator deflection was necessary and a lighter configuration could be achieved. Furthermore, since the internal moments were larger on the front wing it benefits more from the increased size of the wingbox following from the larger wing area, which leads to a decrease in total wing weight. It should be noted that these results are case-specific, but they show the large influence the area distribution between the front and rear wing in a PrandtlPlane configuration can have.

7

Conclusions

The goal of this research was to create a closed-wing weight estimation methodology to be used in the conceptual design of PrandtlPlanes. The methodology has been developed using a semi-analytical approach. The primary weight is estimated using a closed-wing design methodology which takes the over-constrained structure, titled bending axis and fin support into account. A stiffness iteration loop is implemented in which the internal loads are determined using the displacement method and all cross-sections are sized. These cross-sections feature four cross-coupled booms and four skins. Secondary weights are added using empirical relationships, after the primary weight estimation loop has converged. The methodology was verified with a finite element solver to determine that the resulting design can indeed handle the applied loads and was validated against a state-of-the art conventional wing weight estimation tool.

From the results of the sensitivity analyses several conclusions can be drawn. First, the total wing weight is most sensitive to the wing sweep angle, fin sweep angle, wingspan and trim condition. These parameters should thus be selected with care when using the methodology in a closed-wing conceptual design. Wing taper and fin dihedral angle were found to be of less importance. Secondly, the distribution of the wing weight between the three different surfaces was also greatly influenced by the wing sweep angle, fin sweep angle and trim condition. Finally, the sensitivity of the wing weight and its distribution to the wing sweep angle and fin sweep angle is strongly coupled. The wing weight was most sensitive to the fin sweep angle for low wing sweep angles. These parameters should thus be varied separately in the optimization of a PrandtlPlane configuration.

In comparing three different configurations to each other it was concluded that the closed-wing with a clamped rear wing root has the lowest total wing weight, followed by the PrandtlPlane and the conventional configuration. Furthermore, the influence of the wing sweep angle on the total wing weight proved erratic for the PrandtlPlane configuration, with the optimal configuration not featuring zero degrees sweep. This behaviour was not visible for the conventional and clamped closed-wing configurations. The unexpected behaviour of wing weight with low sweep angles is thus caused by the loads which are induced into the structure through the fins.

After implementing the closed-weight estimator in the Initiator the influence on the PrandtlPlane design was studied. It was found that the original method, which ran EMWET for the front and rear wing underestimated the total wing weight by as much as 23.7% compared to the closed-wing weight estimator for the twin-aisle configuration, if a trim condition was included. Even higher offsets, up to 30.7%, between the two methodologies were found if no trim condition was imposed. Therefore, it can be concluded that the old methodology was not accurate in estimating the wing weight of closed-wing configurations. The influence of the wing weight discrepancies on the overall design performance were large as well. The new design flow estimated the required fuel mass to be 4.2% higher for the twin-aisle long range mission and 1.2% lower for the short range high payload mission compared to the previous methodology featuring EMWET, if a trim condition was included. It can thus not be concluded that the new wing weight estimation always improves or degrades the performance of the aircraft compared to the old methodology, but it does show that the influence on the overall aircraft performance is large. It is important to note that the discrepancies between the original methodology and the closed-wing weight estimator are case-specific and that no clear relationship between the results can be distinguished. Therefore, new design and optimization studies should include the closed-wing weight estimator, instead of relying on relationships between conventional and closed-wing

configurations.

Not only the total wing weight estimation showed great discrepancies between the two methodologies. Due to the inability of the EMWET methodology to capture closed-wing characteristics, such as the tilted bending axis and over-constrained structure, the wing weight distribution between the three surfaces not determined accurately. The old methodology determined the lateral wing weight as a percentage of the total wing weight, but this assumption was more than 70% off for the high payload, low range configuration. The corresponding shifts in center of gravity position have an influence on the performance estimation of the configurations. For the single aisle, medium range configuration the required fuel weight increases by 3.9% compared to the EMWET methodology by implementing the closed-wing weight estimation if trimming is neglected, but only by 2.3% if trimming is taken into account. It can thus be concluded that significant improvements in the estimation of the total wing weight, its distribution and the overall performance of the PrandtlPlane configuration can be obtained by implementing the closed-wing weight estimator.

Finally, the inclusion of the new weight estimation methodology opens the door to explore the option of altering the area distribution between the wings to find an optimal design. Previously this was impossible, because the influence on the wing weight was not accounted for properly. The sensitivity of the wing surface area ratio between the front and rear wing on the total fuel consumption was investigated for the single aisle, medium range mission. A design featuring an area ratio of 1.25 required 2% less fuel, compared to a design with an even area distribution between the wings. While the exact savings and optimal area ratio are case-specific, the results indicate that the required fuel mass is sensitive to the area distribution between the front and rear wing. This parameter should thus be taken into account in future design optimization studies of PrandtlPlane configurations.

To conclude, the Initiator is now capable of determining the wing weight and its distribution for closed-wing configurations accurately. For PrandtlPlanes, the sweep angles of the fin and wings, the wingspan and the position of the center of gravity are the most sensitive parameters that determine the total wing weight and its distribution. They should thus be selected with great care in design and optimization studies, along with the area ratio between the front and rear wing. Subsequent design studies should include the closed-wing weight estimator, since the original methodology misestimated the total wing weight and its distribution, which lead to significant under- or over-predictions of the required fuel weight for a given mission.

8

RECOMMENDATIONS

The recommendations for further improvements on the methodology and analyses presented in this report can be divided in two parts. First, possible improvements in the closed-wing weight estimation are discussed in Section 8.1. Recommendations for the conceptual PrandtlPlane design are compiled in Section 8.2.

8.1. IMPROVEMENTS TO THE CLOSED-WING WEIGHT ESTIMATION

A few improvements can be made to improve the accuracy of the closed-wing weight estimation. First, column buckling considerations are not taken into account in the closed-wing weight estimation methodology. Research by Bindolino et al. indicates that column buckling could increase the primary wing weight of a PrandtlPlane by as much as 7% compared to a structure only sized for static loads.[18] An investigation into this behaviour could prove beneficial to the accuracy of the tool. An initial analysis in Section 5.3 showed that the maximum buckling load in a cross-section depends heavily on the rib spacing and shape of the supports in the corners of the cross-section. These parameters would thus have to be provided as inputs to the tool. Each boom in the cross-section would then be sized for its critical load, either the static or the buckling load. A problem that might be encountered by sizing the cross-sections for both static and buckling loads is the state-switching between the critical load cases. This effect could degrade the convergence behaviour of the stiffness iteration loop. An additional consideration to be taken into account is the fact that a linear analysis of the buckling behaviour in the PrandtlPlane wing is generally not capable of predicting the buckling behaviour accurately. Demasi et al. indicate that the post-critical behaviour of the configuration is highly non-linear and that linear models greatly under- or overestimate the buckling load in the structure depending on the configuration.[33]

Secondly, aeroelastic effects are not considered in the analysis. The displacements of the structural model would then be used to update the aerodynamic shape of the wings in the next iteration. Bindolino et al. found an increase of 2.4% in the total wing weight by including a single static aeroelastic iteration.[18] While this effect may seem small, they also determined that including an aeroelastic loop shifts the weight distribution between the three surfaces considerably.[18] The results in Chapter 6 indicated both the wing weight and aircraft performance to be sensitive to the center of gravity position. A small shift in wing weight distribution might thus have a significant effect on the overall performance of the configuration. Including one aeroelastic iteration would double the time required for a fully converged closed-wing weight estimation.

Thirdly, the effect of engines on the load distribution was initially neglected because the original PrandtlPlane configuration by Frediani only features two fuselage-mounted engines.[9] However, for the twin-aisle and high payload configurations in Section 6.3 two wing-mounted engines were necessary. The loads induced by the weight and thrust of these engines on the structural model should be included into the estimation of the primary wing weight. Additional inputs to the closed-wing weight estimation would then be required to define the spanwise and chordwise positions of the engines, as well as their weight and thrust. A resulting external force and moment can then be applied to the structural model.

The generation of the aerodynamic loads is currently performed with a vortex lattice methodology. Improvements in the accuracy of the wing weight estimator can be realized by improving the load generation module. Elham et al. coupled a vortex lattice methodology, with two 2D aerodynamic solvers to determine the pitching moment due to the airfoil shape.[23] The local lift coefficients at each spanwise section are cal-

culated using the vortex lattice methodology and used as inputs to the 2D aerodynamic analysis. Such a procedure could be implemented into the current methodology with relative ease.

The secondary weight estimation of the closed-wing configuration could be improved as well. At the moment a regression of conventional data is used if not enough information is available to use Torenbeeks method. Deriving an empirical relation for PrandtlPlane configurations based on actual design data is impossible due to the lack of available data. However, a regression analysis might be performed with the results from Torenbeeks weight estimation for several PrandtlPlane designs. This relationship might than be employed during the weight estimation if information about high lift devices, ribs spacing and control surfaces is not yet known.

As described in Section 2.1, two methodologies exist to define the constraints induced by the fin on the rear wing. For all analyses presented in this report, the fin was modelled as a support under an angle to the rear wing. The corresponding assumption is that the fin is infinitely stiff in tension and bending. In a more detailed approach, the fin can be modelled as a structural element with a certain stiffness. The closed-wing weight estimation is capable of handling such an analysis, but will size the fins for a pull-up manoeuvre, which is probably not the critical condition for these surfaces. Performing an analysis for a lateral manoeuvre to size the fins and implementing their stiffness distribution into the closed-wing weight estimator would be an option to improve the overall weight estimation accuracy.

The main goal of this research is to determine whether the PrandtlPlane configuration can replace conventional aircraft in the future. In the current closed-wing weight estimation however, only metallic materials are considered. For future designs, the primary wing structure might be built up from composite materials. The EMWET methodology by Elham et al. makes use of the Angle Minus Longitudinal Plots method to determine the cutoff strains of composite materials.[23] A similar approach might be employed in the closed-wing weight estimator. This would require additional inputs to the tool, since the layup of the material should be defined.

A final improvement can be made by considering more loading conditions for the sizing of the primary wing structure. Currently, a single limit load factor, design weight and center of gravity position are supplied as inputs for the analysis. The wing weight and distribution were found to be sensitive to the position of the center of gravity in Section 6.1.6. Furthermore, no previous research has been performed which determines a 2.5g pull-up manoeuvre to be critical for the structural sizing of closed-wings. Therefore, having the ability to analyse a range of loading conditions, including gusts and shifting center of gravities, could help in determining the critical load case for closed-wing configurations. A study into the effects of these load cases on the wing weight could help define the critical load case to be used in more advanced, finite element based, weight estimation methodologies.

8.2. IMPROVEMENTS TO THE CONCEPTUAL DESIGN METHODOLOGY

The major limitation to the conceptual design of the PrandtlPlane configuration in the Initiator was the lack of an accurate closed-wing weight estimation. This problem was addressed by implementing the methodology described in this report. However, further improvements to the conceptual design methodology can still be made.

First of all, the conceptual sizing of the PrandtlPlane configuration is not automated or optimized yet. The design is based on input parameters for the front wing, rear wing and fins. Zohlandt used the Initiator for an optimization study, in which the optimal set of design inputs was determined for a given mission.[11] However, the results in Section 6.3 indicate that the updated weight estimation has a major influence on the performance of the resulting design. Furthermore, the effect of shifts in wing area between the front and rear wing can now be determined accurately. Therefore, the optimization studies should be repeated to determine if her conclusions are still accurate. The optimized PrandtlPlanes can then be compared to their conventional counterparts, which are optimized in the Initiator as well, for the same mission requirements. The results will give an indication of the feasibility of the PrandtlPlane as the future of aviation.

Instead of sizing the PrandtlPlane configuration based on supplied inputs, some parameters should be updated automatically. The controllability and stability analysis is currently performed at the end of a converged design and the results are not used to redesign the aircraft. As shown in Section 4.2.4, the controllability limit mainly depends on the horizontal spacing between the front and rear wing. By checking for stability and controllability earlier in the design, the positioning of the front wing can be adapted to reach a feasible solution. Using the same principle, the area distribution between the wings and the control surface lay-out can be selected to influence the trim drag of the configuration.

BIBLIOGRAPHY

[1] Kaloterakis N. The jets of the future, 2012. http://www.kollected.com/.

[2] Andrews S. A., Perez R. E., and Wowk D. Wing weight model for conceptual desin of nonplanar configurations. *Aerospace Science and Technology*, 43:51–62, 2015.

[3] Przemieniecki J. S. *Theory of Matrix Structural Analysis*. McGraw-Hill, 1968.

[4] Schiktanz D. and Scholz D. The conflict of aerodynamic efficiency and static longitudinal stability of box wing aircraft. In *3rd CEAS Air&Space Conference*, pages 910–921, Venice, October 2011. CEAS.

[5] Sgouridis S, Bonnefoy P. A, and Hansman R. J. Air transportation in a carbon constrained world: Long-term dynamics of policies and strategies for mitigating the carbon footprint of commercial aviation. *Transportation Research Part A: Policy and Practice*, 45, 2011.

[6] International Air Transportation Association . Vision 2050. http://www.iata.org/, February 2011. Accessed: 18–8-2016.

[7] European Commission . Flightpath 2050: Europe's vision for aviation. http://bookshop.europa.eu, 2011. Accessed: 18–8-2016.

[8] International Air Transportation Association . A global approach to reducing aviation emissions. http://www.iata.org/, August 2009. Accessed: 18–8-2016.

[9] Frediani A, Cipolla V, and Rizzo E. The prandtlplane configuration: Overview on possible applications to civil aviation. In Frediani A. and Buttazzo G., editors, *Variational Analysis and Aerospace Engineering: Mathematical Challenges for Aerospace Design*, volume 66, pages 179–210. Springer, 2012.

[10] Elmendorp R., Vos R., and La Rocca G. A conceptual design and analysis method for conventional and unconventional airplanes. In *29th Congress of the International Council of the Aeronautical Sciences*, St. Petersburg, Russia, September 2014.

[11] Zohlandt C.N. Conceptual design of high subsonic prandtl planes: Analysis and performance comparison with conventional configurations in the high subsonic transport category. Master's thesis, Delft University of Technology, February 2016.

[12] Voskuijl M., de Klerk J., and van Ginneken D. Flight mechanics modeling of the prandtlplane for conceptual and preliminary design. In Frediani A., editor, *Variational Analysis and Aerospace Engineering: Mathematical Challenges for Aerospace Design*, volume 66, pages 435–462. Springer, 2012.

[13] Schiktanz D. and Scholz D. Box wing fundamentals - an aircraft design perspective. In *Deutscher Luft - und Raumfahrtkongress 2011*, pages 601–615, Bremen, September 2011. DLR.

[14] Prandtl L. Induced drag of multiplanes. Technical report, National Advisory Comittee for Aeronautics, Technical note no. 182, March 1924.

[15] Demasi L., Monegato G., Emanuele R., Cavallaro R., and Dipace Antonio. Minimum induced drag theorems for joined wings, closed-systems, and generic biwings: Results. In *56th AIAA/ASCE/AHS/ASC Structures, Structural Dynamics, and Materials Conference*, Kissimmee, Florida, USA, January 2015. AIAA SciTech.

[16] Munk M. General biplane theory. Technical report, National Advisory Comittee for Aeronautics, Report No. 151, 1924.

[17] Kalinowski M. J. Structural optimization of box wing aircraft. *Archive of Mechanical Engineering*, 62(1): 45–60, 2015.

[18] Bindolino G., Ghiringhelli G., Ricci S., and Terraneo M. Multilevel structural optimization for preliminary wing-box weight estimation. *Journal of Aircraft*, 47(2), 2010.

[19] Jemitola P. O. *Conceptual Design and Optimization for Box Wing Aircraft*. PhD thesis, School of Aerospace Engineering, Cranfield University, 2012.

[20] Oliviero F. and Frediani A. Conceptual design of a very large prandtlplane freighter. In Frediani A., editor, *Variational Analysis and Aerospace Engineering: Mathematical Challenges for Aerospace Design*, volume 66, pages 305–321. Springer, 2012.

[21] van Ginneken D. A. J., Voskuijl M., Tooren M. J. L., and Frediani A. Automated control surface design and sizing for the prandtl plane. In *51st AIAA/ASME/ASCE/AHS/ASC Structures, Structural Dynamics, and Materials Conference*, Orlando, Florida, April 2010. American Institute of Aeronautics and Astronautics.

[22] Salam I. R and Bil C. Multi-disciplinary analysis and optimisation methodology for conecptual design of box-wing aircraft. *The Aeronautical Journal*, 120(1230):1315–1333, August 2016.

[23] Elham A., La Rocca G., and van Tooren M. J. L. Development and implementation of an advanced, design-sensitive method for wing weight estimation. *Aerospace Science and Technology*, 29:100–113, 2013.

[24] Dorbath F. *A Flexible Wing Modeling and Psyical Mass Estimation System For Early Aircraft Design Stages*. phdthesis, TUHH, 2014.

[25] Dal Canto D., Frediani A., Ghiringhelli G. L., and Terraneo M. The lifting system of a prandtlplane, part 1: Design and analysis of a light alloy structural solution. In Frediani A., editor, *Variational Analysis and Aerospace Engineering: Mathematical Challenges for Aerospace Design*, volume 66, pages 211–234. Springer, 2012.

[26] Gallman J. W. and Kroo I. M. Structural optimization for joined-wing synthesis. *Journal of Aircraft*, 33 (1):214–223, 1996.

[27] Kroo I. Drag due to lift: Concepts for prediction and reduction. *Annual Review of Fluid Mechanics*, 33: 587–617, 2001.

[28] Megson T.H.G. *Aircraft Structures: for engineering students*. Elsevier, 5 edition, 2013.

[29] Torenbeek E. Development and application of a comprehensive, design-sensitive weight prediction method for wing structures of transport category aircraft. techreport, Delft University of Technology, September 1992.

[30] Raymer D.P. *Aircraft Design: A Conceptual Approach*. American Institute of Aeronautics and Astronautics, second edition edition, 1992.

[31] Drela M. and Youngren H. Avl 3.36 user primer. http://web.mit.edu/drela/Public/web/avl/avl_doc.txt, February 2017.

[32] Roskam J. *Airplane Design*. Roskam Aviation and Engineering Corporation, 1990.

[33] Demasi L. and Cavallaro A.M., R.and Razón. Postcritical analysis of prandtlplane joined-wing configurations. *AIAA Journal*, 51(1), January 2013.

A

Overview of Data Flow in Closed-Wing Weight Estimator

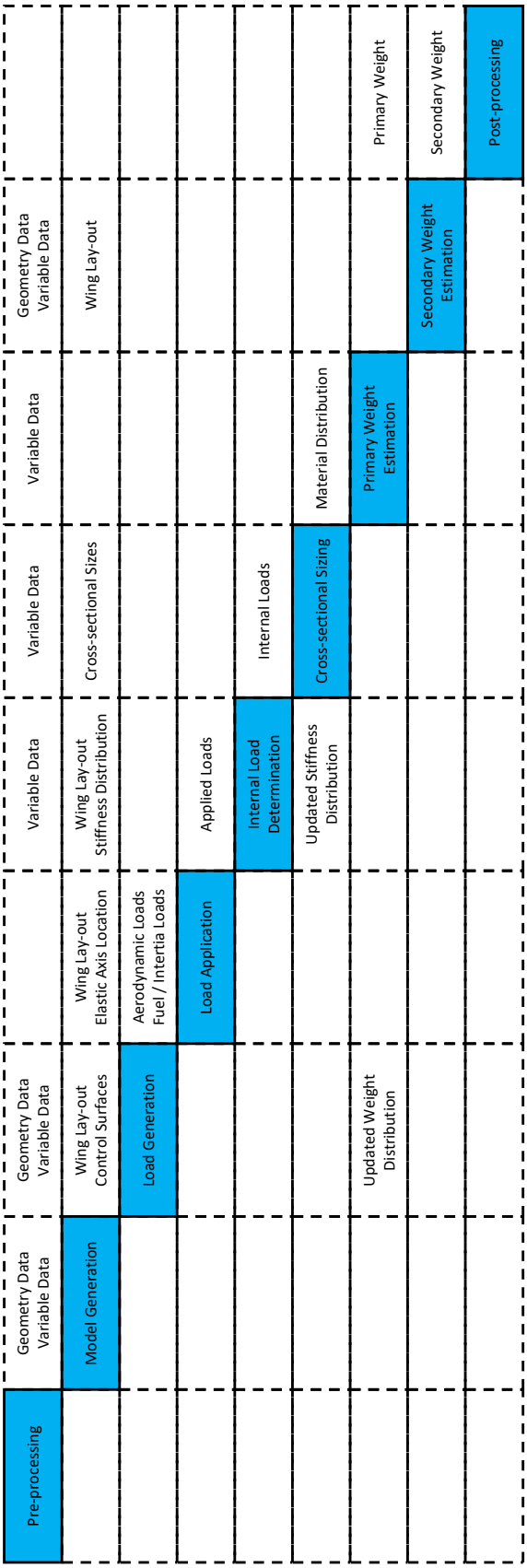

Figure A.1: Overview of the weight estimation variable flow between modules.

B

Reference Case Closed-Wing Weight Estimation

Listing B.1: Geometry input file for the reference case.

```
SURFACE
FrontWing
SECTIONS
0 0 0 4 0 0.25 0.75 NxYHv62IMK_boeing-c 0 0 1
8 15 0 2 0 0.25 0.75 NxYHv62IMK_boeing-c 0 0 1
CONSTRAINTS
0 0 0 clamped 0 0 0
8 15 0 rigid 0 0 0
CONTROL
Elevator 0 0.25 -0.1 0.75
FUEL
0 0.95 73507.3

SURFACE
MainWingConnector
SECTIONS
8 15 0 2 0 0.25 0.75 NxYHv62IMK_boeing-c 0 -1 0
9 15 3 2 0 0.25 0.75 NxYHv62IMK_boeing-c_mirror 0 -1 0
CONSTRAINTS
8 15 0 rigid 0 0 0
9 15 3 rigid 0 0 0

SURFACE
RearWing
SECTIONS
9 15 3 2 0 0.25 0.75 NxYHv62IMK_boeing-c 0 0 1
17 0 3 4 0 0.25 0.75 NxYHv62IMK_boeing-c 0 0 1
CONSTRAINTS
9 15 3 rigid 0 0 0
16 1.875 3 support 0.6 0.2 1
17 0 3 symmetry 0 0 0
CONTROL
Elevator 0.75 1 1 0.75
FUEL
0.05 1 73495.1
```

Listing B.2: Variable input file for the reference case.

```
0.78  0.348309  230.154
150  2.5  30
9  0  0
64  quad
614985  126613
7.25e+10  2.69e+10  5.05e+08  3.31e+08  2800  1.5
614985  2.5  1
0.5
0
```

C

NASTRAN VERIFICATION

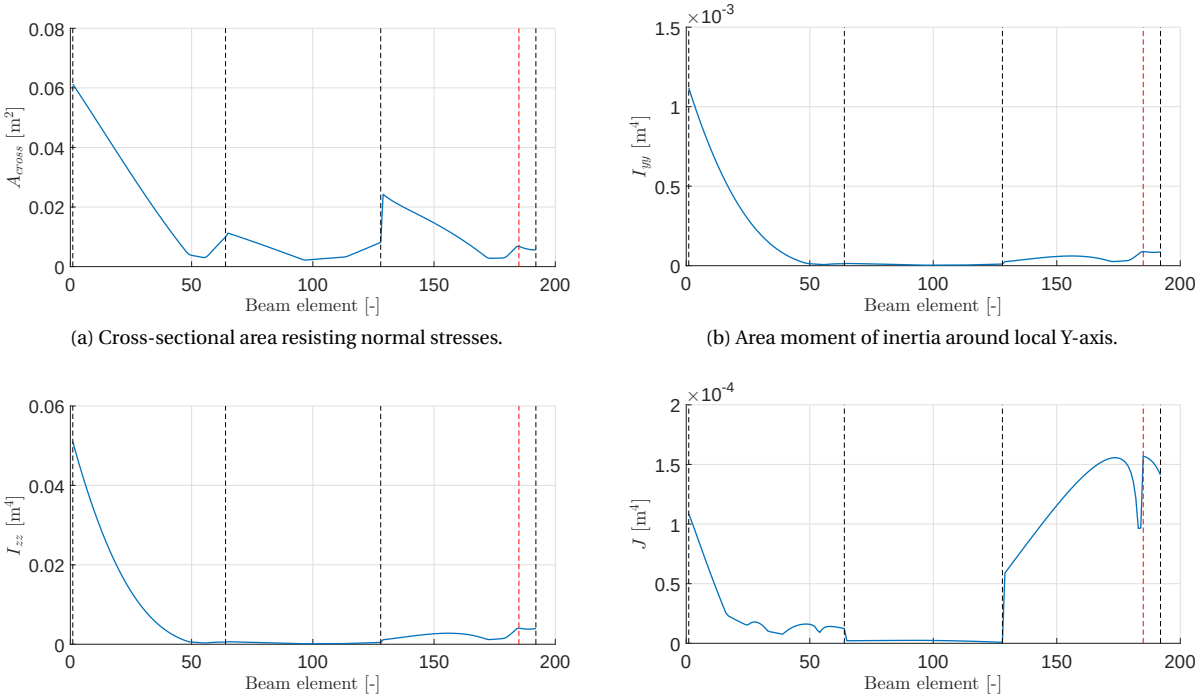

(a) Cross-sectional area resisting normal stresses.

(b) Area moment of inertia around local Y-axis.

(c) Area moment of inertia around local z-axis.

(d) Polar moment of inertia.

Figure C.1: Distribution of stiffness parameters throughout the system.

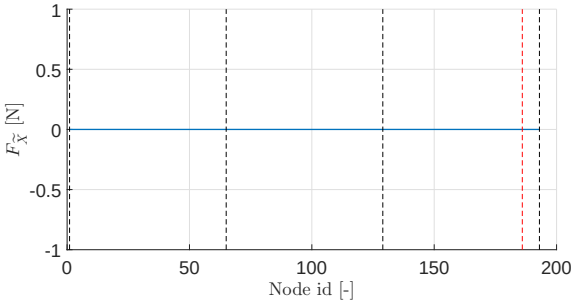

(a) External forces in X.

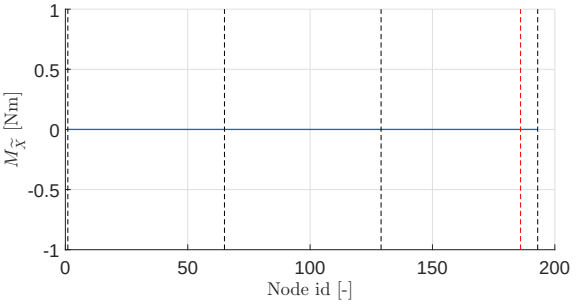

(b) External moments around X.

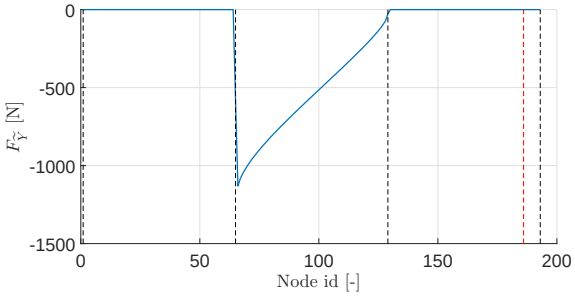

(c) External forces in Y.

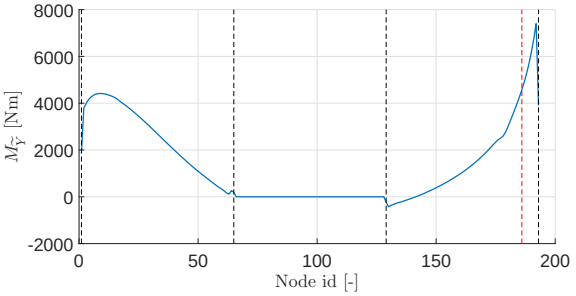

(d) External moments around Y.

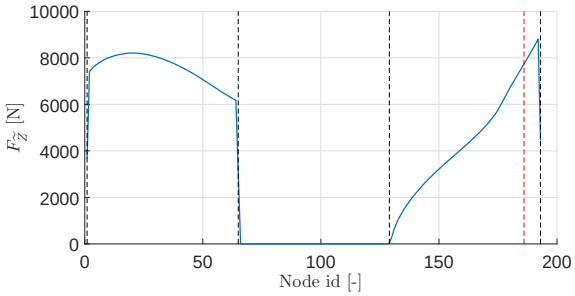

(e) External forces in Z.

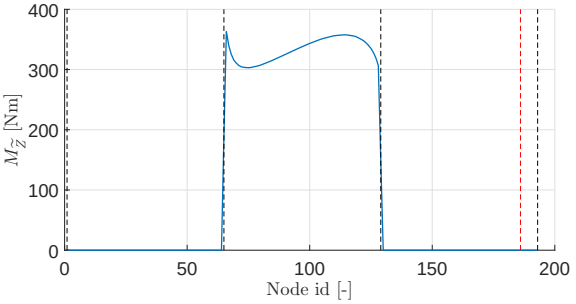

(f) External moments around Z.

Figure C.2: Internal load comparison between tool and Nastran.

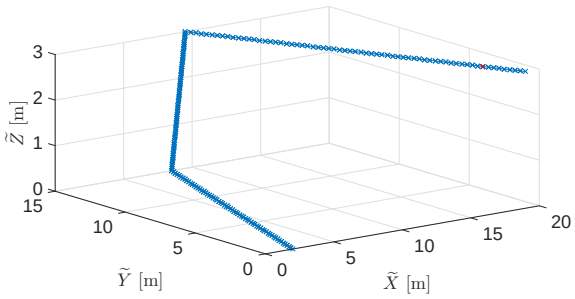

Figure C.3: Structural grid definition of the Nastran comparison model.

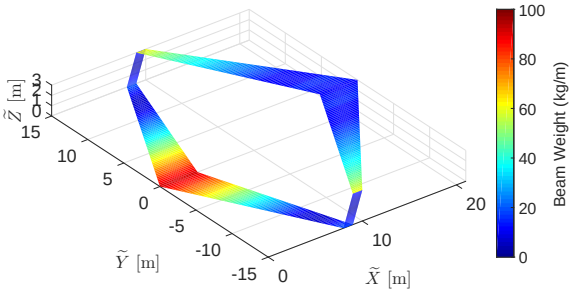

Figure C.4: Wing weight distribution and geometric lay-out of the Nastran comparison design.

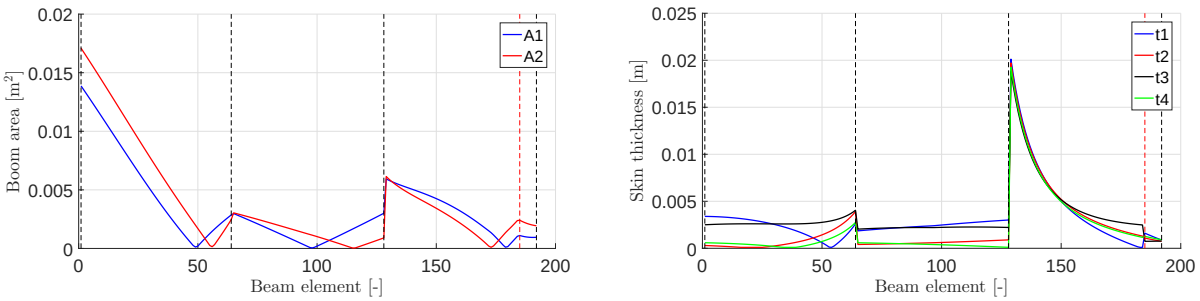

(a) Boom area distribution.

(b) Skin thickness distribution.

Figure C.5: Local sizing results of the verification case.